

**INTRACELLULAR DRUG DELIVERY USING LASER ACTIVATED
CARBON NANOPARTICLES**

A Thesis
Presented to
The Academic Faculty

by

Aritra Sengupta

In Partial Fulfillment
of the Requirements for the Degree
Doctor of Philosophy in the
School of Chemical and Biomolecular Engineering

Georgia Institute of Technology
August 2014

Copyright © 2014 by Aritra Sengupta

INTRACELLULAR DRUG DELIVERY USING LASER ACTIVATED CARBON NANOPARTICLES

Approved by:

Dr. Mark R. Prausnitz, Advisor
School of Chemical and Biomolecular
Engineering
Georgia Institute of Technology

Dr. Naresh N. Thadhani
School of Materials Science and
Engineering
Georgia Institute of Technology

Dr. Julie A. Champion
School of Chemical and Biomolecular
Engineering
Georgia Institute of Technology

Dr. Mark P. Styczynski
School of Chemical and Biomolecular
Engineering
Georgia Institute of Technology

Dr. Athanassios Sambanis
School of Chemical and Biomolecular
Engineering
Georgia Institute of Technology

Date Approved: 8 May 2014

Dedicated to my parents.

ACKNOWLEDGEMENTS

First of all, I wish to thank my parents, especially my mother, for leading me to the path of education. I would like to thank all my school teachers for believing in me and encouraging me to do well. I would like to thank my undergraduate mentors Dr. Sunando DasGupta, Dr. Sirshendu De and Dr. Swapan Ghosh for giving me the first opportunity to do research in their labs. I would like to thank Dr. Brian Pogue for giving me an opportunity to come to the US and work on breast cancer imaging which fueled my interest in bio based research.

I would like to thank Dr. Mark Prausnitz, first of all for accepting me in his group and secondly for giving me a wonderful project to work on. I thank him for giving me the freedom and liberty to do all sorts of experiments that were reasonably feasible. I would also like to thank Donna Bondy for her constant encouragement and support throughout my Ph.D. Her management of all the lab supplies, funding and other logistical issues really inspired me to manage my own research well. I would also like to thank Dr. Ying Liu for introducing me to cell culture, Dr. Samantha Andrews for constantly encouraging me during the tough 2nd and 3rd years of Ph.D., Dr. Yoo Chun Kim for being on the same boat as I was and sharing the frustration with me when things did not work. I thank all the past and present drug delivery lab members for their help and support throughout my Ph.D.

Finally, I would like to thank my friends without whom I would not have made anywhere close to where I am today, specifically I would like to thank Dr. Sayan Chakraborty for showing me the meaning of hardwork and dedication in life.

TABLE OF CONTENTS

DEDICATION	iii
ACKNOWLEDGEMENTS	iv
LIST OF FIGURES	ix
SUMMARY	xvi
I INTRODUCTION	1
II BACKGROUND	4
2.1 Current Intracellular Drug Delivery Techniques	5
2.1.1 Chemical Methods	5
2.1.2 Biological Methods	6
2.1.3 Physical Methods	7
2.1.4 Lasers in medicine	10
2.1.5 Drug Delivery using laser	12
2.2 Carbon Nanoparticles in Medicine	13
2.3 Laser Particle Interaction	14
2.3.1 Laser Carbon Interaction	14
2.4 RNA Interference and siRNA	15
III EFFICIENT INTRACELLULAR DELIVERY OF MOLECULES WITH HIGH CELL VIABILITY USING NANOSECOND-PULSED LASER- ACTIVATED CARBON NANOPARTICLES	18
3.1 Introduction	19
3.2 Methods	20
3.2.1 Laser Apparatus	20
3.2.2 Cell Preparation	21
3.2.3 Nanoparticle Preparation	21
3.2.4 Sample Exposure	22
3.2.5 Cytotoxicity of CB Nanoparticles	23
3.2.6 Analysis and Quantification	23
3.2.7 Statistical Analysis	24

3.3	Results	24
3.3.1	Intracellular uptake due to laser-activation of CB nanoparticles	24
3.3.2	Effects of laser pulse fluence, number of pulses, beam spot size and pulse repetition rate on intracellular uptake and cell viability	25
3.3.3	Effects of interaction between sequential pulsing protocols on uptake and viability	30
3.3.4	Effects of CB nanoparticle type and concentration on uptake and viability	33
3.3.5	Toxicity of CB nanoparticles	34
3.3.6	Effects of cell type and molecular weight of uptake marker on uptake and viability	37
3.3.7	Trade-off between maximizing uptake and maximizing viability	37
3.4	Discussion	40
3.5	Conclusion	44
IV	POLOXAMER SURFACTANT PRESERVES CELL VIABILITY DURING PHOTOACOUSTIC DELIVERY OF MOLECULES INTO CELLS	45
4.1	Introduction	45
4.2	Materials and Methods	47
4.2.1	Cell Preparation	47
4.2.2	Nanoparticle Preparation	48
4.2.3	Additive Preparation	48
4.2.4	Laser Apparatus	49
4.2.5	Sample Exposure	49
4.2.6	Analysis and Quantification	50
4.2.7	Statistical Analysis	51
4.3	Results	51
4.3.1	Effect of Laser Exposure Conditions on Photoacoustic Delivery of Molecules into Cells and Cell Viability	51
4.3.2	Effect of Poloxamer Surfactants	55
4.3.3	Effect of Cell-Repair Mechanism Enhancers	57
4.3.4	Effect of Glycine Betaine	60
4.4	Discussion	62
4.5	Conclusion	64

V	MECHANISM OF ENERGY TRANSFER FROM LASER TO NANOPARTICLE TO FLUID MEDIUM TO CELL	65
5.1	Introduction	65
5.2	Materials and Methods	67
5.2.1	Laser Apparatus	67
5.2.2	Nanoparticle Preparation	68
5.2.3	Cell Preparation, Exposure and Imaging	69
5.2.4	Transmittance Measurements	70
5.2.5	Acoustic Measurements	70
5.2.6	Temperature Measurement	71
5.3	Results and Discussion	72
5.3.1	Intracellular Drug Delivery	72
5.3.2	Light Absorption and Heating	74
5.3.3	Heating Timescale, Particle Temperature, Bubble Formation and Reaction	78
5.3.4	Pressure Generation	80
5.3.5	Impact on Cells	86
5.4	Conclusion	88
VI	siRNA DELIVERY USING PHOTOACOUSTICS	90
6.1	Introduction	90
6.2	Delivery System Design	92
6.3	Intracellular Drug Delivery with Laser Activated CB	95
6.4	siRNA Delivery and Knockdown	98
6.5	Conclusion	100
VII	DISCUSSION AND CONCLUSION	102
7.1	Contribution	110
VIII	RECOMMENDATIONS	111
8.1	Nanoparticles	111
8.2	System Characterization	113
8.3	Understanding Hypothesis	114
8.4	siRNA Delivery	116

8.5	Characterization in-vivo	116
APPENDIX A	— IN-VIVO STUDIES	118
APPENDIX B	— SUPPLEMENTARY INFORMATION FOR PHYSICAL MECHANISMS	128
APPENDIX C	— siRNA SUPPLEMENTARY INFORMATION	137
REFERENCES	147

LIST OF FIGURES

3.1	Fluorescence imaging of intra-cellular uptake. Cells inspected visually using a confocal microscope show that there is little uptake of calcein (green) when cells were exposed to just carbon black (CB) nanoparticles but no laser (a), very little uptake when cells were exposed to laser but not CB nanoparticles (b) and extensive uptake when cells were exposed to laser with CB nanoparticles at 44 mJ/cm ² fluence, 1 min exposure time, 10 Hz pulsing frequency and 21.4 mm beam diameter (c). Closer inspection of these cells at higher magnification, reveals that calcein is present throughout the interior of the cells and not just localized, for example, to endosomes (d). In all samples, very few cells were stained with propidium iodide (red), which is a marker of necrotic and late apoptotic deaths. Scale bars are 20 μ m.	26
3.2	Effect of laser fluence on intra-cellular uptake and viability of DU145 cells. Cells were exposed to laser for 1 min at various laser fluence levels. Asterisk (*) shows data where viability is lower than sham and hash symbol (#) shows data where uptake is lower than viability (p <0.05). The figure demonstrates saturation of both uptake and viability beyond 44 mJ/cm ² exposure. All laser exposures were at 10 Hz pulsing frequency and 21.4 mm beam diameter. Data show average \pm standard deviation (SD) (n = 3 replicates).	27
3.3	Effect of exposure time and total energy on intracellular uptake and viability of DU145 cells. (a) When fluence was set at 18.75 mJ/cm ² , there was no change of viability but uptake increased with exposure time until it was the same as viability at 7 min. (b) When fluence was set at 25 mJ/cm ² , viability was less than the sham and uptake was always significantly lower than viability (p <0.05). (c) When total energy is plotted against uptake, at ≥ 100 J, uptake remained approximately constant at $\sim 75\%$ at higher energy levels. All laser exposures were at 10 Hz pulsing frequency and 21.4 mm beam diameter. Asterisk (*) shows data where viability is lower than sham and hash symbol (#) shows data where uptake is lower than viability. Data show average \pm SD (n = 3).	29
3.4	Effect of beam diameter and pulsing frequency on intracellular uptake and viability of DU145 cells. (a) Reducing the beam diameter from 21.4 mm (full cuvette) to 9 mm (16% of the cuvette surface area) resulted in lesser bioeffects, with higher viability and lower uptake (44 mJ/cm ² fluence, 1 min exposure time, 10 Hz pulsing frequency). (b) Increasing pulsing frequency from 0.1 Hz to 10 Hz while keeping number of pulses at 100 had no statistically significant effect on viability, while uptake was slightly higher at 0.1 Hz compared to 1 Hz and 10 Hz (44 mJ/cm ² fluence, 21.4 mm beam diameter). Asterisk (*) and hash symbol (#) show statistically significant differences in uptake and viability, respectively (p <0.05). Data show average \pm SD (n = 3).	31

3.5	Effect of pretreatment and sequential laser exposures on intracellular uptake and viability of DU145 cells. (a) Compared to sham treatment (A), there was no significant effect of weak laser exposure of cells in the presence of CB nanoparticles (B). Very strong laser exposure of CB nanoparticles (without cells) as a pretreatment followed by addition of cells and weak laser exposure (C) was not significantly different from conditions (B) and (A) in terms of uptake and viability. (b) The sequential combination of a strong laser exposure and weak laser exposure (E) was statistically no different from the strong laser exposure alone (D) and much greater than the weak laser exposure alone (B) in terms of uptake and viability. (C) The sequential combination of two strong laser exposures with different laser parameters (G) had lower viability but uptake was not statistically different from either of the individual laser exposures alone (D, F). All laser exposures were at 10 Hz pulsing frequency and 21.4 mm beam diameter. Asterisk (*) and hash symbol (#) show statistically significant differences in uptake and viability, respectively ($p < 0.05$). Data show average \pm SD ($n = 3$).	32
3.6	Effect of increasing India ink and CB nanoparticle concentration on intracellular uptake and viability of DU145 cells. In each paired comparison, the concentration of India ink and CB nanoparticles were adjusted so that the laser absorbance was the same. Uptake and viability generally decreased with increasing nanoparticle concentration, and India ink had stronger effects on uptake and viability than CB nanoparticles at the higher concentrations. All laser exposures were at 44 mJ/cm ² fluence, 1 min exposure time, 10 Hz pulsing frequency and 21.4 mm beam diameter. Asterisk (*) and hash symbol (#) show statistically significant differences in uptake and viability, respectively ($p < 0.05$). Data show average \pm SD ($n = 3$).	35
3.7	Toxicity of CB nanoparticles on DU 145 cells measured by MTT cytotoxicity assay. Cells were exposed to CB nanoparticles for 24 h and 72 h, which yielded ED50 values of 350 mg/l and 360 mg/l, respectively. These values are ~14 times higher than the concentration (25 mg/l) used in most experiments in this study. Data show average \pm SD ($n = 3$).	36
3.8	Comparison of intracellular uptake and viability of two cell lines (DU145 and H9c2) after the same laser exposures. Cell viability was the same, whereas uptake after the 1 min exposure was significantly different between the two cell lines. All laser exposures were at 25 mJ/cm ² fluence, 10 Hz pulsing frequency and 21.4 mm beam diameter. Asterisk (*) shows statistically significant difference in uptake ($p < 0.05$). Data show average \pm SD ($n = 3$).	38
3.9	Effect of molecular weight on intracellular uptake and viability after the same laser exposures. There is no statistical difference in viability across all samples, whereas the uptake decreased as the molecular weight was increased for calcein (Cal), 10 kDa dextran (D10), 70 kDa dextran (D70) and 500 kDa dextran (D500). All laser exposures were at 44 mJ/cm ² , 10 Hz and 21.4 mm beam diameter. Asterisk (*) shows statistically significant difference in uptake ($p < 0.05$). Data shows average \pm SD ($n = 3$).	39

3.10	Comparison between intracellular uptake and viability. This graph shows all data generated in this study (i.e., from Figures 2 - 7). All data points are at or below the uptake = viability line since there cannot be more cells with uptake than cells that are viable.	41
4.1	Effect of photoacoustic delivery using nanosecond-pulsed laser and CB nanoparticles on uptake and viability of DU145 prostate cancer cells. (A) Percentage of cells remaining viable and exhibiting intracellular uptake of calcein is shown as a function of photoacoustic exposure conditions, including laser fluence (mJ/cm^2) and exposure time (min). Representative flow cytometry scatter plots are shown for cells at the same six conditions shown in part (A): (B) untreated cells (cells only), (C) cells exposed to CB nanoparticles but no laser (sham), (D) cells exposed to laser ($44 \text{ mJ}/\text{cm}^2$, 7 min) but no CB nanoparticles, and cells exposed to CB nanoparticles and laser at (E) $25 \text{ mJ}/\text{cm}^2$, 1 min, (F) $25 \text{ mJ}/\text{cm}^2$, 7 min and (G) $44 \text{ mJ}/\text{cm}^2$, 3 min. The asterisk symbol (*) represents statistical difference of viability between two samples ($p < 0.05$) and hash symbol (#) signifies that uptake and viability for a given sample are significantly different ($p < 0.05$). Data show average \pm standard deviation (SD) with three replicates each ($n = 3$).	52
4.2	Cell sorting between two populations of cells seen after exposure to strong photoacoustic conditions. (A) Representative flow cytometry scatter plot of cells exposed to CB nanoparticles and laser at $44 \text{ mJ}/\text{cm}^2$, 3 min. Fluorescence microscopy image shown of representative cells from (B) the population with higher forward scatter (P1), exhibiting green fluorescence from calcein uptake and (C) the population with lower forward scatter (P2) exhibiting red fluorescence from PI staining. Scale bars are $20 \mu\text{m}$	54
4.3	Effect of poloxamer surfactants on the viability and uptake of DU145 cells when exposed to laser in the presence of CB nanoparticles. (A) Effect of F-68 poloxamer at different concentrations (2%, 5%, 10% (v/v)) on cell viability and uptake with sham or actual exposure to laser ($25 \text{ mJ}/\text{cm}^2$, 7 min). (B) Effect of F-68 poloxamer at 10% (w/v) concentration on cell viability and uptake with sham or actual exposure to laser ($44 \text{ mJ}/\text{cm}^2$, 3 min). (C) Effect of F-127 poloxamer at different concentrations (5%, 10% (v/v)) on cell viability and uptake with sham or actual exposure to laser ($44 \text{ mJ}/\text{cm}^2$, 3 min). Representative flow cytometry scatter plots are shown for cells exposed to laser ($44 \text{ mJ}/\text{cm}^2$, 3 min) with (D) no poloxamer, (E) 10% (v/v) F-68 poloxamer (F) 5% (v/v) F-127 poloxamer, (G) 10% (v/v) F-127 poloxamer. The asterisk symbol (*) represents statistical difference of viability between two samples ($p < 0.05$) and hash symbol (#) signifies that uptake and viability for a given sample are significantly different ($p < 0.05$). Data show average \pm SD ($n = 3$).	56

4.4	Effect of treatment with various cell-repair mechanism enhancers on the viability and uptake of DU145 cells when exposed to laser in the presence of CB nanoparticles. (A) Effect of BAPTA-AM, an intracellular Ca^{2+} chelator, added before laser exposure. (B) Effect of ATP, a source of cellular energy, added before laser exposure. (C) Effect of ATP and CaCl_2 , which triggers plasma membrane repair mechanisms, added before laser exposure and BAPTA-AM added after laser exposure. (D) Effect of FBS, a source of nutrients, growth factors and protective compounds found, added before laser exposure. The asterisk symbol (*) represents statistical difference of viability between two samples ($p < 0.05$) and hash symbol (#) signifies that uptake and viability for a given sample are significantly different ($p < 0.05$). Data show average \pm SD ($n = 3$).	59
4.5	Effect of treatment with glycine betaine (GB) on the viability and uptake of DU145 cells when exposed to laser in the presence of CB nanoparticles. The asterisk symbol (*) represents statistical difference of viability between two samples ($p < 0.05$) and hash symbol (#) signifies that uptake and viability for a given sample are significantly different ($p < 0.05$). Data show average \pm SD ($n = 3$).	61
5.1	A schematics of laser carbon interaction and drug delivery. The nanosecond laser heats the carbon black (CB) nanoparticles and heats them, producing a pressure wave along with a vapor bubble. This leads to intracellular drug delivery of calcein.	67
5.2	Fluorescence imaging of intracellular uptake of calcein in DU145 cells. Both laser and carbon black are necessary for significant uptake of calcein under the conditions tested and calcein should be added before the exposure for delivery to be efficient (a). With increasing concentration of CB the uptake initially increases but after a certain concentration of CB, the uptake falls (b). Calcein uptake initially goes up and then it saturates as the fluence of the laser is increased (c). Scale bars are $100 \mu\text{m}$	73
5.3	Absorption of IR light by CB nanoparticles using two different techniques. Absorption of light increases linearly when CB concentration is increased at different wavelengths of light when measured using a spectrophotometer (a). Absorption of IR nanosecond laser using power meter shows increase in absorption of laser when the concentration of CB is increased (b). Data show average \pm standard deviation (SD) ($n = 3$ replicates).	75
5.4	Bulk temperature rise measured using an IR camera of a CB suspension at two different concentrations (12.5 and 25 mg/l) and two different laser fluences (25 and 44 mJ/cm^2). The temperature rise was lower when CB suspensions were replaced with pure DI water. Higher temperature rise resulted when either the fluence or the CB concentration was increased. The solid lines were the modeled temperature rise.	77

5.5	Acoustic output of 25 mg/l CB suspension measured using a hydrophone. The time domain shows there is a sudden rise of pressure followed by a slower fall (a). The frequency domain shows the constituent frequency of the system decreases significantly after 30 MHz (b).	82
5.6	Effect of measurement distance from source, CB concentration and Laser Fluence on the peak pressure. Pressure signal is inversely proportional to the distance from the source (a). Increasing the CB concentration increases the signal linearly (b). Increasing the Fluence increases the pressure non-linearly (c). Data show average \pm standard deviation (SD) (n = 115 replicates) . .	84
5.7	Effect of acetic acid and carbon nanotubes on pressure waves. When water is replaced with non-reacting acetic acid and carbon black is replaced with less chemically active nanotubes there was still pressure detected.	85
5.8	Effect of placing a saran wrap between the cells and the nanoparticles. When cells and nanoparticles are placed on the same side there is significant damage observed whereas when they are placed in either side there is no damage observed.	87
6.1	Physical characterization of carbon black (CB) nanoparticles. (A) Representative dynamic light scattering measurement of hydrodynamic diameter of CB nanoparticle aggregates in DI water suspension at a final concentration of 25 $\mu\text{g/l}$ shows a single peak and no particle settling. Transmission Electron Microscope image (inset) of dried CB nanoparticle aggregates shows the individual spherules constituting the aggregates. The scale bar is 50 nm. (B) Representative acoustic output (pressure) versus time measured using a hydrophone when CB nanoparticle suspension (50 mg/l) was exposed to a single laser pulse at 250 mJ/cm^2 fluence. The frequency distribution calculated from the hydrophone calibration curve reveals a broadband signal up to approximately 30 MHz (inset).	94
6.2	Intracellular delivery of FITC-dextran in Hey A8-F8 ovarian cancer cells. (A) Cells inspected by microscopic imaging show uptake of 70 kDa FITC-conjugated dextran (green) when cells were exposed to laser at 44 mJ/cm^2 for 1 min in the presence of 25 mg/l CB nanoparticles. Cells were also stained with propidium iodide (red), which is a marker of nonviable cells: (I) fluorescence microscopy, (II) brightfield microscopy. Scale bars are 100 μm . (B) Flow cytometric analysis of percentage of cells remaining viable and exhibiting intracellular uptake of dextran is shown as a function of photoacoustic exposure conditions, including laser fluence (mJ/cm^2) and exposure time (min). The asterisk symbol (*) represents statistically different viability compared to sham samples ($p < 0.05$) and the hash symbol (#) signifies that percentage of cells with uptake and viability for a given sample are significantly different ($p < 0.05$). Data show mean \pm standard deviation (SD) with three replicates each (N = 3). (C) Representative flow cytometry histogram plots of FITC-dextran fluorescence are shown for cells incubated with FITC-dextran at four conditions shown in (B): (I) untreated cells (no laser, no CB nanoparticles), and cells exposed to CB nanoparticles and laser at (II) 19 mJ/cm^2 , 7 min (III) 25 mJ/cm^2 , 3 min, (IV) 44 mJ/cm^2 , 1 min.	96

6.3	Uptake of anti-EGFR siRNA (s564) and knockdown efficiency of EGFR mRNA after photoacoustic delivery in ovarian cancer cells. (A) Amount of intracellular siRNA (s564) (in arbitrary units) normalized per 10 ng of total RNA, quantified using qPCR, when Hey A8-F8 cells with anti-EGFR siRNA or NC siRNA were exposed to laser at 19 mJ/cm ² for 7 min in the presence (CB) or absence (no CB) of 25 mg/l CB nanoparticles. (B) EGFR mRNA level normalized relative to GAPDH level measured using qPCR showing knockdown when cells were exposed to laser with CB nanoparticles with anti-EGFR siRNA compared NC-siRNA. Asterisk symbol (*) shows statistically significant differences in uptake and knockdown (p <0.05). Data show mean ± SD (N = 3).	99
A.1	Representative fluorescent and bright field images of tissue sections extracted immediately post treatment under various conditions. Fluorescence imaging shows that there is no propidium iodide signal (PI) signal when there is no carbon black (CB) in the tissue. The CB by itself without laser exposure shows a little signal whereas when laser and CB is used at 100 mJ/cm ² for 2 minutes there is some signal which increases when the laser fluence is increased to 200 mJ/cm ² . Bright field imaging with H & E staining shows the accumulated CB and separation of muscle tissue. Scale bars are 500 μm.	122
A.2	Representative fluorescent and bright field images of tissue sections extracted 2 days post treatment under various conditions. Fluorescence imaging shows that there is decrease in propidium iodide signal (PI) signal in the tissue with carbon black (CB) and no laser compared to immediate extraction. The laser by itself without CB does not show any sign of long term PI staining (thus signifying damage) whereas tissue exposed to 200 mJ/cm ² for 2 minutes in the presence of CB still shows PI signal. Bright field imaging with H & E staining shows the accumulated CB still present even after 2 days and separation of muscle tissue. Scale bars are 500 μm.	123
A.3	Representative fluorescent and bright field images of tissue sections extracted 7 days post treatment under various conditions. Fluorescence imaging shows that tissue exposed to 200 mJ/cm ² for 2 minutes in the presence of CB still shows PI signal. Bright field imaging with H & E staining shows the accumulated CB still present even after 7 days and separation of muscle tissue. Scale bars are 500 μm.	125
A.4	Pixel of PI positive normalized to total pixel counts for analyzed tissue sections as a function of various treatment conditions at different days. Percentage of PI positive area relative to total area in the tissues under various treatment conditions when the muscle is extracted immediately after exposure (A), 2 days post exposure (B) and 7 days post exposure (C) showing PI signal in the exposed sample with CB even after seven days post treatment. Data show average ± standard deviation (SD) (n = 3).	126
B.1	DLS measurement of CB nanoparticles show a mean diameter of ~200 nm with a dispersity of 0.21. The suspension shows no sign of settling or aggregation over time.	132

B.2	Increase of particle temperature with time assuming first the surrounding temperature remains at 23°C and then once the vapor is formed, the bulk temperature goes to 100°C and stays there. This is the worst case scenario of heat transfer between particle and bulk.	133
B.3	Characterization of the CB suspension after the exposure. First the nanoparticle size was determined using DLS after either no exposure to laser till an hour of exposure (a). The absorption spectra were characterized for CB exposed for different time periods using a spectrophotometer to show that there is no statistical difference. (Error bars not shown, n=3).	134
B.4	The acoustic measurement setup which is used to characterize the acoustic output of the system. The hydrophone can be moved in the x,y and z directions relative to the stream of nanoparticles thereby enabling us to map the spatial pressure profile.	135
B.5	Pressure output with an extended time. There is no further signal after the initial signal (as shown in Figure 5.5 in main thesis).	136
C.1	Light absorption by CB nanoparticle solution versus wavelength. Absorption spectra measured using a spectrophotometer shows that CB nanoparticles absorbs across a wide range of wavelengths, including NIR.	142
C.2	Expression of EGFR in Hey A8 F8 cells treated with EGFR-siRNA and NIR laser, but no CB nanoparticles (left bar) and cells treated with CB nanoparticles, but no siRNA or laser (right bar). In both cases, there was no significant knock-down of target EGFR gene (2 tailed t-tests with Welchs corrections, p = 0.5). Expression presented in arbitrary units as mean ± SD (N = 3).	143
C.3	Brightfield (phase contrast) micrographs of Hey A8 F8 cells 24 h post treatment with (A) CB only, (B) anti-EGFR siRNA and laser at 19 mJ/cm ² for 7 min, (C) NC-siRNA, CB nanoparticles and laser at 19 mJ/cm ² for 7 min and (D) anti-EGFR siRNA, CB nanoparticles and laser at 19 mJ/cm ² for 7 minutes. Scale bars are 100 μm.	144
C.4	Uptake of anti-EGFR (s564) siRNA and knockdown of EGFR using Lipofectamine 2000 (Lipo 2000) (A) Amount of intracellular siRNA (s564) (in arbitrary units), normalized to 10 ng of total RNA, quantified using qPCR when Hey A8-F8 cells with anti-EFFR siRNA or scrambled siRNA treated with the manufacturers recommended amount of Lipofectamine 2000. (B) EGFR mRNA level normalized relative to GAPDH level measured using qPCR showing knockdown when cells were treated with Lipofectamine 2000 and anti-EGFR siRNA compared to scrambled siRNA. Asterisk symbol (*) shows statistically significant differences in uptake and knockdown (p <0.05). Data show mean ± SD (N = 3).	145

SUMMARY

Recent progresses in pharmaceuticals and medicine have identified many intracellular targets for future pharmaceuticals development. Intracellular delivery of large therapeutic molecules is a major challenge because of the presence of the plasma membrane. While there are many strategies to load cells with drug, one approach is to use a physical force to porate the cell membrane, thereby letting therapeutic molecules diffuse into the cell. These methods, collectively called physical methods of drug delivery, have the advantage of being generic, fast, and often less cytotoxic compared to the viral and chemical methods of intracellular drug delivery, but cannot simultaneously sustain high levels of uptake and cell viability. Our approach to the problem is to induce controlled and reversible cell damage through pulsed laser irradiation of carbon black (CB) nanoparticles. We first demonstrated intracellular delivery of calcein and FITC-dextran in human prostate carcinoma cells (DU145) and rat cardiomyoblasts (H9c2). We found that both the laser and CB had to be present for the drug delivery to occur significantly. We then characterized and optimized the system for maximal uptake and minimal loss of viability. We studied the effect of number of parameters including laser fluence, time of exposure, CB concentration, and pulsing frequency, and characterized the system efficacy in terms of uptake of marker molecule and viability. We observed efficient uptake in most cases, however cell death was also high at higher fluence and longer exposures. We hypothesized that absorption of laser by CB leads to heating which causes thermal expansion of CB particles followed by vapor bubble formation and/or initiates a chemical reaction between CB and water, leading to generation of pressure waves. Then, the pressure waves and/or the vapor bubbles interact with the cells leading to pore formation from which either the cells recover and drug delivery is achieved or cell death occurs.

In the second half of this study we worked on understanding the underlying causes of cell death. We concluded that cell death is caused by either necrotic death or death through

fragmentation of cells caused by the force generated through laser-carbon interaction. After concluding that cell death is caused by fast mechanical poration, we added poloxamers to mitigate the effect with the rationale that it will plug pores as soon as they are formed. The observed increase in viability through addition of poloxamer leads us to believe that this process is similar to other physical methods like ultrasound and electroporation in some regards.

We then proceeded to understand the details of mechanism of force generation. We devised a technique to measure the acoustic waves generated from the laser-irradiated CB. We observed that increasing fluence and CB concentration leads to increase of pressure waves. We also predicted the maximum particle temperature through bulk temperature measurements and theoretical calculations. Our prediction is that the particle temperature approaches 1000°C for $44 \text{ mJ}/\text{cm}^2$ pulses. Through this we developed the hypothesis that the laser heats the CB leading to thermal expansion, vapor formation and/or chemical reaction leading to generation of acoustic waves. We also concluded that the reaction does not play an important role and that thermal expansion and vapor formation are the two main reasons for acoustic wave generation. Our experiments also suggested that the effect is a near-field effect making the cellular and particle microenvironments very important for successful transient poration of cell membrane..

To demonstrate its potential for medical applications, we applied our technique for intracellular delivery of a real therapeutic molecule. We chose to deliver anti-EGFR siRNA to ovarian cancer cells. Cells exposed to a laser at $18.75 \text{ mJ}/\text{cm}^2$ for 7 minutes resulted in a 49% knockdown of EGFR compared to negative control. We established an alternative way to deliver siRNA to knockdown proteins, for the first time using laser CB interaction.

Finally, we demonstrated the technique in-vivo, wherein we showed that about 30% of the exposed area had uptake compared to non-exposed (sham) controls, but did not quantitatively assess cell death. We believe further optimization will lead to better efficacy in vivo.

The method proposed in this study has several advantages: i) it is fast compared to viral and chemical delivery, ii) it can be applied to a wide variety of cell types and tissue

types, iii) there is no modification required to nanoparticles used in this study which makes it a relatively simple procedure, iv) the necessity of both the CB and laser for the effect to occur results in a localized effect. This technique holds the potential to be an alternative to chemical and biological methods of intracellular drug delivery and we hope someday it will find use in clinic.

CHAPTER I

INTRODUCTION

For most of the industry's existence, pharmaceuticals have primarily consisted of low molecular weight chemical compounds that are dispensed orally (as solid pills and liquids) or as injectables as a bolus. During the past three decades, however, formulations that control the rate and period of drug delivery (i.e., time-release medications) and target specific areas of the body for treatment have become increasingly common [1]. However, this creates a challenge to not only develop new drugs and treatments but also come up with a way to effectively deliver them.

Since development of new drug molecules is expensive and time consuming, an alternative is to increase the efficacy of old drugs by delivering them at controlled rate, and targeting them effectively [2]. The goal of many sophisticated drug delivery systems is to deploy medications intact to specifically targeted parts of the body through a medium that can control the therapy's administration by means of either a physiological or chemical trigger. Many pharmaceutical agents, including various large molecules (proteins, enzymes, antibodies) and even drug-loaded pharmaceutical nanocarriers, need to be delivered intracellularly to exert their therapeutic action inside cytoplasm or onto nucleus or other specific organelles, such as lysosomes, mitochondria, or endoplasmic reticulum. In addition, intracytoplasmic drug delivery in cancer treatment may overcome such important obstacles in anticancer chemotherapy as multidrug resistance [3].

However, the lipophilic nature of biological membranes restricts the direct intracellular delivery of such compounds. The cell membrane prevents big molecules, such as peptides, proteins, and DNA, from spontaneously entering cells unless there is an active transport mechanism, as in the case of some short peptides. Under certain circumstances, these molecules or even small particles can be taken from the extracellular space into cells by the receptor-mediated endocytosis [4]. The problem, however, is that molecules/particles

entering the cell via the endocytic pathway become entrapped in endosomes and eventually end up in the lysosomes, where active degradation processes by the lysosomal enzymes takes place. As a result, only a small fraction of unaffected substance appears in the cell cytoplasm. This result in the situation where many compounds showing a promising potential in vitro cannot be applied in vivo owing to bioavailability problems.

So far, multiple and only partially successful attempts have been made to bring various macromolecular drugs and drug-loaded pharmaceutical carriers directly into the cell cytoplasm, bypassing the endocytic pathway, to protect drugs and DNA from the lysosomal degradation, thus enhancing drug efficiency or DNA incorporation into the cell genome. Techniques like ultrasound induced intracellular drug delivery, electroporation, microinjection, etc. collectively called the physical methods of drug delivery are capable of achieving that, but the primary drawback with these techniques is the tradeoff between high levels of uptake and high viability.

We propose an alternative technique of achieving intracellular drug delivery through exposure of dilute carbon black (CB) solution to pulsed nanosecond laser in the presence of cells. The idea to use laser-CB particle interaction for drug delivery came from the work of Chen and Diebold [5] who demonstrated generation of giant photo-acoustic waves when dilute CB suspension was exposed to nanosecond pulsed lasers [5]. Our labs experience with ultrasound mediated intracellular drug delivery, made us aware of the fact that short, intense pressure fluctuations in a cell system can lead to uptake of molecules. Guided by our previous experience and intuition, we first demonstrated and optimized intracellular drug delivery through the use of a femtosecond laser and CB. The system was quite efficient but femtosecond lasers are expensive and complicated to use, making it less attractive for applications. Encouraged by the femtosecond laser experiments we decided to try the same method with much cheaper, widely available nanosecond laser. This thesis represents the summation of all the effort in that direction. The overall objectives of this thesis can be broadly classified into two parts: i) to characterize the systems efficacy through uptake and viability measurements by varying input parameters and understanding the underlying mechanism of intracellular drug delivery, and ii) applying the system to deliver fluorescent

molecules in vivo and therapeutic like siRNA in vitro to demonstrate its clinical relevance.

The first part of the study focuses on understanding the bioeffects of the laser particle interaction. For that, we characterize the viability (i.e. live cells) and uptake (i.e. viable cells with molecules inside them) by varying a number of parameters like laser fluence, time of exposure, CB concentration, pulsing frequency, etc. to establish the dominant parameters that govern the outcome. We also attempt to determine the cause of cell death post treatment and try to address the issue through the use of various additives. Next, we study the underlying mechanism of generation and nature of the physical force that results in membrane poration, by measuring the pressure and temperature of the system. The final part of this thesis focuses on applying the technique to assess a future medical application. For that, first the system is used to deliver siRNA in vitro to demonstrate knockdown of EGFR protein in ovarian cancer cells and finally, we show a proof of principle study of intracellular delivery of propidium iodide (PI) in murine TA muscles.

In the subsequent chapters we will first ask questions and then formulate hypotheses to answer them, and then test those hypotheses through experiments and calculations. Each chapter will describe in detail the questions asked, the hypotheses proposed, experimental design to test the hypotheses, and interpretation of results followed by a conclusion. We also propose recommendations for future advancement at the end.

CHAPTER II

BACKGROUND

In the last century significant advancement in pharmaceuticals has resulted in eradication of deadly diseases like small pox; led to reduction of 99% of the deaths caused by diphtheria, mumps, pertussis and tetanus in the US [6]. With the advent of new kinds of drugs, it became equally important to come up with ways to deliver them [7, 8]. Traditionally the oral route was preferred, owing to its non-invasive nature and ease of delivery, but unfortunately, adequate peptide or protein drug delivery has not yet been attained via this route. This is, in part, a consequence of the acidic conditions of the stomach, the first-pass effect of the liver (i.e. the loss of drug owing to metabolic processes before entering the systemic circulation) and the resistance exerted by the intestine, which alters, destroys or reduces absorption of nearly all macromolecules, thereby reducing their bioavailability [9]. There are alternative routes of delivery like nasal, transdermal, intravenous, etc., but they suffer from drawbacks like whole body exposure and limitations on the types of drugs that can be used [10]. This, in part, led to discovery of newer techniques to deliver drugs that are targeted towards the specific sites in the body. At present drug delivery is a vast and important field in its own [11].

A lack of good drug delivery technique can not only hamper effectiveness of traditional medication [12, 13] but will lead to further complications to future medication techniques like gene corrections, RNA interference (RNAi) and cell therapy. With the progress in biotechnology, it has been possible to identify a lot of intracellular targets that, if treated will lead to better therapy. Most pharmaceutical agents have primary targets within cells and tissues; ideally, these agents may be preferentially delivered to these sites of action within the cell [14]. This group includes preparations for gene and antisense therapy, which have to reach cell nuclei; proapoptotic drugs, which target mitochondria; lysosomal enzymes, which have to reach the lysosomal compartment; siRNA and mRNA which needs to reach

into the cytoplasm [3].

2.1 Current Intracellular Drug Delivery Techniques

In order to deliver drugs to intracellular targets, a strong barrier called cell membrane must be overcome. Cell membrane is an extremely hard barrier to overcome because it is made of highly structured lipid bilayer, which regulates the entry and exit of most of the external molecules. Only a very few small molecules can make it across the cell membrane through diffusion. Cell membrane being negatively charged does not interact with a lot of naturally occurring macromolecules. P-glycoprotein pumps push drugs out of the cells [15]. Big molecules can only make it into the cells through a collective process of cells called endocytosis which eventually leads the drugs to highly acidic endosomes and are subject to lysosomal degradation [16, 17]. Because of the nature and complexity of intracellular drug delivery, there are varieties of techniques and approaches that can be used to achieve the same. Most intracellular drug delivery methods can be classified into 3 kinds of techniques viz. a) Chemical b) Biological and c) Physical. Each method has its own advantages and shortcomings which would be discussed in the following section.

2.1.1 Chemical Methods

Chemical methods involve modifying the drug chemically to make the drug more stable, changing the drug formulation or encapsulating them in a polymeric material to have a longer circulation in blood or embedding the drug in porous structure to get a sustained release effect. These techniques also give an either precise targeting effect or a control of the release profile. In the past few decades there has been a growing interest in delivering effective drugs, proteins, peptides in specific targets using nanoparticles [12, 18, 19]. Nanoparticles are man-made materials which are in the 5 - 200 nm size range [14]. The use of nanoparticles in science is called nanotechnology [20]. Due to its small size, it generally has a higher efficiency of being taken up by cells, and gets cleared more efficiently unlike microparticles which stay in the body for extended periods of time.

Based on the materials used and the method of preparation various kinds of nanoparticles can be manufactured, like inorganic nanoparticles [21], polymeric nanoparticles [22],

nanocrystals [23], solid lipid nanoparticles [24], liposomes [25] and dendrimers [26]. These nanoparticles can be engineered to target various intracellular targets with varying degree of success. Drugs encapsulated within a shell or adsorbed on a surface provide a protection of the naked drug from a systemic response. Examples of this technique are nanoshells, polymeric nanoparticles, solid lipid nanoparticles and liposomes. Among all of these technologies, the most notable is the use of liposomes, where the drug is encapsulated in a phospholipid bilayer structure, which prevents immune response and increases the circulation period in the body. They are also amphiphilic and therefore are conducive to surface modification which can then be used to target specific cells and provide stealth from immunity [27, 28]. The protective activity has a special relevance to RNA delivery because of the presence of RNAase in the tissue of animals. Polymeric nanoparticles can also be used to provide a sustained release of a drug once they are taken up by cells.

Cell penetrating peptides and cationic lipids are also possible ways of delivering drugs and nucleic acids into the cell by overcoming the electrostatic force of the cell membrane. Complexes of polymers with DNA, called polyplexes [29], are used for their high loading and low toxicity [30]. The general drawbacks associated with chemical methods are associated with the stability in the systemic circulation, clearance of the nanoparticles, toxicity and endosomal and lysosomal degradation [31-33].

2.1.2 Biological Methods

Biological methods, also known as viral vector techniques, are methods which use a biological carrier mostly viruses to deliver drugs to specific tissues. Virus has been evolutionarily very good at infecting tissues and therefore serves as a potentially good carrier for targeted drugs. This technique has been traditionally chosen as a preferred method for gene delivery because of the ease of design and high efficiency [34]. The use of retroviruses [35] and adenoviruses [36] and herpes simplex virus are some examples of the carrier. But because large scale production of virus based drug is extremely expensive and high host immunogenicity associated with this technique has led to decline of interest in this method [37]. With the advent of other methods, biological methods are more and more at a disadvantageous

position in clinical medicine [38].

2.1.3 Physical Methods

An alternative technique to deliver drugs to cells is to use a physical force that temporarily disrupts the membrane and allows the molecules to either diffuse in or are driven electrophoretically to cause uptake of molecules [39]. Membrane disruptions leads to direct cytosolic delivery bypassing the endocytotic pathway and the externally controlled field can be manipulated to change the pore size leading to uptake of different kind of molecules by the same force [40, 41]. Generally bigger pores and pores that remain open for a longer duration causes uptake of bigger molecule but there is a potential risk of cell death because of apoptosis triggered by Ca^{2+} efflux or necrosis [42]. The primary challenge is to optimize the conditions to maximize uptake while minimizing cellular deaths. Physical methods have gained interest in the drug delivery world because of their ease in use, genericity and targeting properties. Some examples of physical methods are listed as follows:

2.1.3.1 Electroporation

Electroporation or electropermeabilization is a process of increasing cellular permeability caused by an externally applied electrical field. The field causes destabilization of the cell membrane leading to enhanced permeability. The field then, in some cases of charged molecules like DNA and protein, drives the molecules across the membrane electrophoretically achieving drug delivery of big molecules [43, 44]. Gene transfer by electroporation has been successfully used to deliver genetic materials across broad range of cells both in-vitro and in-vivo [45, 46]. The approach becomes increasingly invasive, as the tissue becomes more and more non-accessible. There have been reports of cell death by apoptosis and long term effects on cells after being subject to electroporation. The efficacy of the method is highly dependent on the local distribution of electric field in the tissue and therefore has to be optimized from tissue to tissue [47]. Even though this sensitivity has prevented commercialization of the technology in the US, electrochemotherapy is approved in Europe. A more recent approach is a technique termed as electron avalanche transfection which

involves delivery of DNA using high voltage plasma discharge, following very short (microsecond) pulses. This technique has been shown to be more efficient in terms of uptake and viability compared to electroporation [48].

2.1.3.2 Ultrasound

Ultrasound which is primarily used for imaging has also been used to achieve intracellular drug delivery [49]. Ultrasound-mediated delivery occurs due to the transient mechanical disruption of the cell membranes by acoustically-induced bubble activity or acoustic cavitation [50-52]. It's a relatively fast, non-invasive tool for drug delivery and gene delivery. This method has been used in conjunction with viral vectors [53] and microbubbles [54] to obtain targeted and efficient drug delivery. The method involves focusing a beam of ultrasound into the desired tissue externally. This causes heterogeneous effects because the sound attenuates and reflects heterogeneously from the body. The underlying mechanism of membrane disruption by ultrasound might be caused by acoustic cavitation which is intrinsically a heterogeneous effect [55]. Cell death through this method either occurs by lysis (fragmentation), necrosis or apoptosis. If the intensity of ultrasound is increased, it leads to more cell death by lysis suggesting a mechanical disruption of cell membrane during the ultrasound exposure [42, 56].

2.1.3.3 Microinjection

This technique involves direct delivery of drugs or DNA materials into the cell using a glass micropipette under a microscope. This technique has the advantage of high transfection efficiency and homogenous response as the materials are injected directly into the cells. This has been used primarily for pronuclear injection for producing transgenic mice and for in vitro fertilization in clinical medicine [57]. Unfortunately, the technique involves a highly skilled person who has to inject cells one by one leading to an extremely low throughput [58]. This drawback has limited the use of this technique.

2.1.3.4 Particle Bombardment

This is primarily an in-vitro method, which utilizes a gene gun to deliver a payload of an elemental particle of heavy metal coated with plasmid DNA [59]. This is also referred to as bioballistics. Even though so far it has been primarily used in plant cells it has a potential to be used in mammalian cells as well. They have been used to deliver DNA vaccines and transform *C. elegans*, as an alternative to microinjection [60]. Because this technique involves heavy metals, its use is limited either because of cellular toxicity or price per injection. In-vivo application of this technique is limited to skin and shallow tissue targets [61, 62].

2.1.3.5 Magnetofection

Magnetofection involves the use of magnetic fields to concentrate iron oxide particles containing nucleic acid into target cells. First, the nucleic acids are associated with cationic magnetic particles; next they are concentrated in the vicinity of cells supported by appropriate magnetic field. But the primary delivery occurs through endocytotic pathway [63]. Nucleic acids are then released into the cytoplasm depending on the formulation used from the endosome. So far, most of the studies involving magnetofection are in-vitro studies though there is a promising potential of remote targeting in-vivo using magnets to tumors and other hard to access areas [64].

2.1.3.6 Advantages of Physical Methods

Physical methods of drug delivery rely on an external physical force that causes temporary disruption of cell membrane. This makes them relatively less sensitive to type of drug and type of cells compared to its chemical and biological counterparts. Therefore, these methods are considered generic and platforms are easily transferable to newer systems. Additionally, the uptake occurs directly into the cytosol bypassing the endocytotic pathway resulting in a whole cytoplasm delivery and not just local delivery to endosome, while avoiding endosomal degradation of drug [39]. Physical methods are generally much faster than other types of delivery methods (delivery timescale in minutes) because there is an active pore that is

created on the cell membrane which results in active delivery and does not rely on the inherent capabilities of cell to uptake the drug which are comparatively slower (delivery timescale in hours). In physical methods, little to no modification of the drug is required because the drugs are actively delivered to cells without any receptor binding or chemical targeting. The advantage of using naked drug is in less off-targeting, less toxicity and ease of preparation of samples. Physical methods involve the use of a physical force and generally just the naked drug and sometimes inert materials that do not take part in bioeffects generally. The result is a relatively simple and non-toxic system [65, 66]. Nevertheless, physical methods suffer from a drawback of high cell death associated with high uptake because forces that cause the delivery to occur is also responsible for cell death. Therefore the greatest challenge is to optimize the condition such that there is very little cell death but coupled with maximal viability [65].

2.1.4 Lasers in medicine

A laser is a device that emits light through a process of optical amplification based on the stimulated emission of electromagnetic radiation [67]. The term laser stands for light amplification by stimulated emission of radiation. A laser consists of a gain medium, a mechanism to supply energy to it, and something to provide optical feedback [68]. The gain medium is a material with properties that allow it to amplify light by stimulated emission. Light of a specific wavelength that passes through the gain medium is amplified (increases in power). The process of providing external energy to the gain medium, in the form of either electric current or light at a different wavelength than the laser output, is called pumping and is usually achieved by a flash lamp or a seed laser. The feedback mechanism, in most lasers, is provided by an optical cavity which are generally a pair of mirrors that let light bounce back and forth passing light every time through the gain medium. When number of atoms in excited state is more than atoms in ground state, population inversion is achieved in the gain media, and the amount of stimulated emission due to light that passes through is larger than the amount of absorption, causing light amplification. Typically one of the mirrors in the optical cavity is partially transparent allowing some of the light to

pass through causing the final output beam.

Depending on the pumping mechanism and the optical cavity, lasers can be classified into two different groups; continuous lasers and pulsed lasers. Continuous lasers have a continuous beam output and require the population inversion to be replenished steadily. In some lasing media this is impossible. In some other lasers it would require pumping the laser at a very high continuous power level which would be impractical or destroy the laser by producing excessive heat. Such lasers cannot be run in CW mode. In pulsed lasers, the output is pulsed and can be achieved by pulsed pumping, mode locking or Q-switching.

Pulsed pumping involves pumping the laser material with a source that is itself pulsed, either through electronic charging in the case of flash lamps, or another laser which is already pulsed. Examples of such lasers are excimer lasers and copper vapor lasers, and they can never be used in the continuous mode. Mode locking technique can produce extremely short pulses (~ 10 femtoseconds) [69]. These pulses will repeat at the round trip time, that is, the time that it takes light to complete one round trip between the mirrors comprising the resonator. Ti:Sapphire is an example of such laser, and is primarily used because it has a very wide gain bandwidth and can thus produce pulses of only a few femtoseconds duration. These lasers are used to maximize the non-linear effect of a system by depositing energy at a very fast pace, causing optical breakdown in some cases [70].

In a Q-switched laser, the population inversion is allowed to build up by introducing loss inside the resonator which exceeds the gain of the medium to store maximum possible pump energy in the laser medium. Then, after that, the introduced loss mechanism (often an electro- or acousto-optical element) is rapidly removed (or that occurs by itself in a passive device), allowing lasing to begin which rapidly obtains the stored energy in the gain medium. This results in a short pulse incorporating that energy, and thus a high peak power [71]. Nd:YAG lasers are a common examples of Q-switched lasers and pulse lengths can be in the order of nanoseconds. Typically these lasers are much cheaper compared to Ti:Sapphire femtosecond lasers. On May 16, 1960, Theodore H. Maiman operated the first functioning laser [72] at Hughes Research Laboratories, Malibu, California. Only

two years later, in 1962, a dermatologist named Leon Goldman used it to remove a tattoo. Since the inception of lasers, it found its use in medicine. As the years progressed its applications widened and currently they are used in a variety of applications such as angioplasty [73], cancer diagnosis [73, 74], cancer treatment [75], cosmetic applications such as laser hair removal, tattoo removal, dermatology, lithotripsy [73], mammography, medical imaging, microscopy, ophthalmology (includes LASIK and laser photocoagulation), optical coherence tomography, prostatectomy, surgery [76] etc. Lasers are attractive because they are optically coherent which enables the light to be focused and targeted consistently, they are generally monochromatic and therefore can be used to interact with specific targets and finally they can generate very high peak power (mode locked and Q-switched lasers) which give them unique characteristics and properties. The main challenge with laser is to find the right wavelength, uniform beam profile and control the energy at a specific site in the body especially in the tissue situated deep in the body.

2.1.5 Drug Delivery using laser

Some methods of intracellular drug delivery have used lasers. Methods like optoporation [77] and optoinjection [78] are used to deliver exogeneous molecules directly into the cells. Optoporation uses a focused laser light (less than 1 μm diameter) to thermally damage cell walls and deliver molecules into cells on a cell by cell basis. Optoinjections uses laser to create shockwaves through the use of laser absorbing media (typically polyimide) to mechanically damage cells. Laser particle interaction has also been shown to lead to creation of acoustic waves that have a potential to disrupt cell membrane [79, 80]. Another way of creating a shockwave is to use a shocktube [81] which can then be used to deliver drugs into the cells. Indirect methods which use laser for intracellular delivery involve nanoparticles loaded with drugs which are released through shining of laser light on them, incurring a time and spatial control over the release of drug [78, 82].

The generation of shockwave using laser has been subject to a lot of research lately. A complete field of photo-acoustics has come forth as a result [83]. Drug delivery using

shockwave generated by lasers is in reality a two-step process: the first being the transduction of laser energy to acoustic waves and the second step is the interaction of that pressure wave with the cell to cause membrane disruption. Shockwave generation has been attributed to optical breakdown (plasma formation), ablation, thermoelastic expansion or vapor formation [84]. The shockwave and acoustic waves generated from these mechanisms are thought to temporarily disrupt the cell membrane allowing drugs and other molecules to diffuse in [85-87]. The exact nature of pressure wave and cell membrane interaction which causes membrane disruption is not well known and is still subject to debate. It is however, believed that once the membrane disruption occurs the drug delivery into the cells occur because of passive diffusion. Generation of pressure waves through laser irradiation poses several advantages in the sense that there is more spatial control over the pressure wave generation areas.

2.2 Carbon Nanoparticles in Medicine

Carbon occurs in various forms such as carbon black, graphite, nanotubes, fullerenes etc. Carbon nanotubes (CNTs) are being widely used for targeted drug delivery research, owing to their high internal volume and ease of functionalization of external surface. A popular version of nanotubes is the use of soluble fullerene derivatives such as C60 which can be easily used in drug loading and formulations [88]. Direct non-endocytic delivery of plasmid DNA was also achieved using a technique called nanotube spearing [89]. But unfortunately the toxicity of nanotubes is still under question and in some cases has been shown to be acutely toxic to cells [90]. Carbon dots (C-dots) have been used in particle tracking and imaging and are said to be non-toxic to cells [91].

Carbon black (CB) is another form of carbon and is one of the major components of India ink. CB is composed of very small primary particles, which fuse to form branched aggregates. Aggregates are the smallest functional unit of CB. They are formed through the fusion of smaller units, called primary particles, into a three dimensional branched chain structure [92]. They have found use as medical tattoos and markers for tissue and have been also used as a model nanoparticle dye in some cases.

2.3 Laser Particle Interaction

Laser particle interaction has found a significant place in medicine and other fields. In photo-acoustics metal particles are used to map out the tissue region in vivo and also used for particle tracking [93, 94]. In drug delivery laser particle interaction has mainly focused on gold nanoparticles. Gold nanoparticles are preferred and have been used in various ways to deliver drugs because of non-toxic nature and tunability to specific laser wavelengths. For example, gold nanoshells have been used to load drugs inside and them, and targeted to specific sites such as tumor and then once they reach the specific site, drug is released through thermal ablation of the shell using a tuned laser leading to controlled drug delivery [95]. Another way to use gold nanoparticles is to incubate cells with gold nanoparticles for a few hours and once the gold particles are taken up, they can be irradiated with laser to cause either endosomal escape [96] or cellular death [97]. By tuning the surface chemistry of these nanoparticles can be preferentially taken up by cancerous cells thereby only selected cell deaths can be caused. Most of the studies required gold to be either conjugated to membrane surface [98, 99] or internalized into the cells to have an effect. Unfortunately gold nanoparticles are hard to prepare, expensive and are not the most efficient absorbers of lasers especially at wavelengths other than 532 nm because the gold can melt at certain fluences of the laser and change its shape and stop interacting with the laser. Therefore it is desirable to find other candidates than can more efficiently convert laser energies to either heat or sound to cause more efficient disruption of cell membrane. Other studies have shown that pressure wave and bubble formation occur at an interface of metal and water [84].

2.3.1 Laser Carbon Interaction

Carbon black has a higher absorption across all wavelength compared to gold and no structure or shape modifications are needed in carbon to make it absorb light of various wavelength and therefore makes it a competitive candidate for absorptive media for laser. In 1995, Chen et al. showed production of acoustic wave due to laser irradiation of carbon suspension [100]. Irradiation of carbon nanoparticle suspensions with high power pulsed laser

radiation have been reported to produce shock waves [101, 102], various chemical species [103, 104], sonoluminescence [105] and an anomalously large sound wave called the "Giant Photoacoustic Effect" [100]. These pressure forces were believed to be caused by the sudden volume change caused by vaporization of fluid surrounding the heated carbon particles and potentially because of the reaction of this vapor with carbon to initiate the endothermic carbon-steam reaction. Chemical reactions were also reported when the suspensions were made in non-aqueous solvents like toluene and benzene [104]. Formation of gas bubbles due to fluid vaporization around the heated particles as well as the product gases of chemical reaction are also believed to cause cavitation bubble dynamics which may lead to the strong pressure forces [106, 107]. This similarity with ultrasound led to the belief that it might act as a potential drug delivery technique like ultrasound. It had the potential advantages of better control over the acoustic field both spatial and temporal. The acoustic sources (CB particles) are in the vicinity of the target therefore by varying the concentration a greater control over the field is achieved. Chakravarty et. al. demonstrated the use of CB to deliver molecules efficiently into DU145 cells by laser irradiation of carbon suspension in the presence of cells [108]. But the mechanism of action is so far poorly understood and a part of this thesis is dedicated to understanding some of the basic mechanisms that might be responsible for efficient drug delivery.

2.4 RNA Interference and siRNA

RNA interference (RNAi) is a recently described mechanism for inhibiting gene expression. It was originally identified in plants, fungi, and worms when introduction of control sense oligonucleotides into cells unexpectedly led to reduced gene expression [109-111]. RNAi-mediated gene silencing suppresses gene expression by several mechanisms, including the targeted sequence-specific degradation of mRNA, translational repression, and the maintenance of silenced regions of chromatin. Silencing of endogenous genes regulates basic biological processes, including the transition from one developmental stage to the next [112]. In addition, RNAi is used as a form of primitive immunity to protect the genome from invasion by exogenous nucleic acids introduced by mobile genetic elements, such as

viruses and transposons. Interest in RNAi soared when it was shown that RNAi also occurs in mammalian cells [113]. This raised the prospect of harnessing this potent and specific gene-silencing mechanism for biomedical research and therapy. In the past few years, there has been an RNAi revolution as researchers have sought to understand how RNAi works to regulate gene expression, have used it to perform reverse genetics in mammalian cells, and have begun to explore its potential therapeutic use.

RNAi pathways have been most fully described in *Drosophila*, but mammalian complexes and mechanisms are thought to be similar. The effector molecules that guide mRNA degradation are small [21- to 25-nucleotide (nt)] dsRNA, termed small interfering RNAs (siRNAs), produced by the cleavage of long dsRNAs [114-116]. These short RNAs are produced by the cytoplasmic, highly conserved Dicer family of RNase IIIlike enzymes, resulting in a characteristic 2123-nt dsRNA duplex with symmetric 2- to 3-nt₃ overhangs [113, 117]. RNAi can also be initiated by introducing chemically synthesized siRNAs into cells. The siRNAs are taken up into a multisubunit ribonucleoprotein complex called RISC (RNA-induced silencing complex). The antisense (guide) strand of the siRNA directs the endonuclease activity of RISC to the homologous (target) site on the mRNA resulting in mRNA cleavage [118].

Some have touted RNAi as the next new class of therapeutics. Because all cells are thought to contain the machinery to carry out RNAi and all genes are potential targets, the possible applications for medicine are, in principle, unlimited. This widespread applicability, coupled with relative ease of synthesis and low cost of production (especially compared to proteins such as antibodies or recombinant growth factors at the concentration needed for therapeutic effects), makes siRNAs an attractive new class of small-molecule drugs. In addition, siRNAs are chemically stable and can be stored lyophilized without refrigeration. Moreover, as they enter the RNAi pathway later, siRNAs are less likely to interfere with gene regulation by endogenous microRNAs. The sequence specificity of RNAi, even when off-target effects are considered, promises potent therapies with little toxicity due to off-target gene silencing. This high specificity also implies that the application of RNAi in some instances, such as to treat viral infections or cancer, might lead to resistance due to

sequence mutations. This has proved to be the case in several in vitro studies suppressing viral replication by RNAi (e.g., poliovirus [119] and HIV-1 [120, 121]). But nevertheless, siRNAs are the class of RNAi therapeutics that are most advanced in preclinical and clinical studies. Major drawback for siRNA includes the poor pharmacokinetic property and biological permeability restrictions, off-target effects and interferon response [122]. In particular, siRNAs longer than 30 nucleotides, in specialized highly sensitive cell lines and at high concentrations, lead to the activation of the immune system [123]. Also, a low transfection efficiency, poor tissue penetration because of polyanionic nature [124]. siRNA stability by itself is also one of the major issues because siRNAs, like most RNA molecules, are readily degraded by RNases, which are ubiquitous both in the extracellular and the intracellular space. Delivery remains a major hurdle for RNAi therapy, since siRNAs do not cross the mammalian cell membrane unaided and since many of the transfection methods used for in vitro studies cannot be used in most in vivo settings. There are two common strategies for delivering siRNAs in vivo [125]. One is to stably express siRNA precursors, such as shRNAs, from viral vectors using gene therapy; the other is to deliver synthetic siRNAs by complexing or covalently linking the duplex RNA with lipids and/or delivery proteins.

In vitro siRNAs have been used to knockdown a variety of targets in vitro across multiple cell lines. In vivo they have been used to target a variety of targets like, VEGF [126, 127] and $TGF\beta R2$ [128], SARS [129], Ebola L gene [130]. The current method of delivery are either using liposomes, nanoparticles formulations, ligand targeted lipoplexes, nano emulsions, nanoparticles and chemical modification to siRNA itself to increase stability [131].

Lasers have been used to deliver genetic materials in the past. siRNA has been delivered into the cells using laser in a thermal mechanism [132]. Nanoshells are loaded with siRNA and once they have been uptaken by the cells, they are released by exposing to lasers which aid them to escape the endosomal pathway [133].

CHAPTER III

EFFICIENT INTRACELLULAR DELIVERY OF MOLECULES WITH HIGH CELL VIABILITY USING NANOSECOND-PULSED LASER-ACTIVATED CARBON NANOPARTICLES

Conventional physical and chemical methods that efficiently deliver molecules into cells are often associated with low cell viability. In this study, we evaluated the cellular effects of carbon nanoparticles believed to emit photoacoustic waves due to nanosecond-pulse laser activation to test the hypothesis that this method could achieve efficient intracellular delivery while maintaining high cell viability. Suspensions of DU145 human prostate carcinoma cells, carbon black (CB) nanoparticles and calcein were exposed to 5 - 9 ns long laser pulses of near-infrared (1064 nm wavelength) light and then analyzed by flow cytometry for intracellular uptake of calcein and cell viability by propidium iodide staining. We found that intracellular uptake increased and in some cases saturated at high levels with only small losses in cell viability as a result of increasing laser fluence, laser exposure time, and as a unifying parameter, the total laser energy. Changing interpulse spacing between 0.1 s and 10 s intervals, showed no significant change in bioeffects, suggesting that the effects of each pulse were independent when spaced by at least 0.1 s intervals. Pre-treatment of CB nanoparticles to intense laser exposure followed by mixing with cells also had no significant effect on uptake or viability. Similar uptake and viability were seen when CB nanoparticles were substituted with India ink, when DU145 cells were substituted with H9c2 rat cardiomyoblast cells and when calcein was substituted with FITC-dextran. The best laser exposure conditions tested led to 88% of cells with intracellular uptake and close to 100% viability, indicating that nanosecond-pulse laser-activated carbon nanoparticles can achieve efficient intracellular delivery while maintaining high cell viability.

3.1 Introduction

Many pharmaceutical agents in development and used clinically need to be delivered intracellularly to have their intended therapeutic effect [3]. Inside the cell they have various targets, including nuclear targets for gene transfection, gene correction and other gene-based therapies [134]; mitochondrial targets for certain proapoptotic drugs [135, 136]; and other cytoplasmic sites, including those needed for protein knockdown by RNA interference using siRNA or miRNA [137]. However, the highly structured and lipophilic nature of the cells plasma membranes generally blocks the direct intracellular delivery of such compounds, such that most molecules other than small ions enter cells by an active transport mechanism, such as receptor-mediated endocytosis [16]. Uptake via that route can be accessed through the use of lipid and polymer nanoparticles, especially if decorated with receptor-targeted ligands [138]. However, such chemical delivery systems can be associated with cytotoxicity and drugs administered by that route can be subject to lysosomal degradation after internalization [17]. Viral vectors also harness natural mechanisms of intracellular delivery, but are primarily useful only for DNA delivery and suffer from risks of virus-induced toxicity [139].

Another approach to intracellular delivery uses physical forces to transiently and reversibly disrupt the cell membrane, thereby allowing molecules to directly enter the cytoplasm of cells either by diffusion or, in some cases, by electrophoretically driven processes through short-lived transmembrane pores [39]. Examples of such methods are electroporation [140], ultrasound-mediated intracellular delivery [49, 141, 142] and microinjection [143]. Some methods of intracellular delivery have used lasers, for example, to generate acoustic waves from a shock tube to induce uptake by a mechanical mechanism [144, 145], to heat nanoparticles to induce uptake by a thermal mechanism [146-150], to heat nanoparticles for controlled release of encapsulated drugs [82] or to heat nanoparticles to cause cell death [151]. A common limitation of intracellular delivery methods is a trade-off between achieving high levels of intracellular uptake and maintaining high levels of cell viability, since efficient uptake among viable cells is often associated with significant cell death.

In this study, we investigated a method of intracellular delivery that uses laser-activated

carbon black (CB) nanoparticles. In this approach, nanosecond pulses from an infrared laser are used to interact with CB nanoparticles, which are believed to emit acoustic waves by a so-called giant photoacoustic effect [5] that mechanically acts on the cell membrane to create transient pores through which molecules can enter the cell. In our previous work, we used a femtosecond laser operating at 810 nm wavelength to demonstrate intracellular delivery by this approach [152]. In the present study, we build off those initial findings in two ways. First, we switched from the expensive and complex femtosecond laser used before to a much simpler and less expensive nanosecond pulse laser. Second, we examine the effects of varying laser exposure conditions over a range of parameters in order to optimize uptake and viability, as well as to gain insight into mechanisms of action.

3.2 Methods

3.2.1 Laser Apparatus

The Nd:YAG infrared laser (Powerlite II Plus, Continuum, Santa Clara, CA) available in the High-Strain-Rate Laboratory in the School of Materials Science and Engineering was used to apply pulses of 1064 nm wavelength, 5 - 9 ns pulse length, and 50 - 175 mJ energy per pulse. Pulses were applied at a repetition rate of 10 Hz (i.e., 10 pulses per second), unless otherwise stated. In some cases, pulses were applied at 1 Hz or 0.1 Hz. The energy was varied by manipulating the amplifier voltage of the system. The beam was passed through a Faraday isolator to prevent back reflection. The 12 mm-diameter laser beam was passed through a 9 mm-diameter aperture to block the edges of the beam and thereby obtain a more uniform top-hat profile. The resulting 9 mm-diameter beam was then usually diverged to 21.4 mm diameter using a lens to illuminate the entire cuvette (exposure area of 4 cm²), unless stated otherwise. In some cases, the beam was used directly without diverging (exposure area of 0.63 cm²). Sham exposures were used as negative control experiments, where solutions containing cells, calcein and CB nanoparticles went through all the same steps as exposed samples (see below), except that the laser was not turned on. Another negative control involved only cells without CB nanoparticles or calcein.

3.2.2 Cell Preparation

Human prostate carcinoma cells (DU145, American Type Culture Collection, Manassas, VA) and rat cardiomyoblast cells (H9c2, courtesy of Dr. Mike Davis, Emory University, Atlanta, GA) were cultured as monolayers in a humidified atmosphere of 95% air and 5% CO₂ at 37°C in RPMI-1640 medium (Cellgro, Herndon, VA) and DMEM (Cellgro), respectively, which was supplemented with 100 g/ml penicillin-streptomycin (Cellgro) and 10% (v/v) heat inactivated FBS (Corning, Palo Alto, CA). For each experiment, cells at 80-90% confluence were harvested by trypsin/EDTA (Cellgro) digestion, washed using fresh growth medium with FBS and re-suspended in RPMI at a cell concentration of 10⁶ cells/ml. The DU145 cells [153] were used as a model cell line in most experiments because they are well characterized and have been used extensively in our previous related studies [50, 55, 152]. In some experiments H9c2 cells [154] were used as an alternative model representing a different cell type from a different species.

3.2.3 Nanoparticle Preparation

To prepare the CB nanoparticle solution, 20 mg of CB (Black Pearls 470, Cabot, Boston, MA) were added to 50 ml of 0.013% (v/v) Tween 80 (Sigma-Aldrich, St. Louis, MO; added to reduce aggregation and settling of the nanoparticles) in DI water and sonicated for at least 15 min to obtain the final CB solution at a concentration of 400 mg/l. The size of the individual CB nanoparticles was 25 nm, but they were aggregated into larger particles of 189.3 ± 1.5 nm ($n = 3$) diameter with a dispersity of 0.16 ± 0.03 ($n = 3$), as determined from dynamic light scattering measurements. The individual nanoparticles could not be further separated by sonication (neither bath sonicator nor a more powerful needle sonicator). After making the 50 ml solution of CB nanoparticles, it was aliquoted into smaller 1.5 ml samples.

India ink (Chartpak, Leeds, MA), as obtained from the manufacturer, was first diluted to 1% (v/v) in DI water (without surfactant), which served as the stock solution for experiments. Because the manufacturer did not provide technical information about the ink, we dried 1 ml of the India ink solution on wax paper and determined the solids content to be

129 ± 1.45 mg/l ($n = 3$) by weighing the dried mass. Dynamic light scattering measurements suggested that the mean diameter of the India ink nanoparticles was 110.6 ± 0.74 nm ($n = 3$) with a dispersity of 0.23 ± 0.01 ($n = 3$).

Relative absorption by the India ink stock solution was determined by measuring absorption at 1000 nm wavelength and comparing it with the absorption of the CB nanoparticle stock solution of the same volume, which determined that the ratio of the absorption of the India ink stock solution to the CB nanoparticle stock solution was 2.91 ± 0.1 ($n = 3$). For experiments where India ink and CB nanoparticles were added at the same level of laser absorption, the volume of India ink stock solution added to a sample was 2.91 times less than the volume of CB nanoparticle stock solution.

3.2.4 Sample Exposure

A volume of 520 μ l of cells at a concentration of 10^6 cells per ml was suspended in RPMI, transferred to 1.5 ml microcentrifuge tubes and stored on ice until exposure. CB nanoparticle stock solution was added to achieve a final concentration of 25 mg/l CB nanoparticles, unless otherwise noted. In some experiments different concentrations of CB were used. High purity calcein (Molecular Probes, Eugene, OR) was used as an uptake marker and was added from a stock solution at a final concentration of 10 μ M. In some experiments calcein was replaced by FITC labeled dextrans (Sigma-Aldrich) of 10 kDa, 70 kDa and 500 kDa molecular weights at a concentration of 10 μ M. The final solution was mixed thoroughly by vortexing and then exposed to laser in cuvettes (37-PX-2, Starna Cuvettes, Santa Clara CA) made from Pyrex glass. The total volume of the cuvette was 600 μ l. The top part of the cuvette was cut at 2 mm from the base of the neck to facilitate transfer of liquids. A total volume of 563 μ l of the mixture was transferred to the cuvette using a transfer pipette. The cuvette was placed in a custom-made stand to keep it stationary during laser exposure.

After laser exposure, cells were transferred back to microcentrifuge tubes and stored on ice to reduce uptake due to endocytosis until all the samples were done. Propidium iodide (Invitrogen, Grand Island, NY) was added at a concentration of 7.5 μ M and cells were incubated for at least 10 min to label necrotic and late apoptotic cells. Next, cells

were centrifuged at 500 g for 6 min and washed with PBS (Cellgro) supplemented with 10% FBS twice. After the third centrifugation, the cells were suspended in PBS and then transferred to flow cytometer tubes or were put on a microscope slides and cover slipped for fluorescence imaging.

3.2.5 Cytotoxicity of CB Nanoparticles

Dimethyl thiazoldiphenyl tetrazoleum (MTT) assay was performed to assess the cytotoxicity of CB nanoparticles on the cells. CB nanoparticles were added at concentrations ranging from 50 mg/l to 400 mg/l to DU145 cells that were monolayer cultured on 96 well plates. The cells were then incubated for either 24 h or 72 h with the CB nanoparticles. The cells without CB nanoparticles served as the positive control. The negative control was created by incubating cells with 70% methanol for 30 min. CB nanoparticles were removed from the solution by centrifugation and absorbance measured at 570 nm was used to determine the number of viable cells.

3.2.6 Analysis and Quantification

Cells were imaged using a Zeiss LSM META/NLO 510 multiphoton laser confocal microscope (Zeiss, Thornwood, NY). PMTs, laser power and pinhole aperture were set to minimize bleeding of signal from one dye channel to the other. Images for both the dyes (i.e., calcein and propidium iodide) were taken sequentially to avoid signal overlap. Cells were observed at 20x and 60x magnification to visually inspect cellular uptake in viable cells.

A bench-top flow cytometer (BD LSRII, BD Biosciences, San Jose, CA) was used to quantify uptake, i.e. the number of live cells with calcein uptake, and viability, i.e. the number of live cells that were not necrotic or fragmented, on a cell by cell basis. For quantifying necrotic death, propidium iodide stain was analyzed using a PerCP-Cy5, 670 nm longpass filter. Calcein uptake into cells was detected using a FITC, 530/28 nm bandpass filter. A cell gate was constructed based on forward-scattered and side-scattered light to determine the size distribution of cells in the control. Any events lying within this gate were considered to be cells, whereas events smaller than that were considered cells fragments. To

determine the concentration of intact cells (and thereby account for possible cell loss due to fragmentation), we multiplied the volumetric flow rate in the flow cytometer by the time of analysis to determine the total volume analyzed. Dividing the number of cells detected within the gate by the volume provided the cell concentration, which could be compared to non-exposed controls to determine cell loss due to fragmentation. Approximately 10^5 cell events were collected per sample which was approximately 20% of the total cells present in each sample. To account for spectral overlap between the dyes, compensation controls were run for each experiment. Propidium iodide-positive samples were made by incubating cells in 70% methanol for 30 min and then washing with PBS. Calcein-positive samples were made by exposing cells with CB nanoparticles and calcein at 44 mJ/cm^2 per shot for 3 min. At this condition, there was extensive cell death, but almost all cells which remained viable had calcein uptake.

3.2.7 Statistical Analysis

A minimum of three replicates was performed for all conditions. Replicates enabled calculations of means and standard deviation. The equality of mean response (uptake or viability) between treated samples and sham exposures and other control samples was tested using ANOVA ($\alpha = 0.05$). To test equality of mean response between pairs of data points, 1-way ANOVA followed by the post hoc Tukeys pairwise comparison was used, whereas 2-way ANOVA was employed to compare three or more data points using Microsoft Excel 2010 (Microsoft, Redmond, WA) and GraphPad Prism 6 (GraphPad Software, La Jolla, CA). The null hypothesis was that the average fraction of cells with uptake (or average fraction of viable cells) between a treated sample and a sham exposure were equal. To compare between mean values of two data points, an unpaired Students t-test is performed (2 tails) assuming unequal variances.

3.3 Results

3.3.1 Intracellular uptake due to laser-activation of CB nanoparticles

We first validated that exposure of cells to infrared laser pulses in the presence of CB nanoparticles resulted in uptake of a marker compound, calcein, by viable cells. As shown

in Fig. 3.1a, DU145 prostate cancer cells incubated with CB nanoparticles and calcein, but without exposure to laser pulses, did not show significant intracellular uptake of calcein. This treatment is referred to here as a sham exposure, where cell samples received the same treatment as laser-exposed samples, except the laser was not activated. In Fig. 3.1b, cells were exposed to laser pulses, but there were no CB nanoparticles present. Again, insignificant uptake was seen.

In contrast, Fig. 3.1c shows the effects of pulsing with a laser in the presence of CB nanoparticles, where the majority of cells appear green, indicating intracellular uptake of green-fluorescent calcein. Finally, Fig. 3.1d shows a magnified view of cells exposed to laser pulses and CB nanoparticles, further indicating that the calcein is located throughout the interior of the cells rather than, for example, being sequestered in endosomal vesicles.

3.3.2 Effects of laser pulse fluence, number of pulses, beam spot size and pulse repetition rate on intracellular uptake and cell viability

We next quantified intracellular uptake of calcein and viability in DU145 cells as a function of laser fluence, while keeping all other exposure parameters constant (Fig. 3.2). The time of exposure was set to 1 min at 10 Hz pulsing frequency. Laser exposure at the lowest fluence studied (12.5 mJ/cm^2 per pulse) caused no significant uptake or viability loss compared to the sham negative control (Fig. 3.2). As laser fluence increased, intracellular uptake increased as well, climbing from 30% of cells with uptake at a fluence of 18.75 mJ/cm^2 to 76% of cells with uptake at a fluence of 44 mJ/cm^2 (ANOVA, $p < 0.0001$). Above 44 mJ/cm^2 , intracellular uptake no longer increased and maintained a value of approximately 70–80% of the cells (ANOVA, $p = 0.98$) with uptake. Over the full range of laser fluence conditions studied, the viability remained insignificantly different from sham control samples in almost all cases (ANOVA, $p = 0.48$) (Fig. 3.2).

We expect that laser exposure time (i.e., number of laser pulses) would also affect intracellular uptake and viability. Fig 3.3a and 3.3b demonstrates the effect of exposure time on the uptake and viability of DU145 cells, while keeping all the other factors constant. In Fig. 3.3a, the fluence was set to 18.75 mJ/cm^2 . The viability did not change significantly compared to sham exposure when the exposure time was increased from 1 min to 7 min

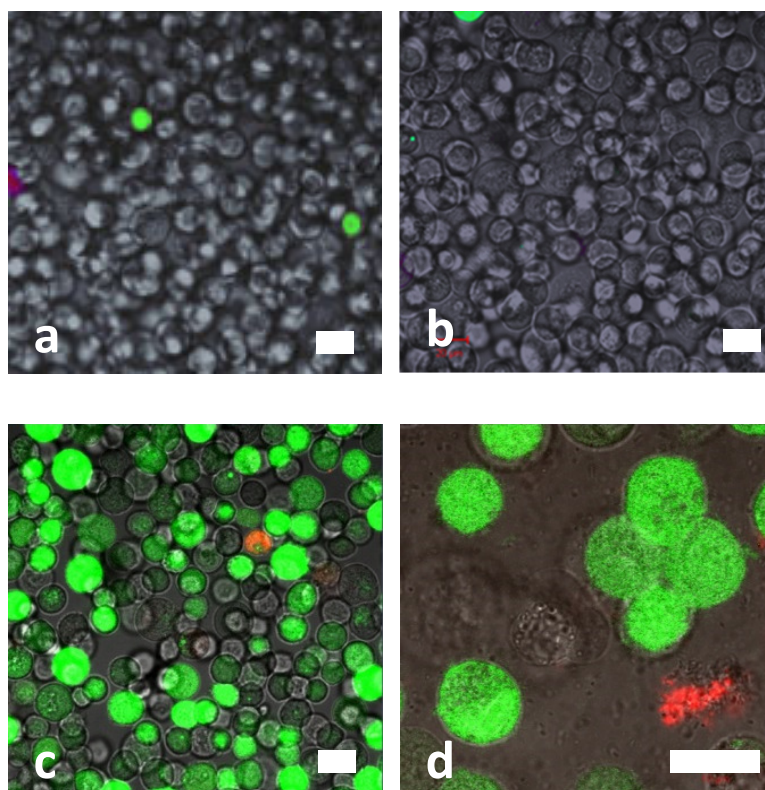


Figure 3.1: Fluorescence imaging of intra-cellular uptake. Cells inspected visually using a confocal microscope show that there is little uptake of calcein (green) when cells were exposed to just carbon black (CB) nanoparticles but no laser (a), very little uptake when cells were exposed to laser but not CB nanoparticles (b) and extensive uptake when cells were exposed to laser with CB nanoparticles at 44 mJ/cm^2 fluence, 1 min exposure time, 10 Hz pulsing frequency and 21.4 mm beam diameter (c). Closer inspection of these cells at higher magnification, reveals that calcein is present throughout the interior of the cells and not just localized, for example, to endosomes (d). In all samples, very few cells were stained with propidium iodide (red), which is a marker of necrotic and late apoptotic deaths. Scale bars are $20 \mu\text{m}$.

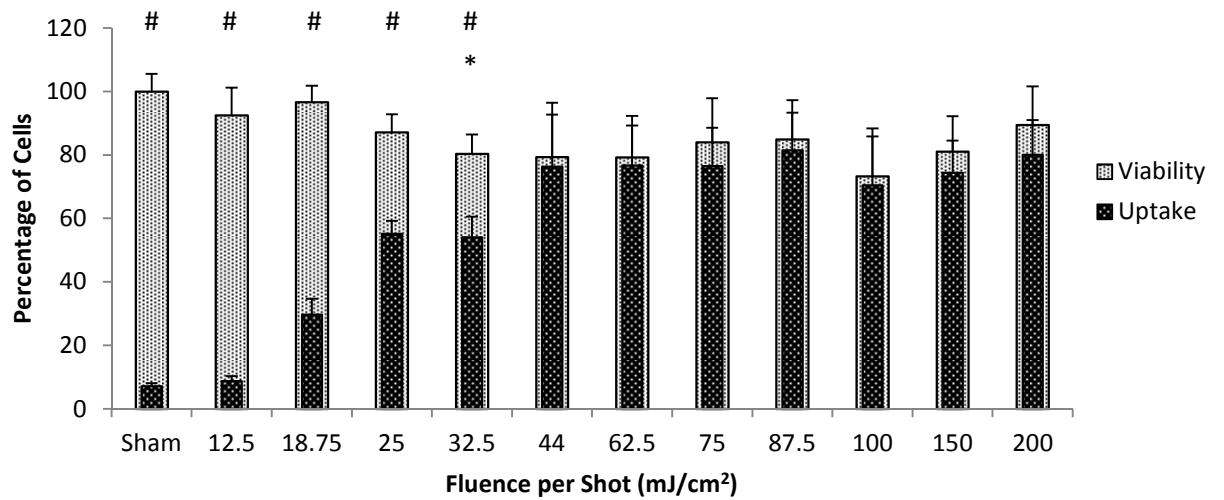


Figure 3.2: Effect of laser fluence on intra-cellular uptake and viability of DU145 cells. Cells were exposed to laser for 1 min at various laser fluence levels. Asterisk (*) shows data where viability is lower than sham and hash symbol (#) shows data where uptake is lower than viability ($p < 0.05$). The figure demonstrates saturation of both uptake and viability beyond 44 mJ/cm² exposure. All laser exposures were at 10 Hz pulsing frequency and 21.4 mm beam diameter. Data show average \pm standard deviation (SD) ($n = 3$ replicates).

(ANOVA, $p = 0.97$), whereas the uptake increased from 30% to 88% (ANOVA, $p < 0.0001$). At 7 min, the uptake value was statistically not different from the viability value (Students t-test, $p = 0.36$), indicating that essentially all viable cells had uptake. When the laser fluence was increased to 25 mJ/cm^2 (Fig. 3.3b), there was a decrease in viability as exposure time increased (ANOVA, $p = 0.0014$), and the uptake initially went up and then decreased (ANOVA, $p < 0.0001$). At all times, uptake was significantly less than viability values (Students t-test, $p < 0.05$).

The data on intracellular uptake from Figs. 2a, 3a and 3b are replotted in Fig. 3.3c as a function of total energy input (i.e., pulse fluence \times laser beam exposure area \times number of pulses). This analysis shows that uptake was proportional to the total energy input below approximately 100 J, which then saturated at a constant uptake value at higher energy inputs.

The data presented so far were generated using a laser beam that fully covered the sample cuvette. When the spot size diameter of the laser beam was reduced from 21.4 mm (full exposure of the cuvette) to 9 mm (16% of the cuvette area was exposed), it resulted in reduced bioeffects. Fig. 3.4a shows that under full cuvette exposure, uptake was higher (Student t-test, $p = 0.002$), but the viability was lower (Student t-test, $p = 0.01$) compared to the partially exposed samples. The total percentage of cells affected by the laser (either uptake or death) was 87% in the case of full cuvette exposure and it was just 40% in the case of 9 mm beam diameter exposure. This value is greater than the 16% of cuvette area, suggesting convection within the cuvette led to more cells entering the laser beam during the exposure time. Additional studies showed that the location of the beam spot in the cuvette did not matter as long as it was within the cuvette area filled with cell solution (data not shown).

The pulsing frequency in the data generated so far was 10 Hz (i.e., 10 pulses per second). We therefore also studied slower pulsing frequencies to determine the resulting effect on uptake and viability. Decreasing the pulsing frequency separates each pulse by more time, which means that the cells have more time to recover from the effect of the laser-CB interaction between pulses. In Fig. 3.4b, pulsing frequency was varied between 0.1 Hz to

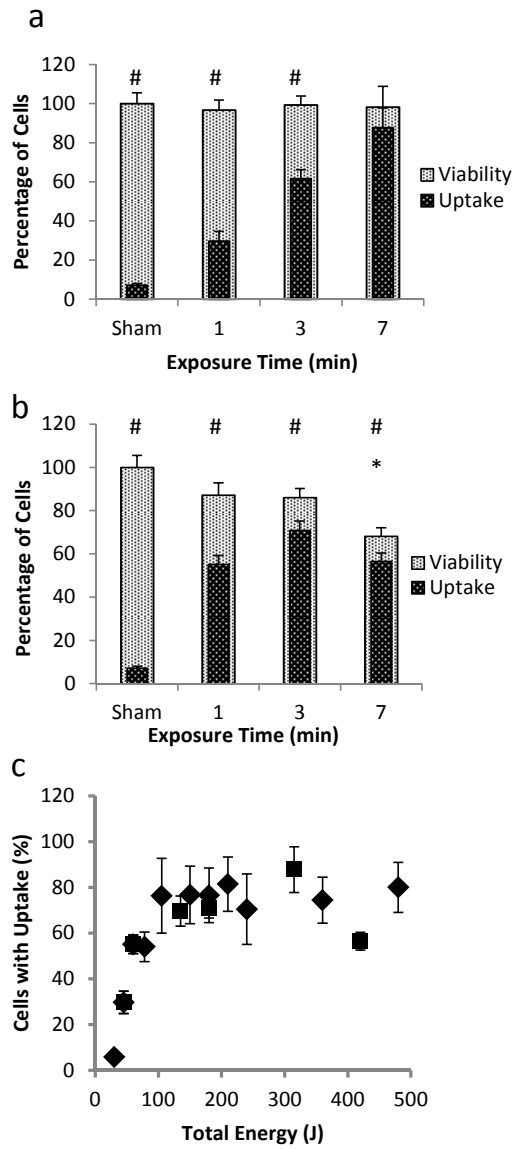


Figure 3.3: Effect of exposure time and total energy on intracellular uptake and viability of DU145 cells. (a) When fluence was set at 18.75 mJ/cm^2 , there was no change of viability but uptake increased with exposure time until it was the same as viability at 7 min. (b) When fluence was set at 25 mJ/cm^2 , viability was less than the sham and uptake was always significantly lower than viability ($p < 0.05$). (c) When total energy is plotted against uptake, at $\geq 100 \text{ J}$, uptake remained approximately constant at $\sim 75\%$ at higher energy levels. All laser exposures were at 10 Hz pulsing frequency and 21.4 mm beam diameter. Asterisk (*) shows data where viability is lower than sham and hash symbol (#) shows data where uptake is lower than viability. Data show average \pm SD ($n = 3$).

10 Hz, keeping all the other parameters constant. The viability was unaffected by changing pulsing frequency (ANOVA, $p = 0.35$). The uptake value for 0.1 Hz was a little higher than the rest (ANOVA, $p = 0.025$). This indicates that greater spacing between pulses by decreasing pulsing frequency has little effect on uptake and viability, which further suggests that any recovery by cells after being exposed to a laser pulse and CB interaction processes occurs on a timescale faster than 100 ms (corresponding to 10 Hz pulsing) or possibly slower than 10 s (corresponding to 0.1 Hz pulsing).

3.3.3 Effects of interaction between sequential pulsing protocols on uptake and viability

Our guiding hypothesis is that acoustic energy emitted by CB nanoparticles during laser exposure impacts cells to transiently increase plasma membrane permeability. According to this hypothesis, pre-treatment of CB nanoparticles in the absence of cells should have no effect on cells added after the laser exposure. To test this hypothesis, we first exposed cells at a mild laser condition (Fig. 3.5a, condition B) and found that there was no significant change in viability or uptake compared to the sham control (Fig. 3.5a, condition A). In a second experiment, we exposed CB nanoparticles (without cells) to a strong laser condition and then added cells to this solution within 5 s after laser exposure. The resulting solution was then exposed to laser condition B. This effect of CB nanoparticle laser pre-treatment (Fig. 3.5a, condition C) had no effect on uptake or viability when compared with condition B (Students t-test $p = 0.26$). This suggests that cells must be present during laser activation of the CB nanoparticles, because the effects of the activation do not persist after laser exposure.

We next performed an experiment to see if pre-conditioning cells would have an effect on subsequent laser exposure. We first exposed cells to a mild laser condition, like before, which had no significant effect on viability and minimal effect on uptake (Fig. 3.5b, condition B, Students t-test $p = 0.26$ for viability and $p = 0.003$ for uptake) and subsequently exposed cells to a moderate laser condition, which significantly increased uptake and decreased viability (Fig. 3.5b, condition D, Students t-test $p = 0.041$ for viability and $p < 0.001$ for uptake). We then combined these two exposures by first exposing cells to the moderate

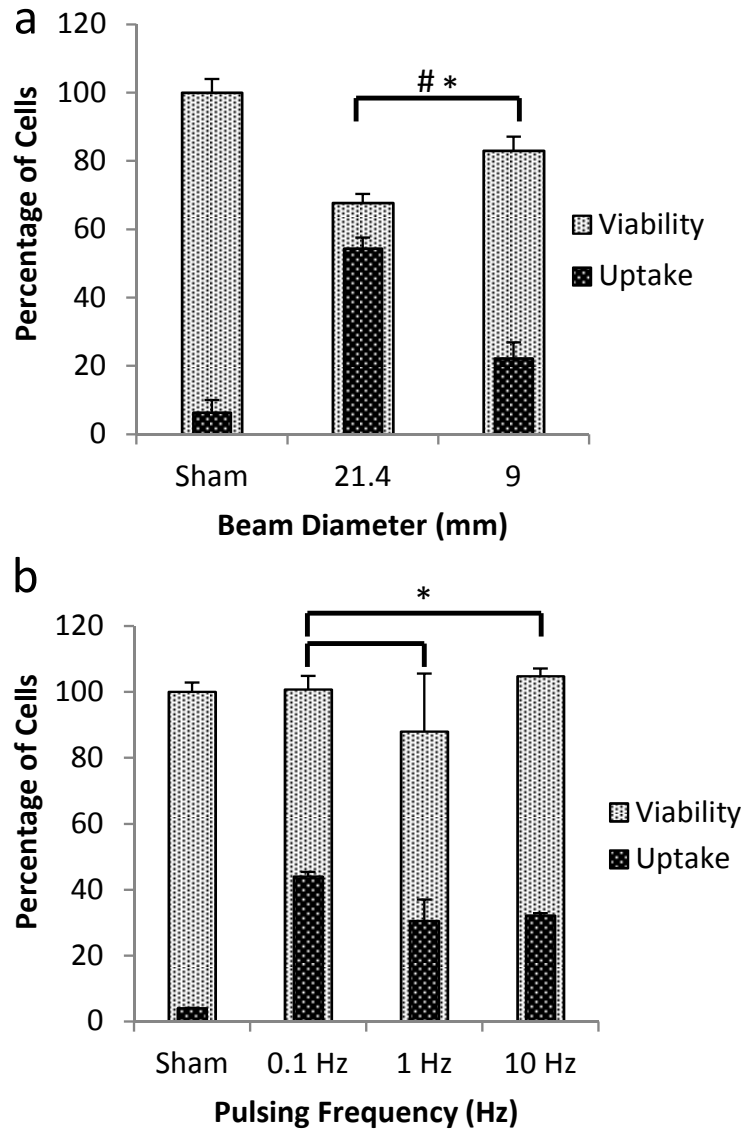


Figure 3.4: Effect of beam diameter and pulsing frequency on intracellular uptake and viability of DU145 cells. (a) Reducing the beam diameter from 21.4 mm (full cuvette) to 9 mm (16% of the cuvette surface area) resulted in lesser bioeffects, with higher viability and lower uptake (44 mJ/cm² fluence, 1 min exposure time, 10 Hz pulsing frequency). (b) Increasing pulsing frequency from 0.1 Hz to 10 Hz while keeping number of pulses at 100 had no statistically significant effect on viability, while uptake was slightly higher at 0.1 Hz compared to 1 Hz and 10 Hz (44 mJ/cm² fluence, 21.4 mm beam diameter). Asterisk (*) and hash symbol (#) show statistically significant differences in uptake and viability, respectively (p < 0.05). Data show average ± SD (n = 3).

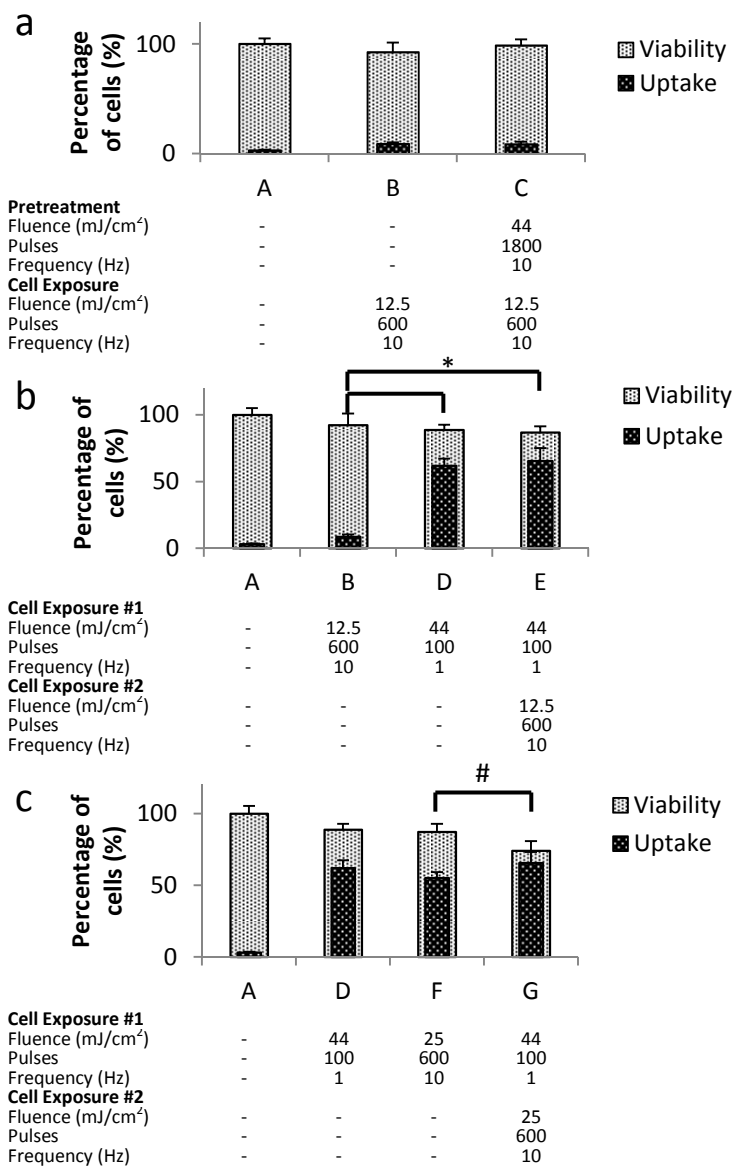


Figure 3.5: Effect of pretreatment and sequential laser exposures on intracellular uptake and viability of DU145 cells. (a) Compared to sham treatment (A), there was no significant effect of weak laser exposure of cells in the presence of CB nanoparticles (B). Very strong laser exposure of CB nanoparticles (without cells) as a pretreatment followed by addition of cells and weak laser exposure (C) was not significantly different from conditions (B) and (A) in terms of uptake and viability. (b) The sequential combination of a strong laser exposure and weak laser exposure (E) was statistically no different from the strong laser exposure alone (D) and much greater than the weak laser exposure alone (B) in terms of uptake and viability. (c) The sequential combination of two strong laser exposures with different laser parameters (G) had lower viability but uptake was not statistically different from either of the individual laser exposures alone (D, F). All laser exposures were at 10 Hz pulsing frequency and 21.4 mm beam diameter. Asterisk (*) and hash symbol (#) show statistically significant differences in uptake and viability, respectively ($p < 0.05$). Data show average \pm SD ($n = 3$).

laser condition (thereby preconditioning them) and then exposing the cells to the mild laser condition (Fig. 3.5b, condition E). However, there was no significant difference between conditions D and E (Students t-test $p = 0.61$ and $p = 0.6$ for viability and uptake respectively), indicating that pre-conditioning cells with a moderate exposure did not enhance the effects of a mild exposure. While we examined only one of many possible preconditioning scenarios, the data suggest that the effects of an initial exposure with significant bioeffects do not make cells more susceptible to bioeffects from a subsequent sub-threshold exposure. This is consistent with the observation made previously when testing the effects of pulsing frequency (Fig. 3.4b), which indicated that cells do not appear to have a memory of previous exposures if the exposures are spaced by >100 ms.

Another combination of laser CB interaction was examined employing moderate laser conditions. One exposure involved stronger fluence and shorter exposure time, while the other exposure involved weaker fluence and longer exposure time. We found that each condition by itself increased uptake and decreased viability (Fig. 3.5c, conditions D and F, Students t-test $p = 0.044$ and $p < 0.001$ for viability and uptake, respectively, for condition F). The combination of applying condition D followed by condition F within 5 s led to a significant decrease in viability (Students t-test $p = 0.03$) with no significant change in uptake (Students t-test $p = 0.53$) (Fig. 3.5c, condition G). The viability in condition G (i.e., 74%) was roughly the product of the viability in conditions D and F ($88\% \times 87\% = 76\%$), suggesting an additive, rather than a synergistic effect of this combination. The fact that uptake did not increase further could be explained because the level of uptake was statistically indistinguishable from the level of viability (Students t-test $p = 0.23$), meaning that essentially all viable cells had uptake.

3.3.4 Effects of CB nanoparticle type and concentration on uptake and viability

The proposed mechanism of molecular uptake into cells in this study involves laser energy absorption and transduction by carbon nanoparticles creating photo-acoustic effects. Fig. 3.6 shows a comparison between India ink, another form of CB nanoparticle, and CB nanoparticles used so far in this study at various concentrations under the same laser

conditions. India ink includes CB nanoparticles as the main component along with other components whose composition are insufficiently characterized [155, 156]. We determined by dynamic light scattering, that the mean diameter of particles in India ink was 110 nm (dispersity of 0.23), as compared to 189 nm (dispersity of 0.16) for the CB nanoparticle aggregates. At each condition in the laser exposure experiments, the concentration of India ink particles was adjusted to have the same laser absorption as their CB nanoparticle counterparts.

Considering the effect of nanoparticle concentration first, when CB nanoparticle concentration was increased, keeping all other factors constant, the viability decreased (ANOVA, $p < 0.0001$), which resulted in a decrease of uptake as well (ANOVA, $p < 0.0001$). Under all the exposed conditions, the difference between uptake and viability was statistically non-significant (Students t-test, $p > 0.05$). When CB nanoparticles were replaced with India ink particles, there was similarly a decrease in viability (ANOVA, $p < 0.0001$), which again resulted in a decrease in uptake (ANOVA, $p < 0.0001$).

When the effects of the India ink and CB nanoparticles are compared, there is no significant difference at low particle concentrations (Students t-test, $p > 0.05$), but viability and uptake are both lower in the India ink samples at the highest concentration (Students t-test, $p < 0.05$). Altogether, these results suggest that the specific chemistry of the CB formulation is not as important as the concentration of CB nanoparticles.

3.3.5 Toxicity of CB nanoparticles

To assess possible toxic effects of the CB nanoparticles, an MTT assay was performed on DU145 cells after exposure to CB nanoparticles at various concentrations for 24 h and 72 h. MTT stains cells that are properly respiring, such that lack of staining is an indicator of cytotoxicity. Fig. 3.7 shows the absorbance values as a function of increasing CB nanoparticle concentration. The data were normalized with respect to the CB nanoparticle-free control. There was no significant difference between the absorbance values of the MTT assay at 24 h and 72 h (ANOVA, $p = 0.39$). Moreover, there was no significant loss of viability below 200 mg/l (ANOVA, $p = 0.997$ and $p = 0.996$, respectively).

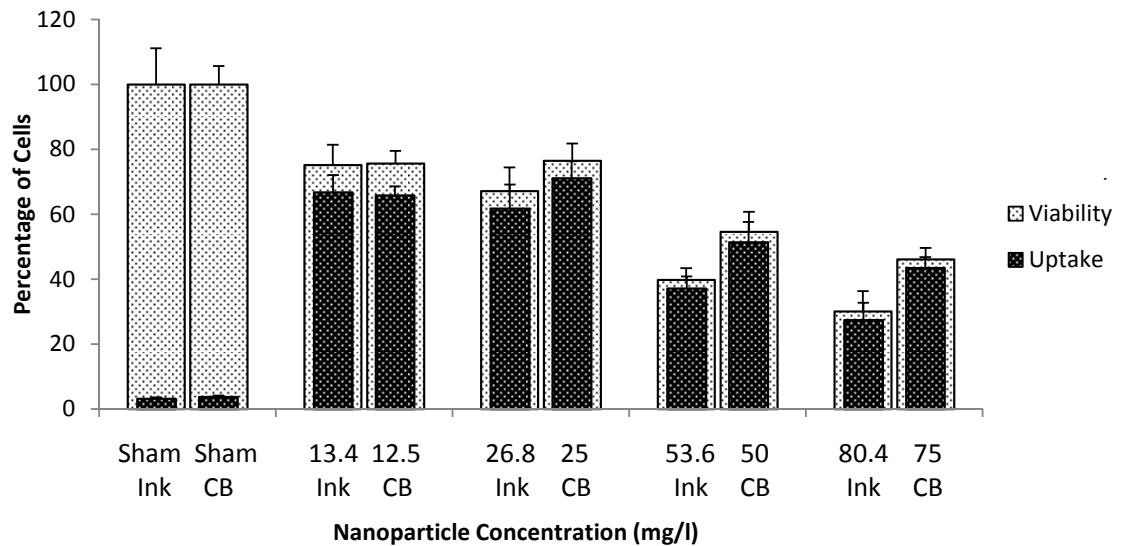


Figure 3.6: Effect of increasing India ink and CB nanoparticle concentration on intracellular uptake and viability of DU145 cells. In each paired comparison, the concentration of India ink and CB nanoparticles were adjusted so that the laser absorbance was the same. Uptake and viability generally decreased with increasing nanoparticle concentration, and India ink had stronger effects on uptake and viability than CB nanoparticles at the higher concentrations. All laser exposures were at 44 mJ/cm² fluence, 1 min exposure time, 10 Hz pulsing frequency and 21.4 mm beam diameter. Asterisk (*) and hash symbol (#) show statistically significant differences in uptake and viability, respectively (p < 0.05). Data show average ± SD (n = 3).

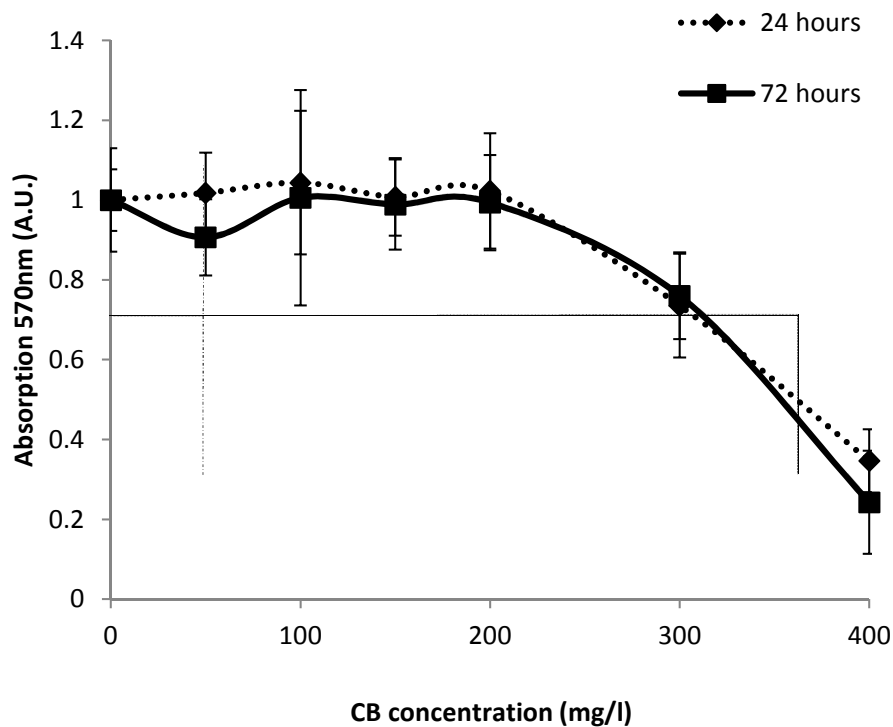


Figure 3.7: Toxicity of CB nanoparticles on DU 145 cells measured by MTT cytotoxicity assay. Cells were exposed to CB nanoparticles for 24 h and 72 h, which yielded ED50 values of 350 mg/l and 360 mg/l, respectively. These values are ~14 times higher than the concentration (25 mg/l) used in most experiments in this study. Data show average \pm SD (n = 3).

These data produce ED50 values of 360 mg/l for the 24 h data and 350 mg/l for the 72 hr data. For most experiments in this study, a CB nanoparticle concentration of 25 mg/l was used, which is an order of magnitude lower than the ED50 value. Visual inspection of cells incubated with high-concentration CB nanoparticles showed the particles coating the cell surface (data not shown). This steric interaction, rather than a chemical interaction, might have affected cell viability at the higher concentrations. The analysis indicates that at the concentrations used in this study, there was no significant change to cell viability as a result of extended exposure to CB nanoparticles.

3.3.6 Effects of cell type and molecular weight of uptake marker on uptake and viability

In addition to DU145 prostate cancer cells, we also studied the effects of laser-activated CB nanoparticles on H9c2 rat cardiomyoblasts. The experiments with these cells were performed at exposures of 25 mJ/cm² for 1 and 3 min, keeping all other parameters constant (Fig. 3.9). When the performance of the two cell lines was compared, the viability was statistically not different from each other (ANOVA, $p = 0.94$), but the uptake was lower for H9c2 cells (ANOVA, $p = 0.007$). These data show that the effects of laser-activated CB nanoparticles on cell uptake and viability are seen in multiple cell types.

The delivery efficiency was also characterized by varying the molecular weight of the uptake markers. Calcein was replaced with FITC-labeled dextrans of molecular weights 10 kDa, 70 kDa and 500 kDa and exposed to laser at 44 mJ/cm² for 1 min, keeping all other parameters constant. There was no statistical difference between the viability of the exposed samples (ANOVA, $p = 0.92$), whereas uptake decreased with increasing molecular weight (ANOVA, $p = 0.022$).

3.3.7 Trade-off between maximizing uptake and maximizing viability

When mean values of cell viability are plotted against uptake (Fig. 3.10), all data points fall below the viability = uptake line. This is because, being counted as an uptake cell requires that the cell must be viable. Some points were at or just below the viability = uptake line, indicating that essentially all viable cells had uptake. No points were at 100% viability and

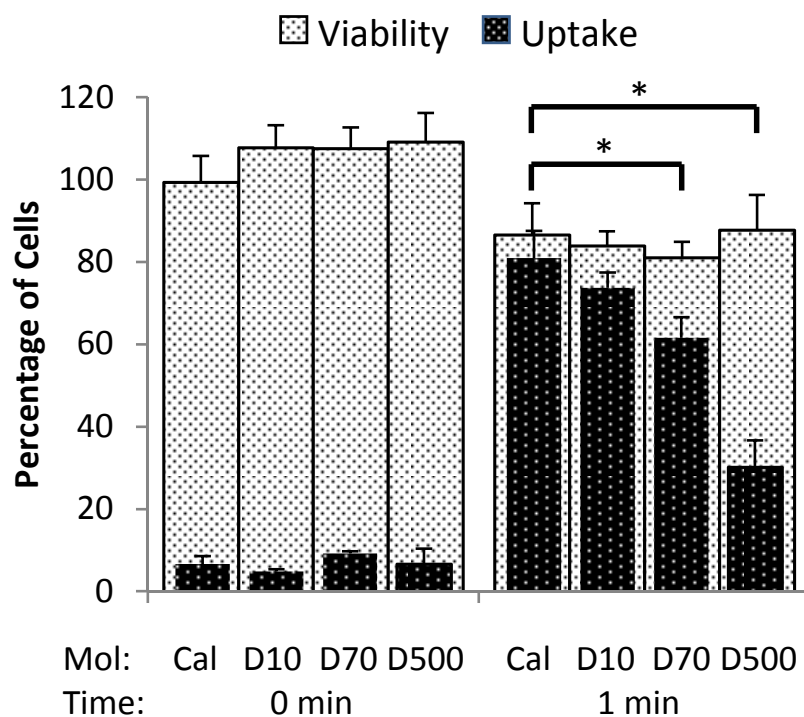


Figure 3.8: Comparison of intracellular uptake and viability of two cell lines (DU145 and H9c2) after the same laser exposures. Cell viability was the same, whereas uptake after the 1 min exposure was significantly different between the two cell lines. All laser exposures were at 25 mJ/cm² fluence, 10 Hz pulsing frequency and 21.4 mm beam diameter. Asterisk (*) shows statistically significant difference in uptake (p < 0.05). Data show average ± SD (n = 3).

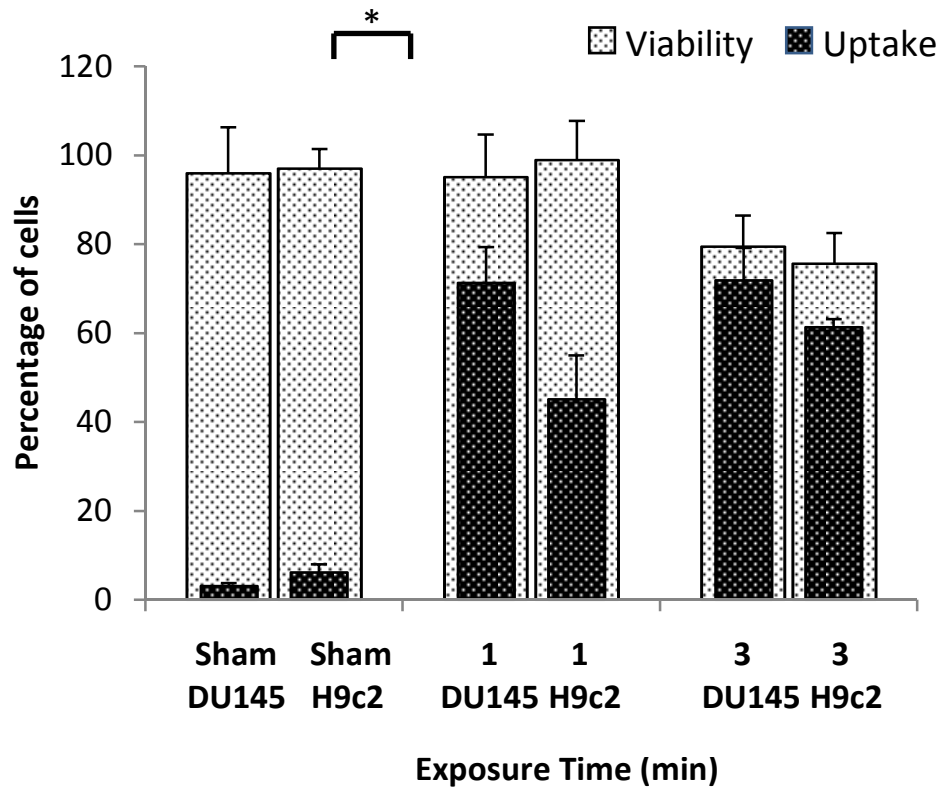


Figure 3.9: Effect of molecular weight on intracellular uptake and viability after the same laser exposures. There is no statistical difference in viability across all samples, whereas the uptake decreased as the molecular weight was increased for calcein (Cal), 10 kDa dextran (D10), 70 kDa dextran (D70) and 500 kDa dextran (D500). All laser exposures were at 44 mJ/cm², 10 Hz and 21.4 mm beam diameter. Asterisk (*) shows statistically significant difference in uptake ($p < 0.05$). Data shows average \pm SD ($n = 3$).

100% uptake, although we did observe 88% uptake with close to 100% viability.

3.4 Discussion

This study was guided by the hypothesis that laser energy is absorbed by CB nanoparticles, which transduce that energy into a form that transiently permeabilizes cells, resulting in intracellular uptake and possible loss of cell viability. Based on prior literature [5, 152, 157], we further believe that the mechanism of energy transduction involves laser-CB nanoparticle interactions leading to the sudden heating of the nanoparticles, which leads to generation of acoustic emissions (i.e., pressure waves) caused by thermal expansion of the nanoparticles, as well as possibly the vaporization of water and/or chemical reaction between water and carbon (i.e., $C (s) + H_2O (l) \rightarrow CO (g) + H_2 (g)$). Elucidating the details of this energy transduction mechanism is beyond the scope of this study.

There should be two time scales associated with this process. The first time scale is that of laser absorption by CB nanoparticles followed by pressure wave generation. The second time scale is that of cell membrane permeabilization, intracellular uptake and membrane resealing. We expect that the time scale of the first step is at least nanoseconds (i.e., the time scale of the laser pulse), but may be longer, given the time it may take to grow and collapse gas bubbles, if they are involved in the mechanism [158]. The time scale associated with intracellular uptake through permeabilized membranes is likely much longer, given that it involves transmembrane diffusion and cell membrane resealing mechanisms.

In general, we would expect that more energy transduction from laser irradiation to acoustic emissions should increase bioeffects on cells. Thus, increased energy transduction should be associated with both increased intracellular uptake as well as increased loss of cell viability. Because of this, the goal for applications is to find conditions that optimize uptake without significant loss of viability. The present study showed that increasing fluence and number of laser pulses (i.e., time of irradiation), both increased energy input and, therefore, increased energy output to cells. Increasing CB nanoparticle concentration increased the number of acoustic sources and thereby increased energy output to cells without increasing energy input. Consistent with our hypothesis, increasing each of these three parameters led

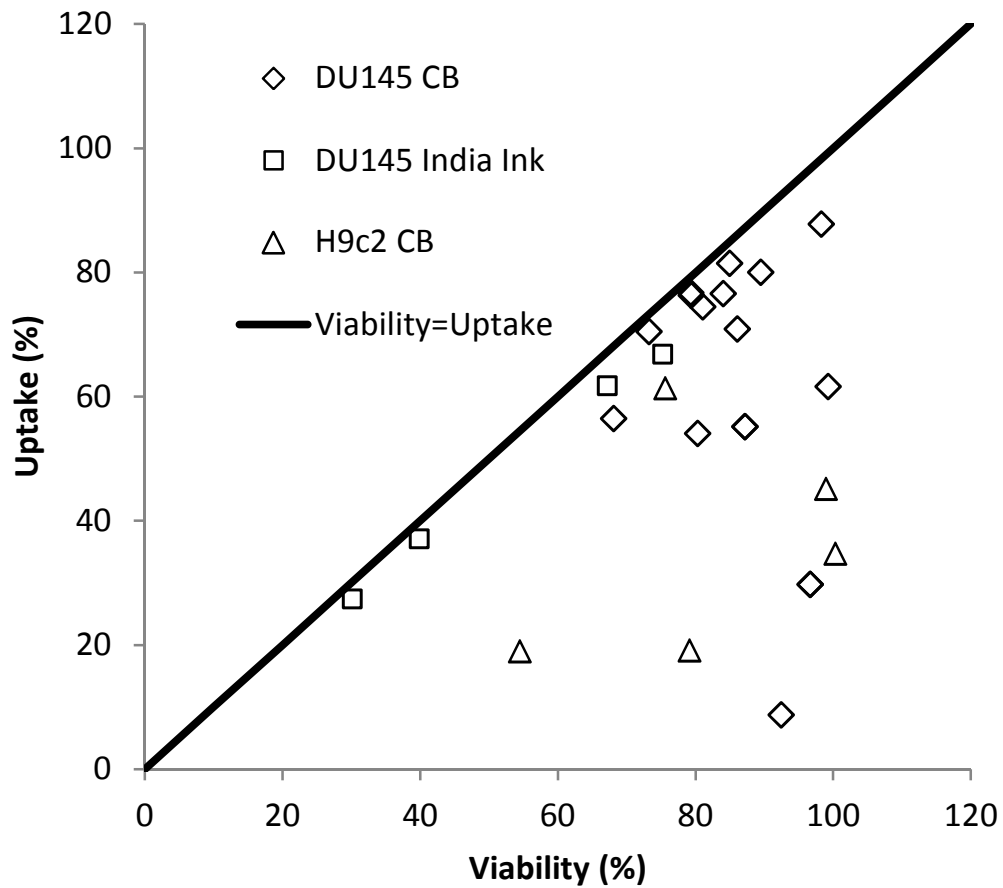


Figure 3.10: Comparison between intracellular uptake and viability. This graph shows all data generated in this study (i.e., from Figures 2 - 7). All data points are at or below the uptake = viability line since there cannot be more cells with uptake than cells that are viable.

to increased uptake and loss of viability, depending on the details of the exposure conditions. The optimal conditions found in this study involved, 18.75 mJ/cm² laser fluence, 7 min exposure of DU145 cells with 25 mg/l CB nanoparticle concentration, and thereby achieving an intracellular delivery efficiency of 88% with 98% viability (Fig. 3.3a). There was no significant effect on uptake or viability due to laser exposure alone (Fig. 3.1a), incubation with CB nanoparticles alone (sham experiments), or pre-treatment of CB nanoparticles with a strong laser exposure (Fig. 3.5a), which is also consistent with the mechanism involving laser energy transduction by CB nanoparticles. Increasing laser fluence initially increased uptake, but then the effects of increasing fluence saturated, which produced cells with efficient uptake and little loss of viability (Fig. 3.2). In contrast, increasing the duration of the laser exposure increased uptake until the point where it started killing cells (Fig. 3.3b). This suggests that the effect of increasing the force applied to cells saturates whereas increasing the time over which that force acts on the cells does not. This interesting relationship is similar to previous observations in electroporation-mediated uptake, where the effects of increasing voltage resulted in saturated uptake, but the effects of increasing number or length of electrical pulses did not [159].

At the conditions used in this study, increasing the concentration of CB nanoparticles increased bioeffects in the form of killing more cells. We did not see an increase in uptake, because at the lower CB nanoparticle concentration used, almost all viable cells already had uptake. Thus, we saw a decrease in uptake due to cell death. At the lowest CB nanoparticle concentration studied (12.5 mg/l), the nanoparticle-to-cell ratio was approximately 100:1 whereas at the highest concentration (75 mg/l) it was approximately 600:1. In general, more acoustic emission sites should produce more pressure waves impacting cells. However, the details of this interpretation are complicated by constructive and destructive interference of waves in the complex acoustic field. Uptake and viability did not depend strongly on pulsing frequency of the laser (Fig. 3.4b). This suggests either that each pulse creates independent effects on the cells, which would mean that the time scale for onset and reversal of the direct bioeffects of the laser exposure is shorter than 100 ms (corresponding to pulsing at a frequency of 10 Hz) or possibly that the time scale is much longer than 10 s (corresponding

to pulsing at a frequency of 0.1 Hz), such that interacting effects of each pulse on the next one(s) are not affected by changing their separation from 0.1 s to 10 s. Given the nanosecond time scale of the laser exposure itself, we hypothesize that the first scenario above is the more likely scenario, such that intracellular uptake and bioeffects that initiate loss of viability occur on a time scale shorter than 100 ms. Our interpretation is further supported by the data in Fig. 3.5b, which showed that pre-treatment of cells with a moderate laser condition did not make them more susceptible to subsequent exposure to mild laser conditions a few seconds later.

When CB nanoparticles were replaced by India ink at concentrations which had the same laser absorbance, the India ink particles were yielded lower viability (Fig. 3.6), which suggests a stronger mechanical effect on the cells. This may be because the nanoparticles in India ink are smaller than CB nanoparticles, which means that for the same mass of carbon, there was a larger number of India ink nanoparticles than CB nanoparticles. An alternative explanation could be that the poorly characterized additional component particles found in India ink might have effects on cells during laser exposure.

Molecules ranging from 0.6 kDa to 500 kDa were delivered into cells, but with decreased efficiency at higher molecular weight. This could be explained by a pore size distribution created in the cell membrane similar in size to that of the molecules, such that the larger molecules were excluded, or at least hindered, by a fraction of the pores. The smallest dextran (10 kDa) has a radius of approximately 2.7 nm and the largest dextran (500 kDa) has a radius of approximately 15 nm [160], which suggests pores of similar size. Alternatively, decreased uptake of the larger molecules could be explained by their slower diffusion through short-lived membrane pores. According to the Stokes-Einstein equation, the 500 kDa dextran has a diffusivity 5.5 times smaller than the 10 kDa dextran.

Finally, we can consider future possible applications for targeted intracellular drug delivery guided by this study's findings. Flow cytometry analysis and MTT cytotoxicity analysis suggested that the procedure was well tolerated by cells under the conditions of this study. Similar bioeffects were seen in two cell lines, DU145 human prostate carcinoma cells and H9c2 rat cardiomyocytes, suggesting the generality of the approach to multiple cell types.

Uptake was also seen for molecules as big as 500 kDa dextran, although the uptake was significantly reduced at higher molecular weight. Bioeffects were reduced by reducing the beam diameter, which was interpreted to mean that bioeffects were only felt where the laser was focused. This can enable targeting the effects to certain locations.

Altogether, these capabilities suggest an efficient method to load cells with molecules at high cell viability, which can be used for in vitro laboratory applications for research or, in the future after additional development, for in vivo drug delivery applications in medicine. Some of the advantages of this approach are its relatively simple procedure, the rapid timescale of delivery into cells and the localization of effects at the site of laser focus. A concern is how the nanoparticles of sizes close to 200 nm will be cleared from the tissue after the laser exposure. This approach is mechanistically similar to electroporation and sonoporation, both of which are used clinically [161, 162], but differs in its ability to achieved highly efficient intracellular delivery with high viability using a non-invasive method.

3.5 Conclusion

This study examined the use of nanosecond laser pulses in the presence of CB nanoparticles to increase intracellular delivery of model compounds, calcein and dextrans, while maintaining high cell viability. We believe that CB nanoparticles absorb the laser energy and transduce it into acoustic outputs that transiently permeabilize the cell membranes, although the details of this mechanism are not explored in this study. We found that lower fluence, with lower concentration of CB nanoparticles and longer exposure times resulted in a gentler photo-acoustic environment that allowed uptake of molecules in up to 88% of cells with no significant loss of cell viability. Increased fluence or CB nanoparticle concentration were also able to yield high uptake but generally had more cell death. We conclude that the method investigated in this work uses a straightforward protocol to enable efficient intracellular delivery of molecules with high cell viability using nanosecond-pulse laser-activated carbon nanoparticles for laboratory use and possible future in-vivo applications

CHAPTER IV

POLOXAMER SURFACTANT PRESERVES CELL VIABILITY DURING PHOTOACOUSTIC DELIVERY OF MOLECULES INTO CELLS

Efficient intracellular delivery of molecules is needed to modulate cellular behavior for laboratory and medical applications, but is often limited by trade-offs between achieving high intracellular delivery and maintaining high cell viability. Here, we studied photoacoustic delivery of molecules into cells by exposing DU145 human prostate carcinoma cells to nanosecond laser pulses in the presence of carbon black nanoparticles. Under strong laser exposure conditions, less than 30% of cells were viable and exhibited uptake. Addition of poloxamer surfactant at those laser exposure conditions increased cell viability to almost 90%, with intracellular uptake in >80% of cells. This remarkable increase in efficiency of intracellular delivery and cell viability may be attributed to enhanced cell membrane re-sealing by poloxamer surfactant after photoacoustic delivery. While F-68 poloxamer was effective, the larger, more-hydrophobic F-127 poloxamer provided the best results. There was no significant protective effect from addition of Ca^{2+} , BAPTA-AM, ATP, fetal bovine serum or glycine betaine, which were expected to promote active cell membrane repair mechanisms and other active intracellular protective processes. We conclude that poloxamer surfactant preserves cell viability during photoacoustic delivery of molecules into cells, thereby enabling highly efficient intracellular delivery.

4.1 Introduction

With advances in medicine and pharmaceutical technologies, patient treatment options are often limited not by the availability of an efficacious drug, but by the ability to deliver the drug to its therapeutic target [2, 8, 163]. The ultimate target of many therapeutics is inside cells, where the drug can alter cellular biochemistry and gene regulation [1, 164]; however, the cells plasma membrane regulates movement of molecules into cells and presents

a difficult barrier to uptake of many therapeutics. Intracellular drug delivery is of recent interest due to an increasing number of intracellular targets that have potential applications, for example, in cancer and AIDS [165, 166]. Techniques that deliver drugs intracellularly can be broadly classified into three categories; viral, non-viral biochemical and non-viral physical methods [3]. While each method has advantages and disadvantages, physical methods, like electroporation and sonoporation, are attractive because they are fast and can serve as a platform for many types of molecules and cells, but they suffer from the drawback of low efficiency because the physical force that is responsible for intracellular delivery is also responsible for causing cellular damage, making a trade-off between maximizing intracellular uptake and maximizing cell viability [49, 141, 167].

We recently introduced an intracellular delivery method involving laser-activated carbon nanoparticles [108, 168]. The method involves exposing cells in a dilute suspension of carbon black (CB) nanoparticles to nanosecond-pulsed laser. In previous studies, high levels of intracellular uptake of molecules present during laser exposure were seen with high viability. We hypothesize that laser irradiation of CB nanoparticles selectively heats the nanoparticles, which results in particle expansion, liquid vaporization and/or chemical reaction ($C (s) + H_2O (l) \rightarrow CO (g) + H_2 (g)$), each of which generates acoustic pressure waves that can interact with the cell membrane to transiently permeabilize it.

Using this approach, drug molecules can diffuse into cells, but if the membrane permeabilization is too severe, it can result in death of the cell. Extensive cell viability loss can occur under strong laser fluence and/or long exposure times. The goal of this study is to protect cells from irreversible damage associated with membrane permeabilization in order to increase cell viability and thereby increase uptake efficiency as well.

The literature suggests a number of strategies to increase cell viability during photoacoustic delivery. In one approach, addition of poloxamer surfactants has been shown to prevent cell death from mechanical insult [169]. For example, F-68 poloxamer has been shown to prevent cells from dying in a gas sparge reactor [170], to promote drug delivery into cells during electroporation [171] and to save muscle cells from death after high-voltage electrical injury [172], and F-127 poloxamer has been shown to increase gene transfection

and viability during ultrasound exposure [173]. Poloxamers used in this study consist of hydrophilic ethylene oxide (EO) and hydrophobic propylene oxide (PO) blocks arranged in a triblock structure with strings of EO monomers flanking a core of PO monomers [174, 175]. Poloxamers have been hypothesized to protect cells from shear-induced damage by reducing cell-bubble interactions, increasing plasma membrane fluidity and resealing holes in lipid bilayer membranes [171, 176]. Other approaches have addressed the effects of elevated intracellular Ca^{2+} on cells, which has been shown to mediate cell death, especially by apoptosis, after cell membrane permeabilization by acoustic cavitation and other physically traumatic interventions [42, 177-180]. Previous studies showed that controlled addition and/or chelation of Ca^{2+} could be used to modulate cell viability; Ca^{2+} chelation can be accomplished using the well-known Ca^{2+} chelator BAPTA-AM [181]. We also hypothesize that ATP, which provides cellular energy [182] and fetal bovine serum, which provides nutrients, growth factors and other protective compounds [183], could help protect cells from lasting damage. Finally, glycine betaine (GB) has been shown to accumulate in cells without causing osmotic stress [184] and protects the cells in two ways: as an osmoprotectant by accumulating at high concentrations inside cells [185] and as a chemical chaperon [36], which deteriorates protein aggregation and enhances renaturation after heat shock [186].

4.2 Materials and Methods

4.2.1 Cell Preparation

Human prostate carcinoma cells (DU145, American Type Culture Collection, Manassas, VA) were cultured as monolayers in a humidified atmosphere of 95% air and 5% CO_2 at 37°C in RPMI-1640 medium (Cellgro, Herndon, VA), which was supplemented with 100 g/ml penicillin-streptomycin (Cellgro) and 10% (v/v) heat-inactivated fetal bovine serum (FBS, Corning, Palo Alto, CA) in T-150 flasks (BD Falcon, Franklin Lakes, NJ). For each experiment, cells at 80-90% confluence were harvested by trypsin/EDTA (Cellgro) digestion, washed using fresh growth medium with FBS and re-suspended in RPMI at a cell concentration of 10^6 cells/ml.

4.2.2 Nanoparticle Preparation

To prepare the CB nanoparticle solution, 20 mg of CB (Black Pearls 470, Cabot, Boston, MA) were added to 50 ml of 0.013% (v/v) Tween 80 (Sigma-Aldrich, St. Louis, MO; added to reduce aggregation and settling of the nanoparticles) in DI water and sonicated for at least 15 min to obtain the final CB solution at a concentration of 400 mg/l. The size of the individual CB nanoparticles was 25 nm, but they were aggregated into larger particles of 189.3 ± 1.5 nm ($n = 3$) diameter with a dispersity of 0.16 ± 0.03 ($n = 3$), as determined from dynamic light scattering measurements. After making the 50 ml solution of CB nanoparticles, it was aliquoted into smaller 1.5 ml samples. Consistency of samples was determined by measuring the absorption spectra using a spectrophotometer (Synergy H4, BioTek, Winooski, VT) and compared to predetermined standards.

4.2.3 Additive Preparation

BAPTA-AM (Sigma-Aldrich) is a cell-permeant Ca^{2+} chelator in live cells, effectively sequestering Ca^{2+} from interacting with other molecules. For chelation experiments, a stock solution containing 130 mM BAPTA-AM in dimethyl sulfoxide was added to cell solutions immediately after the laser exposure to a final concentration of $260 \mu\text{M}$ at room temperature. To increase the extracellular Ca^{2+} concentration, a stock 10 mM CaCl_2 (Sigma-Aldrich) solution in DI water was added at a final concentration of $200 \mu\text{M}$ before the laser exposure. Adenosine triphosphate (ATP, Sigma-Aldrich) is the basic energy unit of eukaryotic cells that directly provides cells with energy. ATP was added at a final concentration of $100 \mu\text{M}$ before laser exposure from a stock of 5 mM ATP in DI water. Glycine betaine (GB, Life Extension, Ft. Lauderdale, FL) was used as a thermoprotectant in this study. A stock of 50 ml of 100 g/l was prepared by adding GB powder to DI water. A volume of $50 \mu\text{l}$ of the stock was added to the cells before exposure and cells were incubated for 30 min at room temperature for internalization of GB into the cells. Pluronic F-68 and F-127 (BASF, Florham Park, NJ) were added to the cell suspension at 2%, 5% and 10% (v/v) from a stock solution of $120 \mu\text{M}$ and $150 \mu\text{M}$, respectively.

4.2.4 Laser Apparatus

A Nd:YAG infrared laser (Powerlite II Plus, Continuum, Santa Clara, CA) was used to apply pulses of 1064 nm wavelength, 5 - 9 ns pulse length, and 100 - 175 mJ energy per pulse. Pulses were applied at a repetition rate of 10 Hz (i.e., 10 pulses per second). The energy was varied by manipulating the amplifier voltage of the system. The beam was passed through a Faraday isolator to prevent back reflection. The 12 mm-diameter laser beam was passed through a 9 mm-diameter aperture to block the edges of the beam and thereby obtain a more uniform top-hat profile. The resulting 9 mm-diameter beam was then usually diverged to a 1.4 mm diameter using a lens to illuminate the entire cuvette (exposure area of 4 cm²). Sham exposures were used as negative control experiments, where solutions containing cells, calcein and CB nanoparticles went through all the same steps as exposed samples (see below), except that the laser was not turned on. Another negative control involved only cells without CB nanoparticles or calcein.

4.2.5 Sample Exposure

A volume of 520 μ l of cells at a concentration of 10⁶ cells per ml was suspended in RPMI, transferred to 1.5 ml microcentrifuge tubes (Eppendorf, Hauppauge, NY) and stored on ice until exposure. CB nanoparticle stock solution was added to achieve a final concentration of 25 mg/l CB nanoparticles, unless otherwise noted. In some experiments different concentrations of CB nanoparticles were used. High purity calcein (Molecular Probes, Eugene, OR) was used as an uptake marker and was added from a stock solution at a final concentration of 10 μ M. The final solution was mixed thoroughly by vortexing and then exposed to laser in cuvettes (37-PX-2, Starna Cuvettes, Santa Clara CA) made from Pyrex glass. The top part of the cuvette was cut at 2 mm from the base of the neck to facilitate transfer of liquids. A total volume of 563 μ l of the mixture was transferred to the cuvette using a transfer pipette. The cuvette was placed in a custom-made stand to hold it during laser exposure. The entire cuvette was exposed to laser pulses.

After laser exposure, cells were transferred back to microcentrifuge tubes and stored on ice to reduce uptake due to endocytosis until all the samples were done. Propidium iodide

(Invitrogen, Grand Island, NY) was added at a concentration of 7.5 μM and cells were incubated for at least 10 min to label necrotic and late apoptotic cells. Next, cells were centrifuged at 500 g for 6 min and washed with PBS (Cellgro) supplemented with 10% FBS twice. After the third centrifugation, the cells were suspended in PBS and then transferred to flow cytometer tubes or were put on microscope slides and cover slipped for microscopic imaging.

4.2.6 Analysis and Quantification

A bench-top flow cytometer (BD LSRII, BD Biosciences, San Jose, CA) was used to quantify uptake, i.e. the number of live cells with intracellular calcein, and viability, i.e. the number of live cells that were not necrotic as determined by propidium iodide staining or fragmented, on a cell-by-cell basis. For quantifying necrotic death, propidium iodide (PI) staining was analyzed using a PerCP-Cy5, 670 nm longpass filter. Calcein uptake into cells was detected using a FITC, 530/28 nm bandpass filter. A cell gate was constructed based on forward-scattered and side-scattered light to determine the size distribution of cells in the control. Any events lying within this gate were considered to be cells, whereas events smaller than that were considered cells fragments or dead cells.

To determine the fraction of intact cells post-irradiation compared to sham (and thereby account for possible cell loss due to fragmentation and necrotic death), we compared the number of PI-negative cells detected within the gate for the exposed sample and the sham. The flow cytometer was run for 90 s, which resulted in collection approximately 10^5 cell events per sample ($\sim 20\%$ of the total cells present in each sample).

To account for spectral overlap between the dyes, compensation controls were run for each experiment. Propidium iodide-positive samples were made by incubating cells in 70% methanol for 30 min and then washing with PBS. Calcein-positive samples were made by exposing cells with CB nanoparticles and calcein at 44 mJ/cm^2 per shot for 7 min. At this condition, there was extensive cell death, but almost all cells which remained viable had calcein uptake.

In some experiments, a bench-top cell sorter (BD Aria) was used to separate populations that were PI-positive, i.e. nonviable cells, from cells that were PI-negative. In these experiments, at least 95% of the cellular solution was run through to get enough samples in each population. After the two sorted population were collected in 15 ml centrifuge tubes, they were centrifuged once at 500 g for 6 minutes to remove the flow cytometer sheath fluid and re-suspended in 100 μ l PBS. A drop of this solution was put on a slide cover-slipped and imaged.

Cells were imaged using a fluorescence microscope using appropriate filters (Olympus IX70, Olympus, Center Valley, PA). Cells were observed at 40x magnification to visually inspect cellular uptake in viable cells.

4.2.7 Statistical Analysis

A minimum of three replicates was performed for all conditions. Replicates enabled calculation of means and standard deviation. The null hypothesis was that the average fraction of cells with uptake (or average fraction of viable cells) between a treated sample and a sham exposure were equal. To compare between mean values of two data points, an unpaired Students t-test was performed (2 tails) assuming unequal variances using GraphPad Prism 6 (GraphPad Software, La Jolla, CA).

4.3 Results

4.3.1 Effect of Laser Exposure Conditions on Photoacoustic Delivery of Molecules into Cells and Cell Viability

Previous studies have shown that exposure of cells in the presence of CB nanoparticles to pulsed laser light can lead to intracellular uptake of molecules and loss of cell viability [108, 168]. In general, stronger laser exposure conditions (e.g., higher fluence, longer exposure time) initially increase uptake, but then reduce uptake efficiency due to increased loss of cell viability. The goal of this study is to protect cells from viability loss so that stronger laser exposure conditions can be used to increase uptake further without associated cell death.

We therefore first identified laser exposure conditions that lead to good intracellular uptake, but have significant loss of cell viability. Fig. 4.1A shows data at such conditions

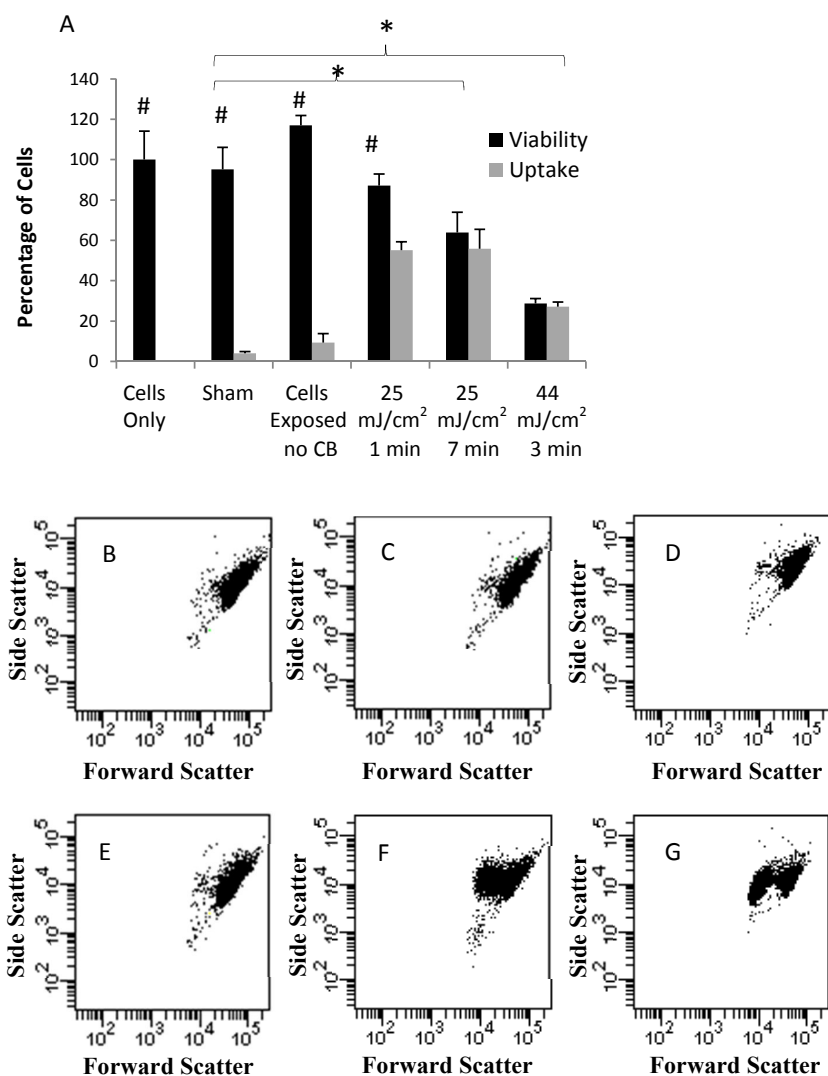


Figure 4.1: Effect of photoacoustic delivery using nanosecond-pulsed laser and CB nanoparticles on uptake and viability of DU145 prostate cancer cells. (A) Percentage of cells remaining viable and exhibiting intracellular uptake of calcein is shown as a function of photoacoustic exposure conditions, including laser fluence (mJ/cm²) and exposure time (min). Representative flow cytometry scatter plots are shown for cells at the same six conditions shown in part (A): (B) untreated cells (cells only), (C) cells exposed to CB nanoparticles but no laser (sham), (D) cells exposed to laser (44 mJ/cm², 7 min) but no CB nanoparticles, and cells exposed to CB nanoparticles and laser at (E) 25 mJ/cm², 1 min, (F) 25 mJ/cm², 7 min and (G) 44 mJ/cm², 3 min. The asterisk symbol (*) represents statistical difference of viability between two samples ($p < 0.05$) and hash symbol (#) signifies that uptake and viability for a given sample are significantly different ($p < 0.05$). Data show average \pm standard deviation (SD) with three replicates each ($n = 3$).

for intracellular delivery of a model compound (calcein) into a model cell type (DU145 prostate cancer cells). When cells incubated with CB nanoparticles and calcein were not exposed to laser (sham), there was minimal uptake (Students t-test, $p = 0.04$) and no significant change in viability (Students t-test, $p = 0.4$). Cells exposed to high-fluence laser (44 mJ/cm^2 for 7 min) without CB nanoparticles similarly showed minimal uptake (Students t-test, $p = 0.04$) compared to cells with no treatment and no significant loss of viability compared to both sham and cells with no treatment (Students t-test, $p > 0.06$ 0.3). This shows that exposure to laser alone or exposure to CB nanoparticles alone has little effect on cells under the conditions used in this study.

When cells were exposed to laser (25 mJ/cm^2 , 1 min) and CB nanoparticles, 55% of cells exhibited uptake of calcein (Students t-test, $p < 0.001$), while viability did not change significantly (Students t-test, $p = 0.4$), which demonstrates the synergistic effect of CB nanoparticles and laser exposure resulting in the uptake of calcein. When the exposure time was increased to 7 min, while keeping the power constant at 25 mJ/cm^2 , the uptake remained constant at 55%, but the viability went down to 63%, which was significantly lower than the sham (Students t-test, $p = 0.04$). Because there was no statistically significant difference between uptake and viability at this condition (Students t-test, $p = 0.6$), this means that essentially all viable cells had uptake and that the barrier to still higher uptake was preventing loss of viability (note that uptake in this study is expressed as a fraction of all cells exposed to laser and not a fraction of just those remaining viable after laser exposure). When we increased the laser fluence to a higher level (44 mJ/cm^2) at an intermediate exposure time (3 min), we observed even lower uptake of 27%, which was essentially equal to the viability of 28%.

When the size distribution of the flow cytometry events recorded in cell samples are plotted in terms of forward and side scatter (log values), we found that control cells with no treatment displayed a tight distribution on the upper right corner, corresponding to relatively large (high forward scatter) and textured (high side scatter) events (Fig. 4.1B). There was almost no PI or calcein staining of events in this population (data not shown). Our belief is that these events are intact (based on forward and side scatter) and viable

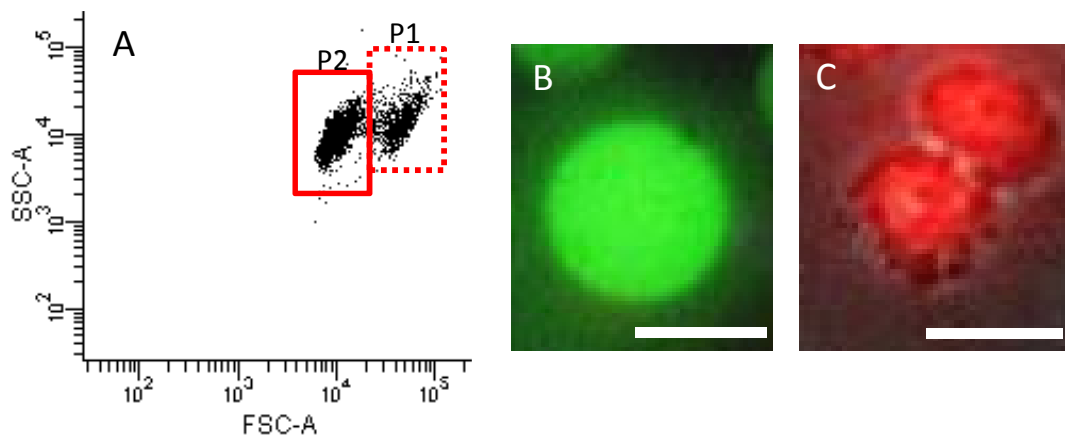


Figure 4.2: Cell sorting between two populations of cells seen after exposure to strong photoacoustic conditions. (A) Representative flow cytometry scatter plot of cells exposed to CB nanoparticles and laser at 44 mJ/cm^2 , 3 min. Fluorescence microscopy image shown of representative cells from (B) the population with higher forward scatter (P1), exhibiting green fluorescence from calcein uptake and (C) the population with lower forward scatter (P2) exhibiting red fluorescence from PI staining. Scale bars are $20 \mu\text{m}$.

(based on lack of PI staining) cells without calcein uptake (based on lack of calcein staining).

When sham control cells and cells exposed to laser without CB nanoparticles were assessed (Figs. 4.1C and 4.1D), we found that these populations looked similar to cells without any treatment (Fig. 4.1B). Cells exposed to laser at 25 mJ/cm^2 for 1 min (which caused little loss of viability, see Fig. 4.1A) also did not exhibit significant changes in the scatter plot (Fig. 4.1E), with most of the cells PI-negative (intact, viable cells) and many of the cells calcein positive (intact, viable cells with uptake) (data not shown).

In contrast, cells exposed to harsher laser conditions associated with significant cell death resulted in visibly different scatter plots that included two populations (Figs. 4.1F and 4.1G). The original population remained, with a few cells PI positive (intact, nonviable cells) and most of the cells calcein positive (intact, viable cells with uptake) (Fig. 4.2B). The other population had similar side scatter, but weaker forward scatter, indicating a smaller size. These events all stained positive for PI, indicating that they were nonviable

(Fig. 4.2C). We interpret the events in this new population as remnants of nonviable cells, consistent with previous observations [42]. In conclusion, we interpret only those cells in the population with higher forward-scatter and no PI staining as viable cells and only cells in that population having calcein uptake with no PI staining as uptake cells. Most of the nonviable cells were found in the lower forward-scatter population, corresponding to PI-positive cell remnants (i.e., very few cells were PI-positive in the higher forward scatter population or in the lost population of fragmented cells). The goal of this study is to prevent cells from being part of the PI-positive, low-forward scatter population of nonviable cells and instead retain them in the PI-negative, high-forward scatter population of viable cells.

4.3.2 Effect of Poloxamer Surfactants

To prevent the cell death seen at strong laser exposure conditions, we tested the hypothesis that these strong laser conditions would lead to high levels of uptake if viability loss could be prevented. We first tried adding poloxamer surfactants to cells during and after laser exposure, because these nonionic triblock copolymers have been shown to protect cells from mechanical damage associated with shear stresses and other physical forces, possibly mediated by sealing leaky membranes or other interactions with the cell membrane [171, 176].

As a control experiment shown in Fig. 4.3A, we first incubated cells with three different concentrations (2, 5, and 10% (v/v)) of the poloxamer Pluronic F-68 (i.e., F-68 sham) and found that viability and uptake were unaffected compared to the untreated sham (Students t-test, $p > 0.6$). Cells were then exposed to the laser (25 mJ/cm², 7 min) in the presence of Pluronic F-68 at the same three concentrations, which resulted in somewhat higher viability and uptake compared to cells exposed to the laser without Pluronic F-68, but these differences were not statistically significant (Students t-test, $p > 0.1$). Despite the lack of significant effect of poloxamer at the conditions tested, we next chose a more powerful laser exposure condition (44 mJ/cm², 3 min), where we would normally kill about 75% of the cells, and added the highest concentration of Pluronic F-68 (10% (v/v)), as shown in Fig. 4.3B. In this case, there was a significant increase in both viability and uptake due to the

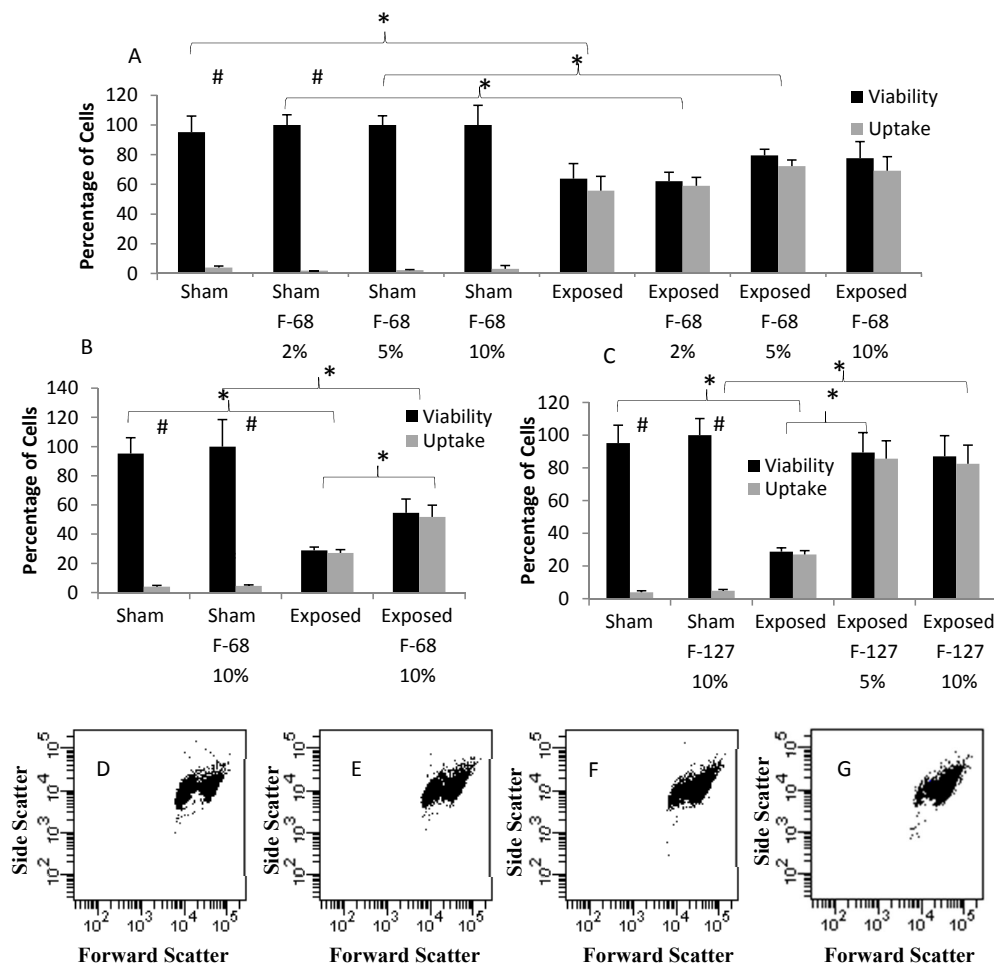


Figure 4.3: Effect of poloxamer surfactants on the viability and uptake of DU145 cells when exposed to laser in the presence of CB nanoparticles. (A) Effect of F-68 poloxamer at different concentrations (2%, 5%, 10% (v/v)) on cell viability and uptake with sham or actual exposure to laser (25 mJ/cm², 7 min). (B) Effect of F-68 poloxamer at 10% (w/v) concentration on cell viability and uptake with sham or actual exposure to laser (44 mJ/cm², 3 min). (C) Effect of F-127 poloxamer at different concentrations (5%, 10% (v/v)) on cell viability and uptake with sham or actual exposure to laser (44 mJ/cm², 3 min). Representative flow cytometry scatter plots are shown for cells exposed to laser (44 mJ/cm², 3 min) with (D) no poloxamer, (E) 10% (v/v) F-68 poloxamer (F) 5% (v/v) F-127 poloxamer, (G) 10% (v/v) F-127 poloxamer. The asterisk symbol (*) represents statistical difference of viability between two samples (p < 0.05) and hash symbol (#) signifies that uptake and viability for a given sample are significantly different (p < 0.05). Data show average \pm SD (n = 3).

addition of the poloxamer. The laser-exposed samples with Pluronic F-68 had 55% of cells viable and 52% of cells with intracellular uptake of calcein, compared to 28% viability and 27% uptake among cells exposed to the laser without the poloxamer (Students t-test, $p = 0.02$ for viability and $p = 0.015$ for uptake).

The reason why the poloxamer was able to increase cell viability at the more powerful laser exposure condition (Fig. 4.3B), but not at the moderate laser exposure condition (Fig. 4.3A), may have a statistical explanation. Perhaps the bigger difference in viability between sham cells and laser-exposed cells at the more powerful laser exposure condition provided a larger dynamic range between the viability levels of the two control groups, which facilitated establishing statistically significant differences from the controls due to the poloxamer.

Building off these results, we hypothesized that a different poloxamer, Pluronic F-127, would provide still better protective effects because of its greater molecular weight and hydrophobicity [187], which might facilitate its interaction with cell membranes and sealing of membrane pores. Consistent with this hypothesis, cells exposed to laser without poloxamer had 28% viability and 27% uptake (Fig. 4.3C). Remarkably, the addition of F-127 poloxamer increased viability and uptake both to approximately 90%.

We can interpret this finding by examining scatter plots associated with these data. Laser-exposed samples without poloxamer show the two characteristic populations, including the intact cells on the right and the cell remnants on the left (Fig. 4.3D). The addition of the less-effective F-68 poloxamer shifted some cells from the left population to the right (Fig. 4.3E). Addition of the more-effective F-127 poloxamer shifted even more of the cells to the right (Figs. 4.3F and 4.3G). This indicates that the addition of poloxamer protected the cells from damage, thereby retaining them in the PI-negative, high-forward scatter population of viable cells and saving them from the PI-positive, low-forward scatter population of nonviable cells.

4.3.3 Effect of Cell-Repair Mechanism Enhancers

We next tried to increase cell viability using chemicals that enhance active cellular repair mechanisms. The approach was guided by previous studies of intracellular delivery by

acoustic cavitation and other mechanical wounding of cells. This literature shows that after making hole(s) in the cell membrane, (i) Ca^{2+} enters the cell, thereby signaling to the cell that its plasma membrane has been breached, (ii) the cell undergoes active repair of the plasma membrane using intracellular lipid vesicles and (iii) excessive and extended high levels of intracellular Ca^{2+} can be toxic to the cell [42, 180].

We first addressed possible toxic effects due to elevated intracellular Ca^{2+} levels by determining if addition of a Ca^{2+} chelating agent (i.e., BAPTA-AM) immediately after laser exposure could reduce viability loss. As shown in Fig. 4.4A, a control experiment that incubated cells with BAPTA-AM (i.e., BAPTA-AM sham) without laser exposure was no different in terms of uptake and viability than the sham without BAPTA-AM (Students t-test, $p = 0.3$ for both uptake and viability). To test our hypothesis, cells incubated with BAPTA-AM immediately after laser exposure (25 mJ/cm^2 , 7 min), however, showed no statistical difference from laser-exposed cells without BAPTA-AM in terms of viability or uptake (Students t-test, $p = 0.21$ for both viability and uptake). This indicates that Ca^{2+} chelation immediately after laser exposure did not significantly affect viability or uptake.

Cell membrane resealing can be an energy-intensive process requiring active repair mechanisms by the cell [180]. For this reason, we hypothesized that addition of ATP during and after laser exposure could facilitate membrane repair and thereby reduce cell death. Fig. 4.4B shows that in the control experiment, incubation with ATP by itself (i.e., ATP sham) had no effect on viability or uptake compared to the sham without ATP (Students t-test, $p = 0.5$ for viability and $p = 0.4$ for uptake). When cells were incubated with ATP during and after laser exposure, however, there was no statistical change in viability or uptake relative to sham (Students t-test, $p = 0.92$ for viability and $p = 0.54$ for uptake). This indicates that addition of ATP did not protect the cells from viability loss.

Because Ca^{2+} can play a dual role of signaling the need for repair initially, but becoming toxic later, we hypothesized that cell viability and uptake could be increased by the addition of Ca^{2+} and ATP before and during laser exposure to promote plasma membrane repair and addition of BAPTA-AM immediately after laser exposure to prevent toxic effects of extended exposure to intracellular Ca^{2+} . Fig. 4.4D shows that the control experiment

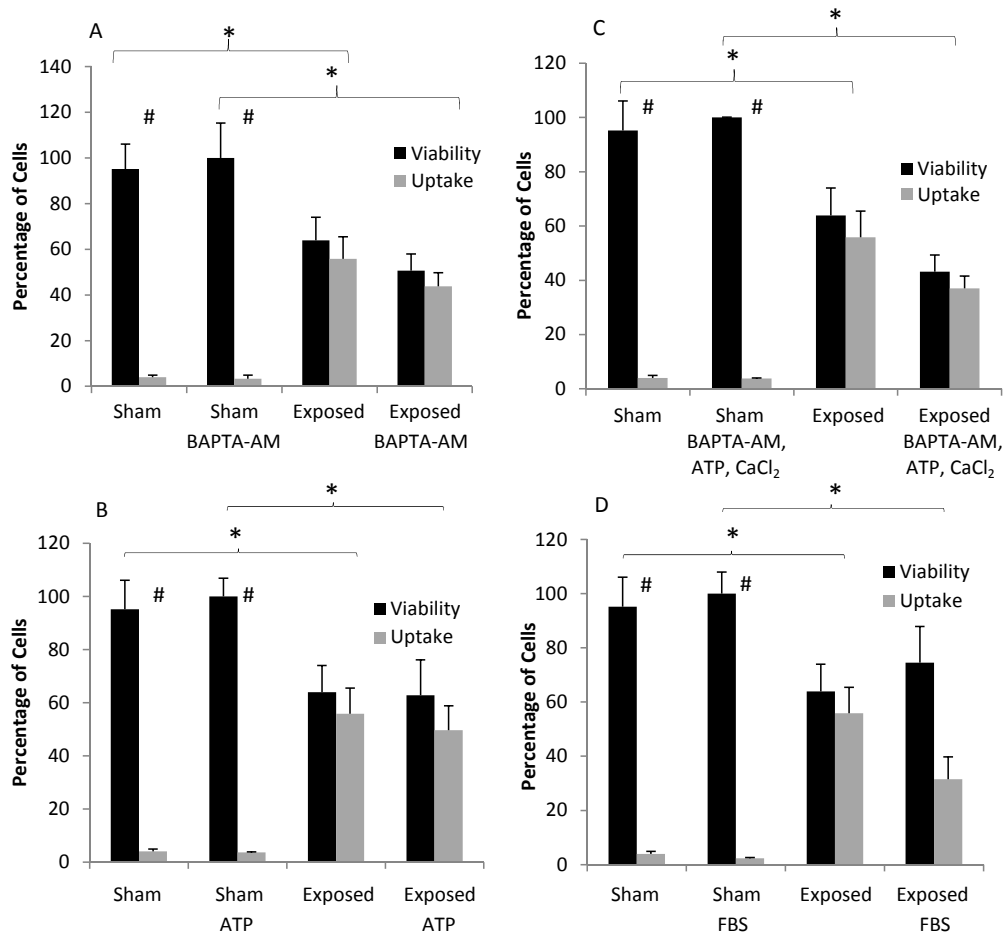


Figure 4.4: Effect of treatment with various cell-repair mechanism enhancers on the viability and uptake of DU145 cells when exposed to laser in the presence of CB nanoparticles. (A) Effect of BAPTA-AM, an intracellular Ca^{2+} chelator, added before laser exposure. (B) Effect of ATP, a source of cellular energy, added before laser exposure. (C) Effect of ATP and CaCl_2 , which triggers plasma membrane repair mechanisms, added before laser exposure and BAPTA-AM added after laser exposure. (D) Effect of FBS, a source of nutrients, growth factors and protective compounds found, added before laser exposure. The asterisk symbol (*) represents statistical difference of viability between two samples ($p < 0.05$) and hash symbol (#) signifies that uptake and viability for a given sample are significantly different ($p < 0.05$). Data show average \pm SD ($n = 3$).

involving the sequential addition of Ca^{2+} , ATP and BAPTA-AM without laser exposure (CaCl_2 , ATP, BAPTA-AM sham) had no significant effect on viability or uptake compared to the sham without these chemicals (Students t-test, $p > 0.4$). To test our hypothesis, cells exposed to laser and incubated with Ca^{2+} , ATP and BAPTA-AM, however, showed no statistical difference from laser-exposed cells without these chemicals in terms of viability or uptake (Students t-test, $p = 0.07$ for viability and $p = 0.66$ for uptake). This indicates that the combined use of Ca^{2+} , ATP and BAPTA-AM did not significantly affect viability or uptake.

Finally, we hypothesized that the addition of fetal bovine serum (FBS) immediately after laser exposure might help stabilize cells during their recovery. Fig. 4.4E shows incubation in FBS without laser exposure as a control experiment (i.e., FBS sham). In the laser-exposed samples, however, the addition of FBS had no statistically different viability compared to the laser-exposed samples without FBS (Students t-test, $p = 0.42$), but the uptake was slightly lower in the samples with FBS (Students t-test, $p = 0.05$). This indicates that addition of FBS after laser exposure did not significantly affect viability.

4.3.4 Effect of Glycine Betaine

Intracellular uptake in this study is mediated by laser irradiation of CB nanoparticles that heats the nanoparticles and is believed to cause transient disruption of the cell membrane [108, 168]. This could lead to cell damage from the heat, as well as from possible osmotic effects associated with membrane permeabilization. These stresses could play a role in the observed loss of cell viability. We therefore hypothesized that addition of GB to cells before laser exposure could prevent cell death from these damaging effects, because GB is known to protect cells and proteins against heat shock and osmotic damage [184, 186]. Fig. 4.5 shows that the GB sham was statistically no different than the sham without GB (Students t-test, $p = 0.5$ for both viability and uptake). The samples exposed to laser with GB were statistically no different than cells exposed to laser without GB (Students t-test, $p = 0.31$ for viability and $p = 0.21$ for uptake). Thus, the addition of GB during and after laser exposure did not significantly affect cell viability or uptake.

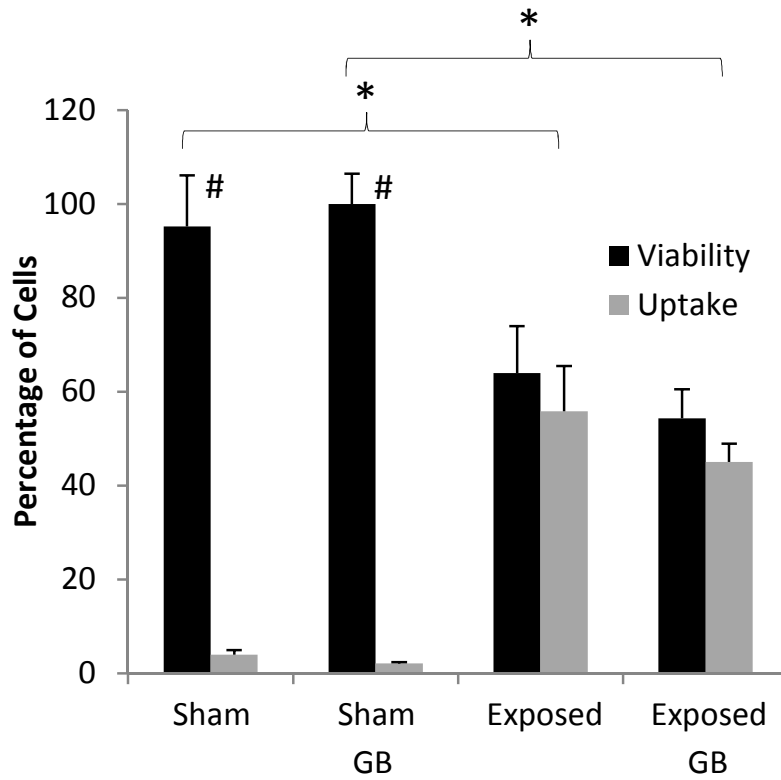


Figure 4.5: Effect of treatment with glycine betaine (GB) on the viability and uptake of DU145 cells when exposed to laser in the presence of CB nanoparticles. The asterisk symbol (*) represents statistical difference of viability between two samples ($p < 0.05$) and hash symbol (#) signifies that uptake and viability for a given sample are significantly different ($p < 0.05$). Data show average \pm SD ($n = 3$).

4.4 Discussion

It is desirable to deliver molecules efficiently into cells without loss of viability. Intracellular delivery methods are often limited by the trade-off between high uptake versus high viability. Our previous work using photoacoustic delivery suffered from the same limitation [168]. The goal of this study is, therefore, to protect cells from viability loss and thereby achieve both high uptake and high viability.

Flow cytometry analysis indicated that nonviable cells were partially intact cell remnants (Fig. 4.1), as opposed to fully fragmented cells. This is consistent with previous reports, for example, after exposure to acoustic cavitation under conditions used to drive intracellular uptake [50]. This is important, because it should be easier to protect a cell from damage that leaves the cell structure largely intact than from damage that fragments the cell into many pieces.

We found that poloxamers were able to protect cells from loss of viability. Previous studies have hypothesized that poloxamers can be incorporated in the cell membrane [169, 188] to decrease membrane fluidity and thereby increase its resistance to shear in vitro [173]. However, such a resistance to mechanical damage to the cell membrane would not only protect cell viability, but would also be expected to decrease intracellular uptake, because the membrane would be less susceptible to poration. Others have hypothesized that poloxamers could help seal leaky membranes by associating with the cell membrane surface at sites of poration [189, 190]. This latter hypothesis would not interfere with membrane pore formation, which is needed to increase intracellular uptake, but should help in membrane resealing through membrane-poloxamer interaction, thereby increasing cell viability. Poloxamers have previously been shown to increase cell viability after electroporation [171, 172], where pore resealing is thermodynamically driven largely on the sub-second time scale, without the need for active cellular processes [191].

The ability of the F-127 poloxamer to protect cells more effectively than the F-68 poloxamer can be attributed to difference hydrophobic and hydrophilic balances of the polymers [170]. F-68 has the structure (EO)75-(PO)30-(EO)75 and F-127 has the structure (EO)100-(PO)65-(EO)100, where EO represents the hydrophilic ethylene oxide monomers,

PO represents the hydrophobic propylene oxide monomers, and the numbers represent the number of monomeric units in each block of the triblock copolymers [174, 175]. Based on the ratio of EO and PO, F-127 is more hydrophobic than F-68 and has more interaction sites to incorporate in the membrane. F-127 also has a longer chain, which gives it a better chance of plugging a bigger hole, which may result in greater success in saving cells.

Other methods that we studied to protect cells were not effective. The use of techniques involving Ca^{2+} , BAPTA-AM, ATP and FBS were hypothesized to protect cells by promoting cell membrane resealing by active mechanisms known to occur after cell membrane disruption by other mechanisms [42, 180], but they did not show significant effects in this study. In our previous study [168], the data suggested that membrane disruption associated with intracellular delivery and cell viability was repaired within 100 ms after firing of the laser. This suggests that the events leading to loss of cell viability occur during this time scale, which may explain why methods to improve active cell-repair mechanisms were unsuccessful, since active cell repair of cell membrane breaches has been reported to occur on a time scale of minutes [42, 180].

GB, which is known to protect cells against heat shock and osmotic effects [184, 186], also did not have significant protective effects on cells in this study. We expect that GB was able to reach its sites of action inside cells [192], because it is a small molecule (MW = 117 Da) that should have been taken up efficiently during the laser exposure, if not during the incubation period. It may be that the active intracellular processes influenced by GBs protective response to heat shock and other insults are not relevant to protection against photoacoustic cell viability loss in this study.

The finding that photoacoustic delivery combined with poloxamer surfactant can yield efficient intracellular delivery is significant. The combination overcomes the common trade-off between increasing intracellular uptake versus preserving cell viability. The use of poloxamer enables stronger photoacoustic conditions to be used in order to increase uptake while still maintaining cell viability. Moreover, the fact that poloxamer is the protective additive is also fortunate, as a various of different poloxamers, including F-127, are used in approved pharmaceutical formulations [187], which facilitates possible future uses of photoacoustic

delivery with poloxamer surfactant in medical applications.

4.5 Conclusion

Photoacoustic delivery into cells using laser-activated CB nanoparticles has the potential to be an efficient method for intracellular delivery of bioactive molecules. This study showed that loss of cell viability could be reversed by addition of poloxamer surfactant during photoacoustic exposure. More specifically, addition of 10% (v/v) F-127 poloxamer increased viability from less than 30% to more than 90%, which similarly increased uptake to occur in more than 90% of cells. In this way, photoacoustic delivery combined with poloxamer surfactant enabled very efficient uptake into viable cells. In contrast, the addition of BAPTA-AM, Ca^{2+} , ATP, FBS or GB did not protect cells from loss of viability, suggesting that active cell membrane repair mechanisms or other active intracellular protective processes that these compounds mediate may not be responsible for protecting cells against damage from photoacoustic delivery. In conclusion, efficient intracellular delivery of molecules can be achieved by photoacoustic delivery using laser-activated CB nanoparticles in combination with F-127 poloxamer surfactant.

CHAPTER V

MECHANISM OF ENERGY TRANSFER FROM LASER TO NANOPARTICLE TO FLUID MEDIUM TO CELL

Previously we have shown efficient intracellular drug delivery as result of laser irradiation of carbon black (CB) nanoparticles. In this study we try to understand the underlying mechanism of energy transduction from the laser to the final cell membrane breach. We hypothesize that the laser heats the nanoparticles leading to thermal expansion, vapor bubble formation and/ or chemical reaction which results in the production of acoustic waves. Then all of these phenomena interact with the membrane to cause drug delivery. Through experiments we go step by step to prove and disprove parts of this hypothesis. We find that at 44 mJ/cm^2 , the particle temperature can go as high as 1000°C and there is probably no reaction occurring at the given conditions. The reason for drug delivery might actually be because of vapor cell interaction.

5.1 Introduction

Many infections are intracellular in nature and often require drugs to be delivered into the cells. Unfortunately delivering drugs into the cells is a huge challenge because of the presence of a highly structured lipophilic cell membrane; existence of P-glycoproteins which efflux the drugs out [193]; the occurrence of degradative enzymes, and the development of endosomes which are highly acidic [17] and which degrade xenobiotics that are endocytised into the cells. Thus very highly specialized systems capable of overcoming these barriers can achieve successful intracellular drug delivery. Currently, a variety of techniques exist to deliver drugs into cells, each with some sort of drawback.

Many of the techniques are based on mimicking natural processes that are known to breach the cell membrane, such as the use of lipophilic molecules which passively diffuse through the cell membrane [194], or taking advantage of the endocytotic pathway by using receptor-targeted ligands on nanoparticles [195]. However such systems have a slow rate of

uptake, and there are toxicity issues associated with the process. Viral systems which are naturally known to penetrate the cell membrane are useful for delivery of DNA but also suffer from the virus induced cyto-toxicity [139].

Another class of intracellular drug delivery methods relies on physically disrupting the membrane using a physical force and achieving delivery of molecules by either passive diffusion or in some cases, though electrophoretic mobility of charged molecules through short lived pores [39]. Some examples of this kind of technique include electroporation [140], ultrasound mediated intracellular drug delivery [49, 142] and microinjection [143]. Laser-based methods have been used for some intracellular drug delivery applications, including heating nanoparticles to either cause cell membrane disruptions [146-150] or cell death [151]. They have also been used to generate pressure waves from shock tubes to induce uptake by mechanical mechanisms [144, 145]. The primary challenge associated with any of these methods is the achievement of high uptake rates while maintaining high cell viability, since the physical force creating transient pores also causes cell death if not carefully controlled.

An alternative technique employing nanosecond laser irradiation of carbon black (CB) nanoparticles in solution with cells demonstrated high uptake of calcein with high viability [196]. The belief was that the laser-CB interaction caused temporary disruption of the cell membrane, leading to uptake of molecules. This technique showed promise of delivering even bigger molecules like mRNA, proteins and SiRNA, but the specific permeabilization mechanisms were not understood. We hypothesize a four step process: first, a portion of the incident laser energy is absorbed by nanoparticles, which raises their temperature; second, the heated nanoparticles expand in size and transfer heat to the surrounding liquid, which vaporizes the liquid and possibly drives chemical reaction; third, nanoparticle and bubble expansion generate acoustic emissions and finally, the energy from the heated and expanded nanoparticles and surrounding bubbles is transferred to the cell membrane, which transiently increases its permeability. In the present paper, we primarily address the first three parts of the hypothesis. We will also touch on the possible causes of membrane disruption, but the nature of cell membrane structural re-organization under mechanical stress to allow transient permeabilization is beyond the scope of this study and has been

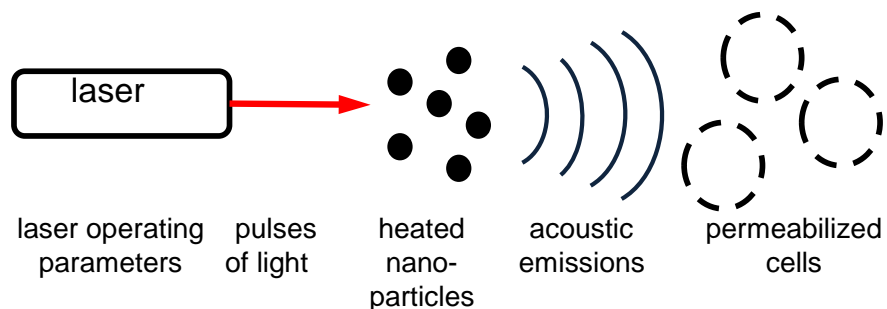


Figure 5.1: A schematics of laser carbon interaction and drug delivery. The nanosecond laser heats the carbon black (CB) nanoparticles and heats them, producing a pressure wave along with a vapor bubble. This leads to intracellular drug delivery of calcein.

addressed in other contexts before [55].

5.2 *Materials and Methods*

5.2.1 **Laser Apparatus**

A Nd:YAG nanosecond (Surelite III, Continuum, Santa Clara, CA) was used to irradiate samples. The pulse duration was 5 - 7 ns operated either in the single shot mode or in the continuous mode at a pulse repetition rate of 10 Hz for exposure times of 1 - 60 min (i.e., 600 - 36000 pulses). Laser fluence was varied between 18.75 - 446 mJ/cm² per shot. The fluence was varied by manipulating the Q-switching time internally and using polarizable quarter plates (Thorlabs, Newton, NJ) externally. The laser beam (8 mm diameter) was passed through a 3 mm pinhole to achieve a more uniform laser energy profile by only allowing the central portion of the beam to pass. The beam was then either used directly in acoustic measurements or diverged using a convex lens to a final diameter of 21.4 mm for cell-exposure experiments. Measurements with a pyroelectric laser sensor (see below) indicated a variation of less than 1% in laser intensity across the beam profile.

5.2.2 Nanoparticle Preparation

Carbon black (CB) nanoparticles (Black Pearls 470, Cabot Corporation, Alpharetta, GA) were dispersed in DI water at a concentration of 0.4 g/l using a needle sonicator (Sonics & Materials, Newtown, CT) for 5 min. A black-colored aqueous dispersion was obtained, whose absorption spectrum was measured using a spectrophotometer (Synergy H4, BioTek, Winooski, VT). Each time a solution was made, the absorption spectrum was compared to a reference spectrum to maintain consistent sample preparation. The CB nanoparticle stock solution was then either diluted using DI water to a concentration of 25 - 400 mg/l or added to a cell suspension solution (see below) to a final concentration of 12.5 - 75 mg/l. In some cases, the CB nanoparticles were dispersed in pure acetic acid (Sigma-Aldrich, St. Louis, MO) instead of DI water. We found that the absorption spectrum remained essentially unchanged when compared with DI water, as long as the CB nanoparticle concentration was held constant (data not shown).

Gold nanorods (Nanopartz, Loveland, CO), which are engineered to absorb 1064 nm wavelength light, were diluted using DI water to 6% (v/v) from an initial stock solution of optical density (OD) 1.1. The gold nanorods measured 168 nm in length and 25 nm in diameter, according to the manufacturers specifications. An iron oxide nanoparticle suspension in water at an initial concentration of 5 g/l and a mean size of 5 nm (Sigma-Aldrich) was diluted (6% v/v) to a final concentration of 0.3 g/l. Carbon nanotubes (Nanostructured & Amorphous Materials, Houston, TX), in the form of single-walled carbon nanotubes (SWCNT) or multi-walled carbon nanotubes (MWCNT), were diluted in DI water from an initial stock solution of 30 g/l to achieve the same absorption spectrum as a CB nanoparticle solution at a concentration of 0.4 g/l. The resulting SWCNT and MWCNT solutions had concentrations of 1.1 g/l and 0.4 g/l, respectively. The length and diameter of SWCNT were 5 - 30 μm and 1 - 2 nm, respectively, and the length and diameter of MWCNT were 10 - 30 μm and 20 - 30 nm, respectively, as reported by the manufacturer.

5.2.3 Cell Preparation, Exposure and Imaging

Human prostate carcinoma cells (DU145, American Type Culture Collection, Manassas, VA) were cultured as monolayers in a humidified atmosphere of 95% air and 5% CO₂ at 37°C in RPMI-1640 medium (Cellgro, Herndon, VA), which was supplemented with 100 g/ml penicillin-streptomycin (Cellgro) and 10% (v/v) heat inactivated FBS (Corning, Palo Alto, CA) in T-150 flasks (BD Falcon, Franklin Lakes, NJ). For each experiment, cells at 80-90% confluence were harvested by trypsin/EDTA (Cellgro) digestion, washed using fresh growth medium with FBS and re-suspended in RPMI at a cell concentration of $\sim 10^6$ cells/ml.

A volume of 520 μ l of cells was transferred to 1.5 ml microcentrifuge tubes and stored on ice until exposure. CB nanoparticle stock solution was added to achieve a final concentration of ranging from 25 - 75 mg/l CB nanoparticles. High purity calcein (Molecular Probes, Eugene, OR) was used as an uptake marker and was added from a stock solution at a final concentration of 10 μ M. The final solution was mixed thoroughly by vortexing and then exposed to laser in cuvettes (37-PX-2, Starna Cuvettes, Santa Clara CA) made from Pyrex glass. The top part of the cuvette was cut at 2 mm from the base of the neck to facilitate transfer of liquids. A total volume of 563 μ l of the mixture was transferred to the cuvette using a transfer pipette. The cuvette was placed in a holder stand to keep it stationary during laser exposure. The entire cuvette was exposed to laser fluences ranging from 25 - 200 mJ/cm² for 1 minute.

After laser exposure, cells were transferred back to microcentrifuge tubes and stored on ice to reduce uptake due to endocytosis until all the samples were done. Cells were then centrifuged at 500 g for 6 min and washed with PBS (Cellgro) supplemented with 10% FBS twice. After the third centrifugation, the cells were suspended in PBS and then were put on a microscope slides and cover slipped for fluorescence imaging using a fluorescent microscope (Olympus IX70, Olympus, Center Valley, PA) using appropriate filters.

5.2.4 Transmittance Measurements

Nanoparticle solutions at appropriate concentrations were placed in the starna cuvettes and exposed to the laser. A pyroelectric laser sensor (Ophir-Spiricon, LLC, North Logan, UT) with appropriate power rating connected to a power meter (Ophir Nova II, Ophir-Spiricon), was placed in front to measure the energy coming into the system. Then the power sensor was quickly moved to the back of the cuvette to measure the energy transmitted through the cuvette. The cuvette with DI water was used as a control. The difference between in and out energy gave the approximate extinction in the cuvette.

5.2.5 Acoustic Measurements

Parametric assessments of acoustic output from laser-irradiated nanoparticle solutions were carried out using an irradiated stream experiment. An overview of the arrangement of the system for acoustic measurement can be found in supplementary information. Briefly, nanoparticle suspensions were loaded in a 30 ml (BD Falcon) syringe which was connected to a 23 G blunt needle (Brico Medical Supplies, Inc., Dayton, NJ) via a tube extender (Baxter, Deerfield, IL). The blunt needle was held submerged in a bracket inside a 37 l glass-walled water-filled tank. The nanoparticle suspension was injected at a known volumetric flow rate of 85 ml/h using a syringe pump (New Era Pump Systems, Inc., Farmingdale, NY), creating a stable particulate stream. Using a stream surrounded by a relatively large water body eliminated possible artifacts associated with compact sample containers, minimized observational effects over relevant timescales by physically separating the radiating volume from large-scale environmental boundaries (walls and free surface), and also provided a simple method for acquiring statistics on large quantities of suspensions of a particular composition.

Acoustic pressures were measured using a needle hydrophone (HNC-0200, ONDA Corp., Sunnyvale, CA), chosen for its broad response bandwidth, small scattering cross section, and small receiving aperture that minimizes field integration of wave fronts that are not planar or incident normally to the sensitive aperture. The hydrophone was mounted to a moving x-y stage so that the position of the hydrophone could be changed relative to the stream.

The position of the hydrophone relative to the stream needle tip was determined using data collected from a focused ultrasound transducer (Panametrics V310-SU, Olympus) and pulser receiver (Panametrics 5072PR, Olympus). Positions were calculated from cross-correlation of scattered signals from the needle tip and hydrophone tip, needle dimensions, and the speed of sound at the water-bath temperature. Stream acoustic output measurements were typically made at with a 5 mm lateral separation between the hydrophone tip and needle center, but varied between 2 and 10 mm.

Stream acoustic output and positioning transducer data were collected with a 100 MHz digitizer (Cleverscope CS320A, Cleverscope Ltd, Auckland, New Zealand) triggered by a sync pulse from the laser. Background sound levels were continuously monitored and experiments halted when the tank water, incrementally seeded with dilute nanoparticles, generates measureable acoustic output when irradiated without stream flow. Experiments were recorded with a video camera zoomed (Canon EOS 60D, Canon USA Inc., Melville, NY) in on the stream and needle nozzle, allowing post-test estimation of stream dimensions using the needle diameter for reference.

5.2.6 Temperature Measurement

A custom made cuvette made using a rubber gasket between 2 calcium fluoride crystal windows of 1" diameter (Thorlabs), was used to hold the CB suspension for laser exposure. The hole is made in the rubber gasket to let fluid into the space between two windows. The final volume was about 550 μl , which was very similar to the Starna cuvettes. An IR Camera (IRC 900, IRCameras, Santa Barbara, CA) was used to measure the temperature rise in the cuvette. The optical window of the cuvette was designed for optimum transmission from 600 nm to 10 μm , beneficial for both the laser and IR camera. The cuvette, being about 5 mm thick, made them a very good thermal insulator, thus there is little heat loss from the system while heating the laser occurs resulting in a more accurate measurement. A total of 500 μl of CB nanoparticles suspended in DI water at a final concentration of 25 mg/l or 50 mg/l were pipetted in. The system was exposed to laser pulses for 7 minutes at either 25 or 44 mJ/cm^2 for 7 minutes. Photon counts emitted from the cuvette were recorded using

the IR camera during the laser exposure and for another 7 minutes after laser exposure to measure the system cooling. The photon count was later converted to temperature by calibrating against a standard J-type thermocouple.

5.3 Results and Discussion

5.3.1 Intracellular Drug Delivery

Previously [152, 168], intracellular drug delivery was achieved with high viability and efficiency when CB suspension was exposed to low fluence laser pulses in the presence of DU145 cells. The study also demonstrated that the uptake was in the entire cytosol and not just the vesicles or membranes suggesting a membrane breach. Under the optimal condition about 90% uptake was observed with almost no loss of viability. Small molecules had significantly higher delivery than bigger macromolecules like dextran. This suggests that the system creates either small or extremely short lived pores. Fig. 5.2a demonstrates that both laser and CB has to be present if there is to be statistically significant uptake of calcein. The calcein has to be added before the exposure, and adding it after does not result in significant delivery, which indicates that the uptake process is short-lived. From Fig 5.2b it can be observed that as the laser fluence is increased the uptake (green cells) first goes up and then it saturates, whereas when the CB concentration is increased (Fig. 5.2c), the uptake first goes up and then it goes down. In other words, the laser fluence does not have additional effect whereas when CB concentration has a continual effect and it never saturates in the range of parameters tested. Increasing either the fluence or the CB concentration should, in theory, increase the bioeffects because of more/ stronger interaction between the CB and the laser. In fact, what we see in terms of uptake is the effect of fluence saturates beyond a point whereas the effect of CB concentration does not, meaning first there is more uptake and then less uptake because more cells die so effectively the uptake gets lower. In order to investigate this, we decided to look at the process in a step by step manner, the first being the laser absorption by CB and heating, followed by the transduction of that energy into pressure and then finally its impact on the cells.

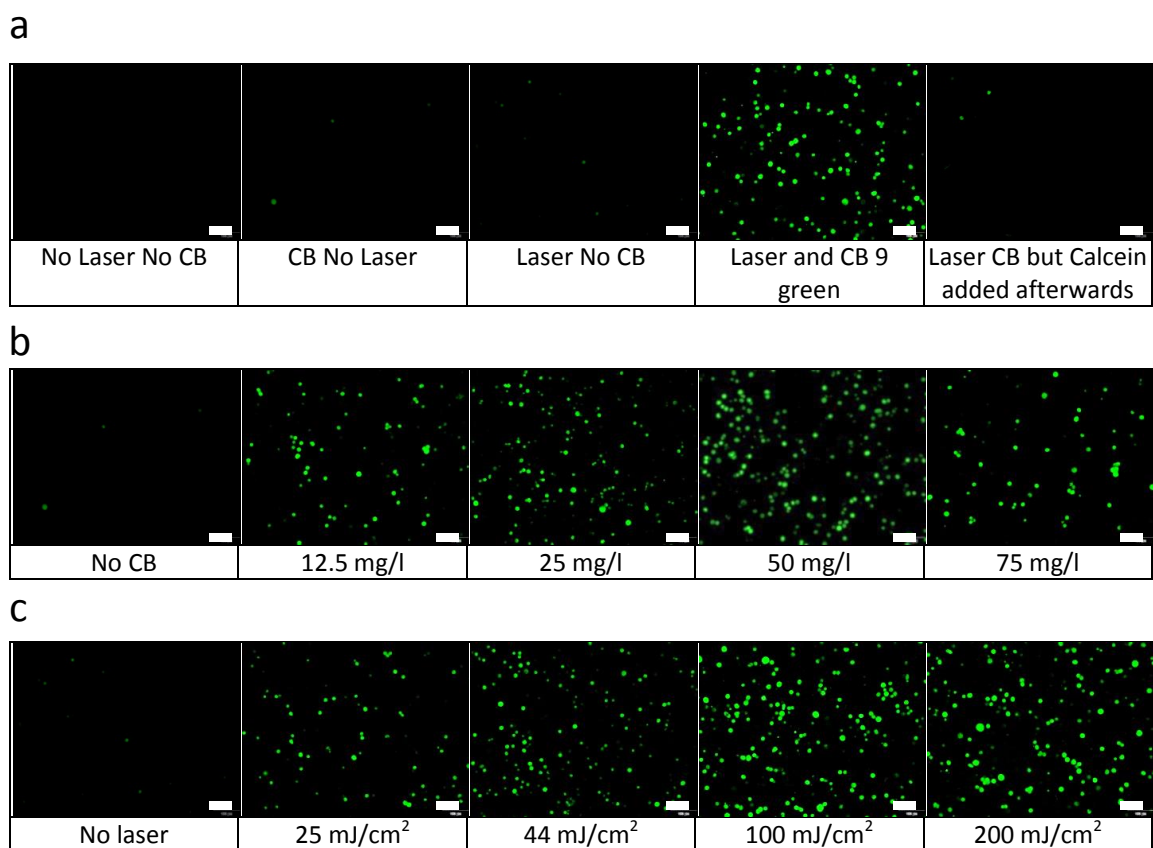


Figure 5.2: Fluorescence imaging of intracellular uptake of calcein in DU145 cells. Both laser and carbon black are necessary for significant uptake of calcein under the conditions tested and calcein should be added before the exposure for delivery to be efficient (a). With increasing concentration of CB the uptake initially increases but after a certain concentration of CB, the uptake falls (b). Calcein uptake initially goes up and then it saturates as the fluence of the laser is increased (c). Scale bars are 100 μm .

5.3.2 Light Absorption and Heating

A spectrophotometer was used to measure the extinction of light by the CB suspension. In the spectrophotometer the highest wavelength achieved was 999 nm, but we believe that the absorption does not change much between 999 nm and 1064 nm based on the previous data from CB absorption spectra [196]. Fig. 5.3a shows that the extinction goes up linearly with concentration (ANOVA, $p < 0.05$). The CB absorbs more in the UV region (300 nm) and less at IR region (999 nm) when the concentration is held constant. Another way to measure the extinction by CB suspension was to use laser power meter to measure the energy coming into the suspension and the amount that is transmitted. The difference between the two should be the amount of energy absorbed and scattered (collectively called extinction). It was found (fig 5.3b) that the extinction of nanosecond laser went up with concentration and it was higher compared to other nanoparticles like iron oxide or gold at the same volume fraction (Student's t-test, $p < 0.05$), which indicated the CB has a greater extinction capability than other nanoparticles on a volume basis. Since in this study we are primarily interested in the heating of the nanoparticles by the laser light, we concentrate on finding the fraction of light energy that was absorbed. Mie theory, which has been previously used extensively to predict the absorption and scattering areas by solving the Maxwells equations for scattering by a spherical entity [197], was used to predict the scattering and absorption by CB particles. Mie theory was modified, as suggested by previous literature [198] to accommodate for particle aggregation in CB suspension. CB aggregates had a mean diameter of 200 nm determined by DLS (see SI), made up of smaller 25 nm spherules. Assuming that the aggregate was spherical it was calculated that there were 133 spherules per aggregate. Scattering and absorption efficiency of these spherules were calculated using Mie theory. The scattering of the total aggregate was summation of the squares of individual areas and absorption was a linear summation of individual spherule absorption areas. Once the total scattering and absorption areas were found, the total energy absorbed was calculated by scaling by the laser fluence. The refractive index of CB played a vital role in determining the absorption and scattering. A refractive index of 2-0.29i was used from previous literature [199]. For 25 mg/l (6% v/v), the total extinction

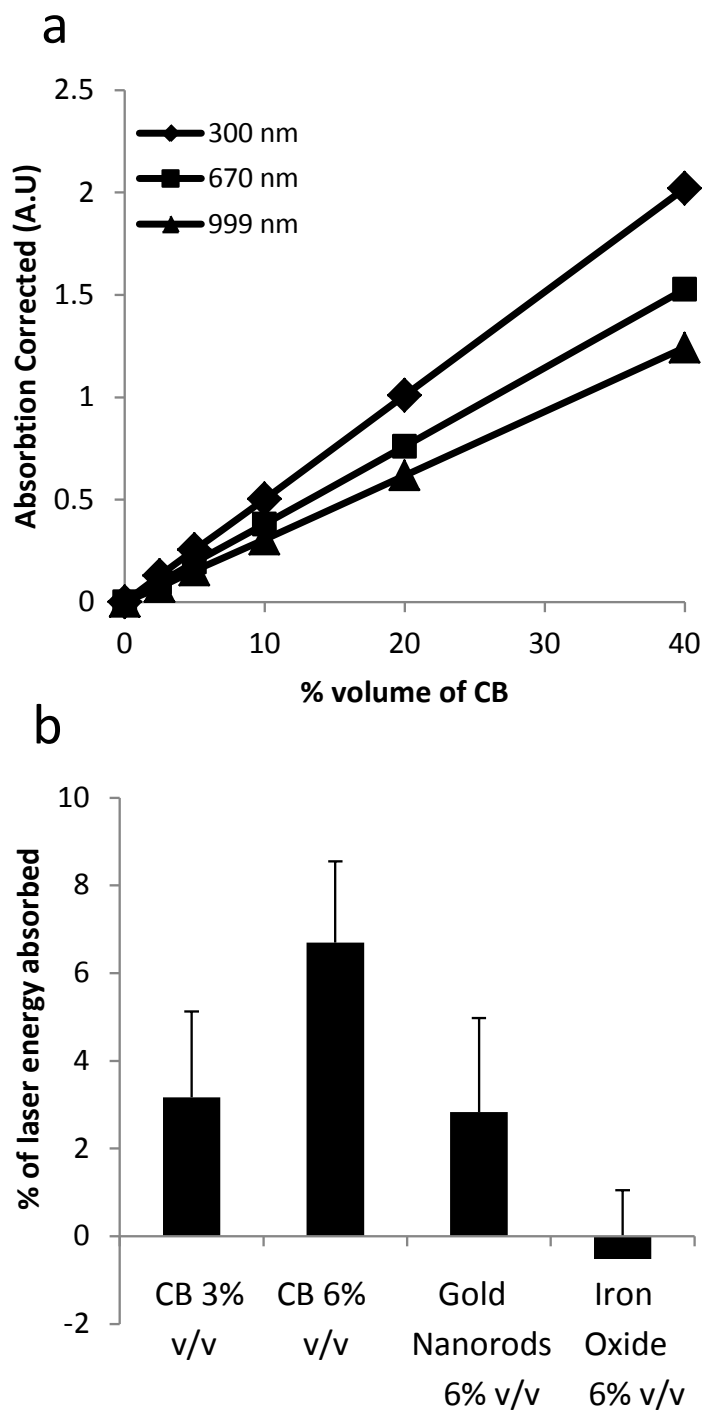


Figure 5.3: Absorption of IR light by CB nanoparticles using two different techniques. Absorption of light increases linearly when CB concentration is increased at different wavelengths of light when measured using a spectrophotometer (a). Absorption of IR nanosecond laser using power meter shows increase in absorption of laser when the concentration of CB is increased (b). Data show average \pm standard deviation (SD) ($n = 3$ replicates).

was calculated from Mie theory was about 6.7% which was in good agreement with the value measured in Fig. 5.3b, which was about 7%. From Mie theory it was also calculated that about 5.8% out of the 6.7% was absorbed and the rest to be scattered. For a fluence of 44 mJ/cm²/pulse over an area of 4 cm², the total energy absorbed by the nanoparticles was found to be 10.15 mJ/pulse.

Another way to determine the total absorption was to first determine the bulk rise of temperature of the CB suspension. Assuming that: i) the particle gets heated to the same temperature every pulse; ii) all the heat that goes into the nanoparticle eventually goes into the bulk water; and iii) the system returns to equilibrium before the next pulse, the heat balance equation is,

$$\dot{Q}_w = m_w C_{pw} \frac{dT}{dt} = \dot{Q}_{w,l} + \dot{Q}_{p,l} + \dot{Q}_{cuvette} - \dot{Q}_{cooling} \quad (5.1)$$

$$\dot{Q}_{cooling} = -h^* A (T_{amb} - T) = -b m_w C_{pw} (T_{amb} - T) \quad (5.2)$$

Solving for T, we get,

$$T - T_i = \left(\frac{\dot{Q}_{tot}}{b m_w C_{pw}} + T_{amb} - T_i \right) (1 - e^{-bt}) \quad (5.3)$$

Where,

$$b = \frac{h^* A}{m_w C_{pw}}, \dot{Q}_{tot} = \dot{Q}_{w,l} + \dot{Q}_{p,l} + \dot{Q}_{cuvette} \quad (5.4)$$

\dot{Q}_{tot} is the total heat absorbed by the system and is assumed to be constant per pulse, T is the bulk temperature, T_i is the initial bulk temperature, h is the heat transfer coefficient, m_w is the mass of water, C_{pw} is the specific heat of water, T_{amb} is the ambient temperature, A is the surface area of the cuvette. If we subtract the total heat absorbed by the water alone from the water with CB nanoparticles we can get the amount of heat absorbed by the nanoparticles. The timescale for the system to reach equilibrium ($L^2/4\alpha_w = 75 \mu s$), where L is inter-particle distance ($= 4 \mu m$, for 25 mg/l CB concentration) and α_w is the thermal diffusivity of water, is much less than the time between the pulses ($= 100 ms$). This means that the system has enough time to reach equilibrium before the next pulse comes in. Fig. 5.4 shows the experimental data (the markers) and the modeled system (the lines). For a fluence of 44 mJ/cm² and CB concentration of 25 mg/l (6% v/v) the heat absorbed per

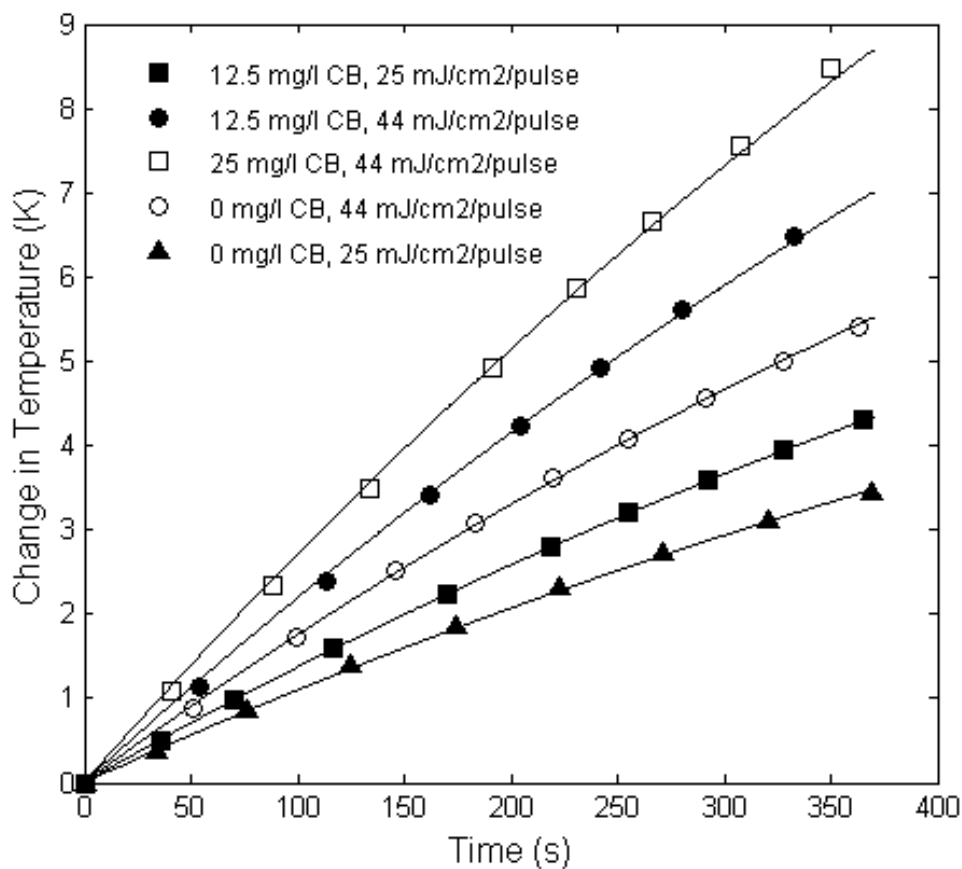


Figure 5.4: Bulk temperature rise measured using an IR camera of a CB suspension at two different concentrations (12.5 and 25 mg/l) and two different laser fluences (25 and 44 mJ/cm²). The temperature rise was lower when CB suspensions were replaced with pure DI water. Higher temperature rise resulted when either the fluence or the CB concentration was increased. The solid lines were the modeled temperature rise.

pulse by the nanoparticles was about 2.75 mJ/pulse. This value was significantly lower than what was calculated from Mie theory or power meter measurements. One of the reasons for the value to be lower might be because a part of the energy is going towards reaction, vaporization and/or pressure generation. These energy losses do not contribute to the bulk rise of the temperature and therefore don't appear in this analysis because potentially they escape the system.

5.3.3 Heating Timescale, Particle Temperature, Bubble Formation and Reaction

The laser pulse is in the order of 10 ns, which given the aggregate diameter of 200 nm, is sufficient time to heat the nanoparticle uniformly. The characteristic timescale for heating the particle is $R^2/4\alpha = 0.011$ ns, where R is the radius of the aggregate and α is the thermal diffusivity of CB, and is seen to be much lower than the pulse length, p_l (=10 ns). Moreover, the parameter $R\lambda < 1$, where λ (=10,000 cm^{-1} [157]) is the absorption coefficient of CB at 1064 nm wavelength, which means that a considerable amount of laser reaches areas of the CB particles far away from the incident beam side. Since we know how much energy got absorbed by the CB nanoparticles (from Mie theory), assuming all the energy went to heating the nanoparticle and there was no loss of heat to the surroundings during the heating process, the peak particle temperature can be calculated from basic calorimetry to be close to 1000°C (see SI) for 44 mJ/cm^2 fluence and 25 mg/l CB concentration. This is expected to occur on the order of tens of nanoseconds, i.e. in the order of the duration of pulse, because the heating timescale is much shorter than pulse length. The maximum temperature is much less than the melting point of CB, so we can assume that there is no melting of CB itself under these conditions.

Since the particle temperature goes beyond 100°C we would expect some of the surrounding liquid water to convert to vapor, leading to formation of bubble. The maximum bubble radius can be achieved if we assume that the final bubble formed is at 100°C so that there is no loss of heat, causing the water vapor to superheat (according to our calculation decrease in density therefore more volume because of superheating steam is less important than creating more steam at 100°C). From this the maximum radius achieved is

around 762 nm. Another way to measure the bubble radius is to assume that the difference in energies calculated with the Mie and IR camera methods goes to vaporization. From those calculations the value comes out to be 645 nm. In either case the size of the bubble is less than 1 μm . Assuming an uniform distribution, the interparticle distance at a CB concentration of 25 mg/l is about 4 μm and particle cell distance is in the similar whereas intercellular distance is about 20 μm at a concentrations of 10^6 per ml used in this study (See SI). Under these circumstances, only the bubbles formed in the vicinity of the cell can interact with the cell membrane making the CB particles very close to the cell relevant if vapor plays a role in the membrane disruption.

Because the nanoparticles are extremely small, they have a very high surface to volume ratio, and hence have a very high heat transfer coefficient. Assuming that there is no heat transfer to the surroundings during the nanoparticle heating may be overly simplistic. A more realistic situation is for heat transfer to the surroundings to occur while the laser is heating the nanoparticle. The maximum heat transfer can occur if we assume that the bulk temperature initially stays constant at 23°C, but when the particle temperature goes beyond 100°C, the water instantly converts to vapor at 100°C and stays that way. It was found that the particle temperature goes beyond 100°C within the first two nanoseconds of heating and there is significant heat loss during that phase from the particle to the surrounding but once there is a vapor shell formed around the particle, it acts as a thermal insulator and then the particle can reach extremely high temperature. Under those conditions the particle temperature goes to about 1000°C after 10 ns of heating. This is basically the same as predicted by no heat transfer; this might be because the heating time scales are too fast. This is further elucidated by the fact that the characteristic timescale for heat transfer to the surrounding, $R^2/4\alpha_w$, is 175 ns, where R is radius and α_w is the thermal diffusivity of water, which is much longer than the pulse duration. Hence, there is little to none heat conduction during the heating of particle which lasts only 10 ns.

Based on predicted particle temperature, there may be a reaction between CB and steam to generate $\text{CO} + \text{H}_2$ through the water-gas pathway. In order for the reaction to occur it has to be both thermodynamically and kinetically feasible. From thermodynamic point of

view, there is enough energy absorbed to consume the entire carbon within 20 pulses if all the energy absorbed goes to reaction and the reaction occurs at 100°C. But even so, the volume of gas produced (CO +H₂) would be a 1/3rd of the volume of vapor produced if all the energy went into vapor formation. In other words, the reaction mechanism is three times less efficient in producing a gas bubble compared to just water vaporization for the same energy delivered to the nanoparticles. From the kinetics perspective, the reaction rates are extremely slow [200] (1.72e-4 m³ of CO+CO₂/kg of C/s at 1300°C) compared to the pulse length, and heat transfer rates which would result in formation of 2.55e-13 m³ of gases per pulse (less than 0.003% of the vapor bubble). So it is not expected to have a significant contribution. If the process is allowed to run for 7 minutes at 10 Hz (4200 pulses) and if the reaction occurs at the predicted rate, only 1% of the CB would be consumed only if a temperature of nearly 1000°C was maintained for the entire time. We consider this unlikely because first there is heat loss to the surrounding in the time scales of 200 ns which reduces the temperature and secondly a certain amount of heat goes into forming vapors which is needed for the reaction to occur. Another way to test the reaction was to expose CB for an hour and testing if there was either a change in absorption or a change in size by DLS. If the reaction occurs even at the slowest rate determined, there should be about 10% reduction in CB content in an hour long exposure, enough to be resolved by spectrophotometric measurement. A 10% reduction in individual particle size should also be evident in DLS. At 44 mJ/cm² laser fluence (an intense exposure condition for in vitro experiments) and up to an hour long exposure, there were no statistical differences observed in either of the measurements, indicating that the reaction might not occur under these conditions (See SI for all the calculations).

5.3.4 Pressure Generation

Fig. 5.5a shows hydrophone data obtained with the laser irradiated stream experiment. The observed delay time between the laser trigger and hydrophone response was as expected for propagation in water between the stream and the hydrophone tip. The data shows a short overall response characterized by a sudden rise to a positive pressure of several atmospheres,

followed by lower level oscillations that are hypothesized to be due to the hydrophone itself. The whole event lasts several hundred nanoseconds which indicate its an extremely fast process. Similar acoustic events have been noted in a liquid metal interface [201]. Fig. 5.5b shows that the frequency spectrum (corrected with the hydrophone factory calibration) is very broad, ranging from several kHz to about 30 MHz after which the signal falls into the measurement noise. The acoustic attenuation coefficient in water increases proportional to the square of frequency, i.e. $\alpha_{ac} = 2.5 \times 10^{-15} \cdot f^2$, [202] where the acoustic attenuation coefficient α_{ac} is given in 1/m and the frequency f is in Hz. At a frequency of 30 MHz, the frequency attenuation at 15 mm is 3.6%, which is within the experimental error bound. It is noted however, that there might be higher frequency components which attenuate even faster and might not be recorded by the hydrophone.

There are four main hypotheses proposed for the generation of acoustic wave from the heating of nanoparticles viz. a) Plasma formation b) Expansion of nanoparticles c) Vaporization of surrounding fluid d) Reaction resulting in bubble formation. Fig. 5.6 shows the dependence of the peak pressure signal from the hydrophone on distance from the source, CB concentration and laser fluence. All the data points are an average of 115 replicates and the error bars are extremely tight which indicated the signal was extremely consistent and repeatable. When the distance from the source was increased the signal decreased in a $1/r$ fashion, which is consistent with literature (ANOVA, $p < 0.0001$) [203]. When the CB concentration was increased the peak pressure signal went up linearly (ANOVA, $p < 0.0001$), as expected when the number of acoustic sources is increased [203]. Peak pressure increased with fluence, although not in linear proportion (ANOVA, $p < 0.0001$). Another experiment that was performed to characterize the system was to see whether the pressure generation was particular to the CB and water system. Fig. 5.7 shows that when water is replaced with pure acetic acid, under the same CB concentration (which also had the same extinction) the peak pressure increased (Student's t-test, $p < 0.001$) by a factor of 1.7. When CB in DI water was replaced with nanotubes, under the same absorbance, single walled carbon nanotubes (SWCNTs) had a higher signal than CB (Student's t-test, $p < 0.001$), whereas multi walled carbon nanotubes (MWCNTs) had a significantly lower

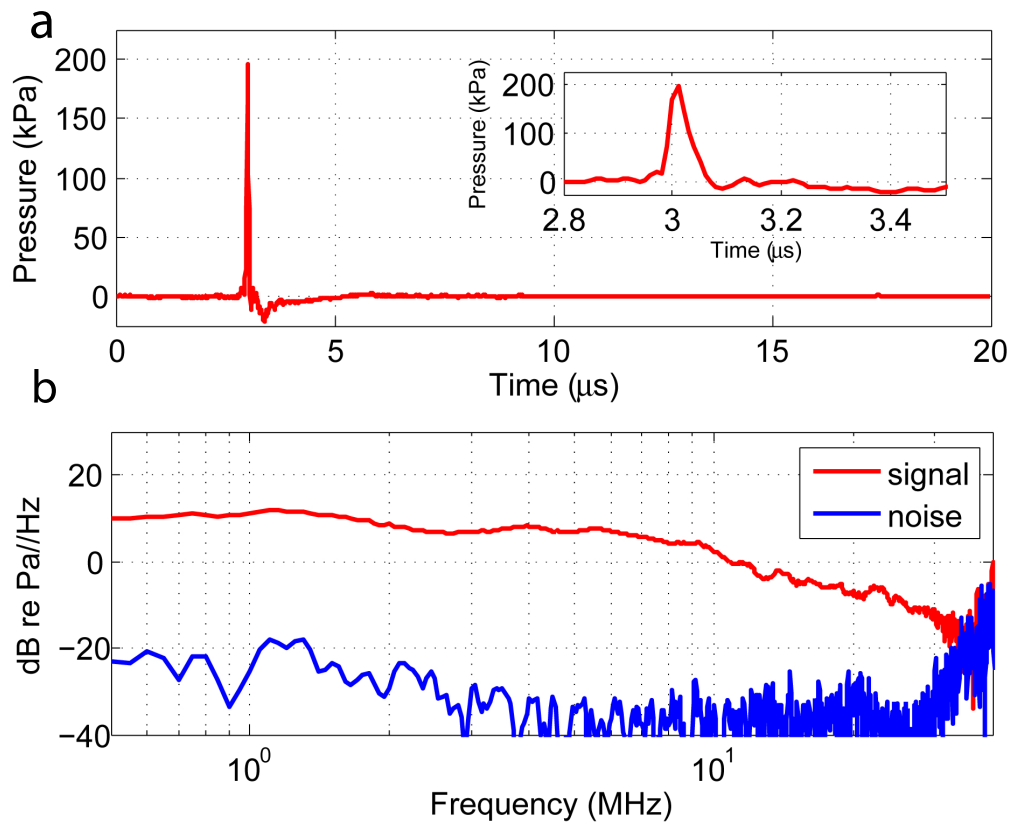


Figure 5.5: Acoustic output of 25 mg/l CB suspension measured using a hydrophone. The time domain shows there is a sudden rise of pressure followed by a slower fall (a). The frequency domain shows the constituent frequency of the system decreases significantly after 30 MHz (b).

signal than CB (Student's t-test, $p < 0.001$). We concluded that the pressure generation is not particular to CB and water system. There are four main hypotheses proposed for the generation of acoustic wave from the heating of nanoparticles viz. a) Plasma formation b) Expansion of nanoparticles c) Vaporization of surrounding fluid d) Reaction resulting in bubble formation.

5.3.4.1 Plasma Formation

Plasma formation is one of the most efficient ways to convert laser energy to acoustic energy. A universal parameter, namely, the conversion efficiency, η , defined as the fraction of energy converted from the laser energy to the acoustic energy, is used to determine the nature and mechanism of pressure generation. Typically η ranges from 10^{-4} for a thermal expansion mechanism [204] to 0.3 for plasma formation and optical breakdown [206]. The conversion efficiency for our case is less than 10^{-5} (see SI), which shows that there is no plasma formation under these fluences.

5.3.4.2 Expansion of Nanoparticles

The particle temperature predictions, along with a volumetric expansion coefficient of 1.8×10^{-4} /K, indicate that the change in diameter of the nanoparticle (assuming a sphere) is about 6%, and the total volume change is about 20%. So the average velocity of the moving wall of the sphere is about 0.9 m/s which is very slow compared to speed of sound.

5.3.4.3 Reaction

The carbon steam reaction is endothermic and both the high heat of reaction and high temperatures need to be maintained for long periods of time for the reaction to occur appreciably. Based on thermodynamic calculations it also appears to be a less efficient use of energy to create a bubble. Reaction between CB and steam might occur but kinetically its extremely slow and might not result in any effect. CB exposed to 44 mJ/cm^2 for 1 h did not show any change in absorbance or DLS measurement data suggesting there was no consumption of nanoparticles. When CB was replaced by nanotubes and water was replaced with acetic acid there was still pressure generation.

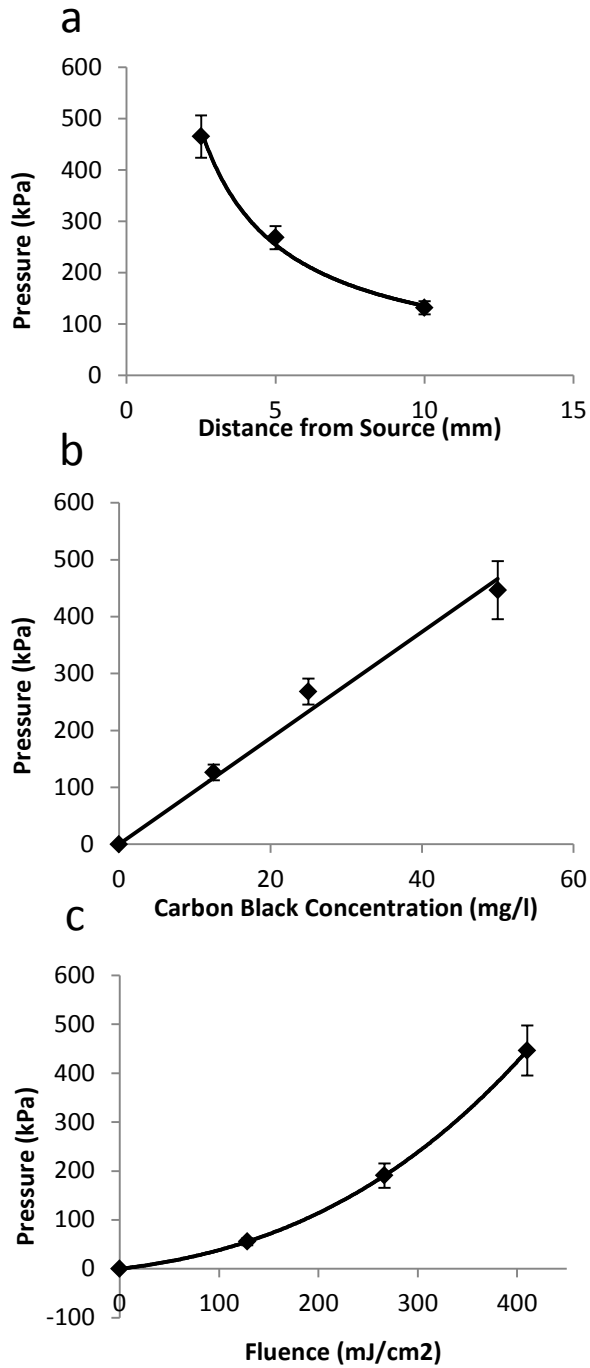


Figure 5.6: Effect of measurement distance from source, CB concentration and Laser Fluence on the peak pressure. Pressure signal is inversely proportional to the distance from the source (a). Increasing the CB concentration increases the signal linearly (b). Increasing the Fluence increases the pressure non-linearly (c). Data show average \pm standard deviation (SD) ($n = 115$ replicates)

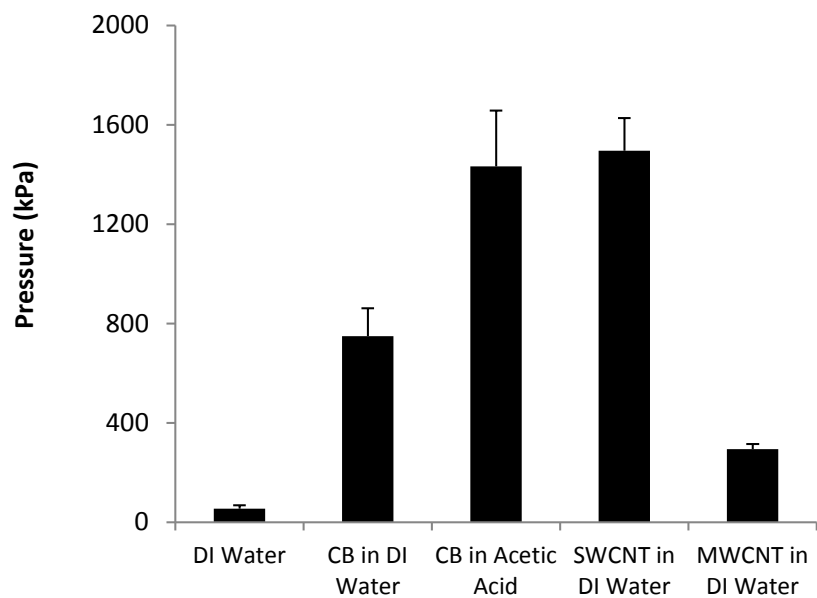


Figure 5.7: Effect of acetic acid and carbon nanotubes on pressure waves. When water is replaced with non-reacting acetic acid and carbon black is replaced with less chemically active nanotubes there was still pressure detected.

5.3.4.4 Vaporization

If the particle temperature as predicted by Mie scattering goes beyond 100°C then some vaporization is expected of the surrounding liquid water. The existence of vapor is also demonstrated by the non-linear rise of peak pressure as a function of fluence. Ideally it should be linear if thermal expansion of nanoparticle was the only mechanism [201]. If the amount of vapor formed is proportional to the total pressure output, it might explain why CB with acetic acid has a higher output. The heat of vaporization of acetic acid is about 1.7 times less than water, therefore under the same fluence a bigger vapor bubble is formed in acetic acid keeping all other parameters the same.

From the above, we conclude that the pressure generation is caused due to a combination of thermal expansion and vapor generation. If that is the case, then getting consistent signal over many pulses also mean that the particle is reaching similar temperature each time a laser pulse interacts with the CB, this justifies our previous assumption in the modeling of Fig. 5.4.

5.3.5 Impact on Cells

In terms of bio-effects one of the key things to note is that while pressure increases with both laser fluence and CB concentration, uptake saturates when fluence is increased, but not when the CB concentration is increased. Drug delivery or membrane permeabilization can occur due to two main reasons: 1) There is a distant, indirect interaction between bubble and cell, mediated through pressure emitted by the nanoparticles; and 2) There is a direct interaction between bubble and cell, mediated through direct contact between the heated vapor bubbles and the cells. To map the spatial domain of the bioeffects, cells and nanoparticles were separated by a saran wrap and then exposed to various laser conditions. The frequency attenuation coefficient, α_{ac} at this distance is so small that the total attenuation is less than 0.0001% for a 30 MHz signal. To account for the pressure attenuation through saran wrap, the calibration curve from Fig 5.6a was used. Assuming a thickness of 10 μm a 14 fold increase in fluence was required to have the same down the line effect across saran wrap as if the cell was in the vicinity of the vapor bubble. No effect

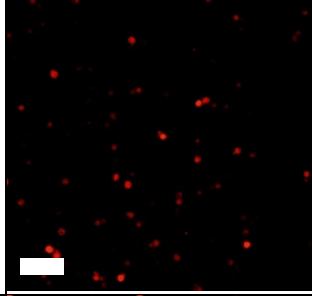
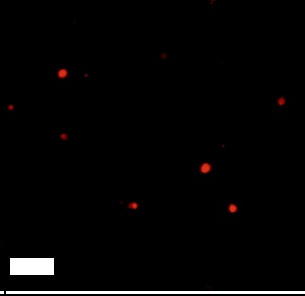
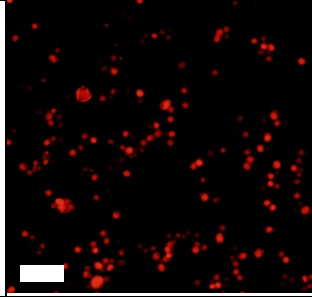
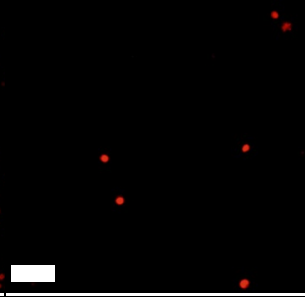
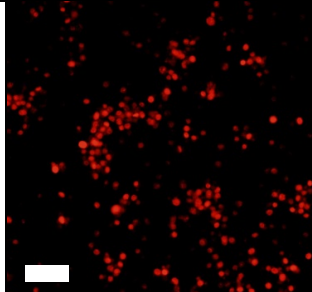
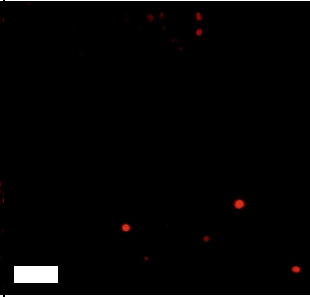
Energy (mj/cm ²)	Fluorescence	Fluorescence
44		
100		
200		

Figure 5.8: Effect of placing a saran wrap between the cells and the nanoparticles. When cells and nanoparticles are placed on the same side there is significant damage observed whereas when they are placed in either side there is no damage observed.

was observed even when a fluence 200 mJ/cm^2 was used. This suggested that either the pressure waves attenuate too fast or a vapor bubble must be physically in the vicinity of the cell. In either case its a short distance effect. Another reason might be that the cells are inhomogeneous themselves and some don't respond to laser treatment while others do, but this seems unlikely because we see a continual effect with increasing CB and time of exposure.

5.4 Conclusion

Laser exposure to CB nanoparticles in the presence of cells leads to intracellular drug delivery. Based on all the presented data, the most likely pathway is:

1. the laser gets absorbed by the nanoparticles and gets converted to heat;
2. the CB then reaches a temperature close to 1000°C at 44mJ/cm^2 laser fluence;
3. Water surrounding the CB vaporizes and forms a vapor shell
4. The bubble growth produces acoustic pressure

The cause of transient cell membrane permeability that facilitates intracellular delivery might not be the pressure waves by themselves, but a vapor cell membrane interaction, which may temporarily re-organize the membrane, resulting in uptake. Such a kind of membrane disruption is expected to be short lived and small, which probably explain why there is high viability associated with the process. The bubble radius is a very weak function of the energy but the number of bubbles produced is linearly proportional to the number of CB nanoparticles. Beyond a threshold a bubble does not have any additional effect explaining why the increase of fluence does not result in additional delivery whereas increasing CB concentration continues to have more and more effect for the range of parameters tested.

We believe this is a new kind of delivery mechanism that has not been proposed in the literature in the past. Cell-bubble contact is new mechanism not proposed before in literature and is very different from ultrasound, electroporation, and fluid mechanical shear. Perhaps this new mechanism explains why we have such efficient uptake, rapidly reversible effects and sharp dependence of uptake on MW. This method owing to its high efficiency has

a potential to be applied to both in-vitro and in-vivo intracellular drug delivery for not just calcein but also molecules like SiRNA, small proteins etc. But understanding this vapor cell interaction is key to future applications and maybe in fact, vapor cell interaction generated by other techniques can result in a high efficiency intracellular drug delivery system.

CHAPTER VI

siRNA DELIVERY USING PHOTOACOUSTICS

The introduction of short-interfering RNA (siRNA) into cells is an attractive tool for RNAi-mediated knock-down of gene expression for research and therapeutic purposes. However, delivery of siRNA into cells has been challenging. To address this challenge, here we report, for the first time, on a method that involves irradiation of carbon black (CB) nanoparticles with near-infrared (NIR, 1064 nm), nanosecond (5 - 9 ns) laser pulses to achieve intracellular delivery of siRNA. In initial studies, physical properties of CB nanoparticles were characterized and then ovarian cancer cells irradiated by NIR laser in the presence of CB nanoparticles were shown to have significant uptake of fluorescein isothiocyanatedextran (FITC-dextran, 70 kDa). Follow-up studies demonstrated significant uptake of siRNA targeting the epidermal growth factor receptor (EGFR) gene, as well as down-regulation of the target EGFR gene on the mRNA level. This new physical method for siRNA delivery expands the tools available for RNAi-mediated gene knock-down and may show future promise for delivery of therapeutic siRNAs for treatment of ovarian cancer and other indications.

6.1 Introduction

Since the discovery of siRNA-mediated gene knockdown in *C. elegans* [109] and its subsequent implementation in mammalian cells [206], this method has gained considerable attention because it has the potential to knock down any specific gene in the body and specifically modulate more therapeutic targets than typical small-molecule drugs [207]. Using this RNA interference (RNAi) approach, *in vitro* and *in vivo* studies have already demonstrated therapeutic potential of siRNA-mediated gene knock-down in diseases like hypercholesterolaemia [208], liver cirrhosis[209], hepatitis B virus (HBV) [210, 211], human papilloma-virus[212] and bone cancer [213]. Human clinical trials are also underway [214, 215]. However, a key challenge to clinical translation is delivering siRNA into cells, because siRNA molecules are big (~ 13 kDa), heavily negatively charged and subject to degradation

by endogeneous enzymes in-vivo [131, 207].

Most of the current techniques to deliver siRNA involve the use of viral vectors [216, 217], lipid vesicles [183, 218], solid nanoparticle formulations [219-221] or hydrodynamic injections [222]. Viral methods suffer from drawbacks like cytotoxicity, insertional mutagenesis and activation of immune response [223, 224]. A major hurdle in non-viral delivery is avoiding endosomal degradation and achieving endosomal escape [225-227]. Another approach is to directly deliver siRNA into cytoplasm, which avoids the endocytic pathway completely. Examples of such methods are electroporation, ultrasound-induced poration, microinjection etc. A common challenge with these methods is to maintain high viability at conditions associated with high intracellular uptake [65].

In this study, we propose a method that uses laser-irradiated carbon black (CB) nanoparticles to achieve intracellular delivery of siRNA. In this method, we expose CB nanoparticles to nanosecond pulsed laser, causing the nanoparticles to preferentially heat up, which results in particle expansion [84], liquid vaporization [84, 228] and/or chemical reaction ($C + H_2O \rightarrow CO + H_2$)[5], followed by generation of acoustic waves, leading to poration of cell membranes [168, 229]. Molecules then passively transport into the cell without the need of endocytosis. Previously we demonstrated this method to be very efficient in delivering small molecules like calcein and larger proteins like bovine serum albumin [168, 229]; here we seek to extend the application to siRNA.

This method of intracellular delivery does not involve internalization of the CB nanoparticles, unlike other methods of intracellular delivery based on laser-particle interactions [230]. In our approach, the nanoparticles transduce laser energy (i.e., photons) into mechanical energy (i.e., acoustic waves) that impact the cell membrane to increase its permeability [168]. In this way, siRNA provided in the extracellular medium can then diffuse directly into its area of target, i.e., cytoplasm, where the mRNAs are present. For this reason, we believe the siRNA delivery to the cytoplasm is especially well suited to delivery by laser-activated CB nanoparticles, as opposed to, for example, DNA, which typically has an intranuclear target for transfection.

We carried out this study in ovarian cancer cells in anticipation of future applications

to treat ovarian cancer. Ovarian cancer is the most lethal of all gynecological cancers and the fifth leading cause of cancer-related deaths in women in the United States [231]. According to the U.S. National Cancer Institute, in 2014 there will be almost 22,000 new cases of ovarian cancer and more than 14,000 women will die of this disease nationally [232]. Current treatment of advanced ovarian cancer, which includes debulking surgery and platinum-based chemotherapy, is initially effective in the majority of patients; however, most of them eventually develop disease recurrence [233].

We have previously shown that targeting epidermal growth factor receptor (EGFR) by siRNA-mediated gene knock-down increased sensitivity of ovarian cancer cells to a traditional anticancer agent cisplatin [234]. This suggests that EGFR can serve as a viable target for development of siRNA-based therapies of ovarian cancer.

In this study, we first tested the hypothesis that laser-activated CB nanoparticles cause enhanced uptake of FITC-dextran (70 kDa) by ovarian cancer cells and then show uptake of anti-EGFR siRNA into ovarian cancer cells and knockdown of EGFR protein. We believe that this is the first study to examine intracellular delivery in ovarian cancer cells and the first to demonstrate siRNA delivery and knock-down using laser-activated CB nanoparticles.

6.2 Delivery System Design

The long-term goal of this study is to introduce nanoparticles into a tissue, irradiate the tissue with laser in order to heat the CB nanoparticles selectively through absorption of the laser energy by the nanoparticles, which causes them to generate acoustic emissions leading to intracellular delivery of siRNA into ovarian cancer cells.

Given this goal, we chose to irradiate the CB nanoparticles with a 1064 nm wavelength NIR laser because light at this wavelength can be generated using relatively inexpensive commercial lasers and is poorly absorbed by biological tissues [235], thereby enabling deeper penetration in tissues [236]. We chose CB nanoparticles as the photoacoustic transducers because they absorb IR light efficiently [237], can be of suitable size for injection and enhanced permeation and retention (EPR) effects [238], and have been shown to generate photoacoustic emissions [5].

To make CB nanoparticle suspensions, commercial CB powder was dispersed in an aqueous solution of Tween 80, a non-ionic surfactant, using a needle sonicator for 15 min at a final concentration of 400 mg/l. Dynamic light scattering showed that this process yielded CB nanoparticles with a mean particle size of ~ 200 nm and a dispersity of 0.21 (Fig. 6.1A). Further analysis by transmission electron microscopy revealed that the CB nanoparticles were aggregates of even smaller spherules of 25 - 30 nm in size (Fig. 6.1B inset). Assuming a spherical shape (with a 200 nm diameter) for the aggregate and a spherical shape (with a 25 nm diameter) for the spherules, we calculated that each aggregate had ~ 133 spherules. Given our goal of heating particles to generate photoacoustic emissions, nanoparticle size and composition are critically important. Nanoparticle temperature is maximized by preventing heat transfer from the nanoparticle to the surroundings during the laser exposure, so that all heat is retained within the nanoparticle. Minimizing heat loss is achieved by reducing thermal conductivity and surface-to-volume ratio of the nanoparticle. CB has a relatively low thermal conductivity (e.g., compared to metal nanoparticles) [237], which facilitates heat retention and. at 200 nm mean diameter. The time scale of thermal conduction to the surroundings is ~ 175 ns (see SI) which is much slower than heat deposition time scale of the laser pulse (i.e., 5-9 ns). In contrast, the time scale of heat loss to the surroundings for a 50 nm diameter nanoparticle is ~ 11 ns (see SI), which is similar to the laser pulse length, suggesting that a 50 nm nanoparticle is too small, because it would lose heat to its surroundings during the pulse. Moreover, as nanoparticle size decreases, the melting point of decreases as well [239], which further motivated us to avoid making nanoparticles too small. We therefore concluded that 200 nm nanoparticles would be effective for our application.

We finally tested the acoustic output of the CB nanoparticle suspension when subjected to laser irradiation. To do so, CB suspensions were exposed to pulsed nanosecond lasers and pressure signals were detected using a hydrophone. CB suspensions exposed to 100 mJ/cm² produced a peak pressure of 0.17 MPa measured at a distance of 5 mm from the CB suspension (Fig. 6.1B); the pressure within the CB suspension was probably significantly higher. The pressure wave was characterized by an initial delay, which can be attributed

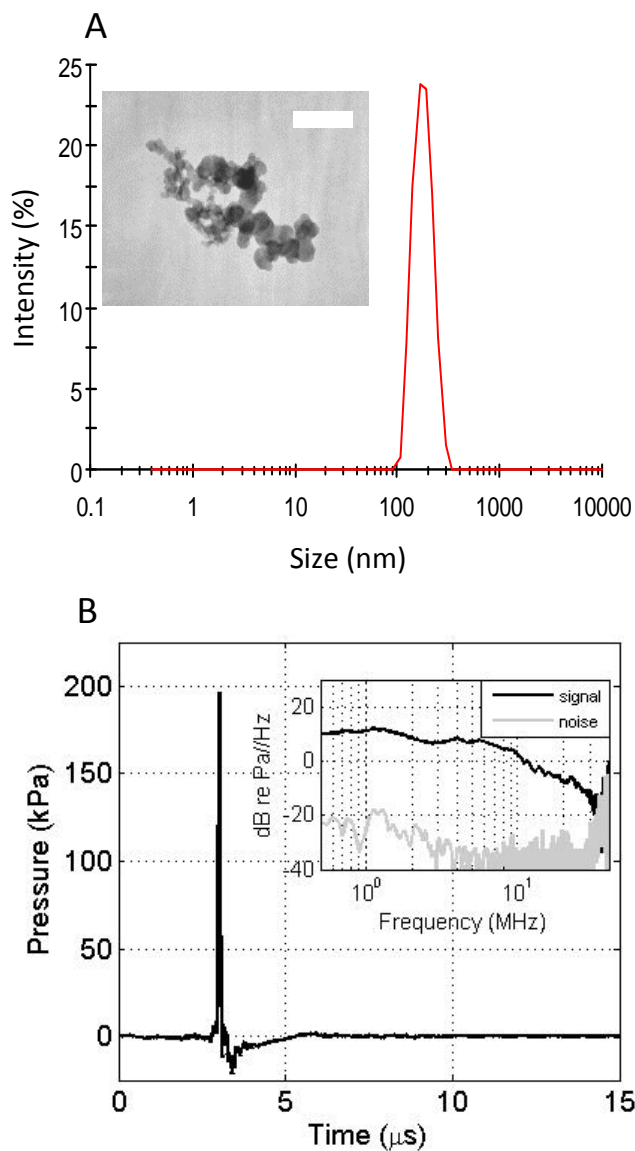


Figure 6.1: Physical characterization of carbon black (CB) nanoparticles. (A) Representative dynamic light scattering measurement of hydrodynamic diameter of CB nanoparticle aggregates in DI water suspension at a final concentration of $25 \mu\text{g/l}$ shows a single peak and no particle settling. Transmission Electron Microscope image (inset) of dried CB nanoparticle aggregates shows the individual spherules constituting the aggregates. The scale bar is 50 nm. (B) Representative acoustic output (pressure) versus time measured using a hydrophone when CB nanoparticle suspension (50 mg/l) was exposed to a single laser pulse at 250 mJ/cm^2 fluence. The frequency distribution calculated from the hydrophone calibration curve reveals a broadband signal up to approximately 30 MHz (inset).

to the time for the acoustic wave to reach the detector from the source (i.e., $t = d / c = (0.005 \text{ m}) / (1490 \text{ m/s}) = 3.35\text{e-}06 \text{ s}$, where t is time delay, d is distance between the CB nanoparticle suspension and hydrophone and c is the speed of sound in water at 23°C), followed by a sudden rise of pressure within 100 ns, followed by a slower recovery within $1 \mu\text{s}$. The whole event from pressure rise to negligible signal lasts less than $1 \mu\text{s}$, which suggests that the sound generation was due to an expansion-type mechanism involving thermal expansion of CB nanoparticles themselves or expansion of vapor/gas bubbles produced by heat transfer from the hot CB nanoparticles [84]. The frequency spectrum showed a broad range of signals from few kHz up to 30 MHz, beyond which the signal became largely indistinguishable from background noise. Overall, these studies show that the CB nanoparticles and laser irradiation conditions used in this study are capable of generating photoacoustic outputs.

6.3 Intracellular Drug Delivery with Laser Activated CB

To address our long-term goal of treating ovarian cancer by intracellular delivery of siRNA, we next identified conditions that enable efficient delivery of molecules into ovarian cancer cells guided by prior literature [168]. Human ovarian cancer cells, Hey A8-F8 cells, were mixed with CB nanoparticles and 70 kDa FITC-dextran (used as a surrogate for siRNA), exposed to laser, washed by centrifugation and then imaged by fluorescence microscopy and analyzed quantitatively by flow cytometry (Fig. 6.2). Cells with intracellular uptake of FITC-dextran were identified by green fluorescence. Non-viable cells were identified by red-fluorescent propidium iodide staining.

Microscopic imaging revealed that laser-irradiation with CB nanoparticles induced uptake of FITC-dextran (as indicated by the green cells) and caused loss of cell viability (as indicated by the red cells) (Fig. 6.2A). Flow cytometry analysis provided quantitative data (Fig. 6.2B). In control experiments using untreated cells (i.e., cells with no FITC-dextran, no CB nanoparticles and no laser irradiation) or sham-treated cells (i.e., cells with FITC-dextran and CB nanoparticles, but no laser irradiation), there was high viability and negligible uptake. We next exposed cells to three different laser-irradiation conditions,

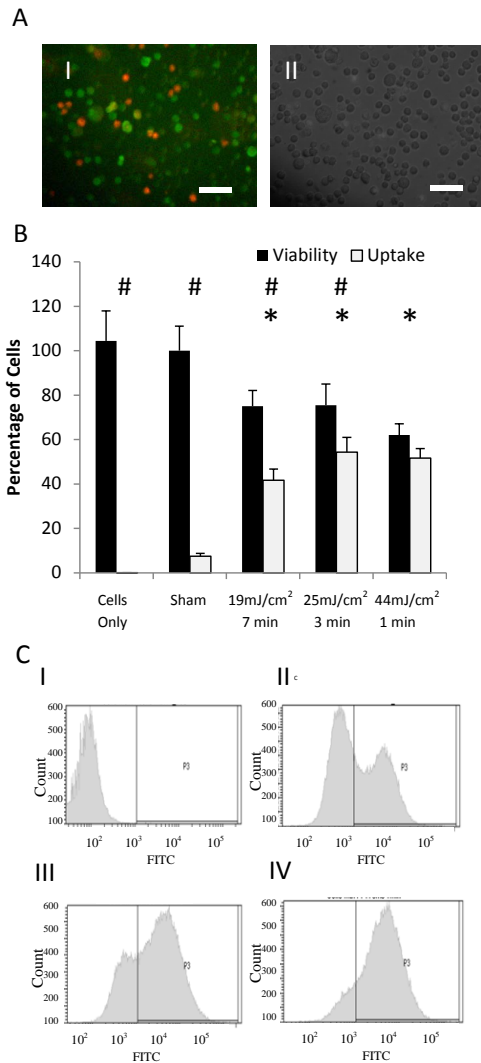


Figure 6.2: Intracellular delivery of FITC-dextran in Hey A8-F8 ovarian cancer cells. (A) Cells inspected by microscopic imaging show uptake of 70 kDa FITC-conjugated dextran (green) when cells were exposed to laser at 44 mJ/cm² for 1 min in the presence of 25 mg/l CB nanoparticles. Cells were also stained with propidium iodide (red), which is a marker of nonviable cells: (I) fluorescence microscopy, (II) brightfield microscopy. Scale bars are 100 μ m. (B) Flow cytometric analysis of percentage of cells remaining viable and exhibiting intracellular uptake of dextran is shown as a function of photoacoustic exposure conditions, including laser fluence (mJ/cm²) and exposure time (min). The asterisk symbol (*) represents statistically different viability compared to sham samples ($p < 0.05$) and the hash symbol (#) signifies that percentage of cells with uptake and viability for a given sample are significantly different ($p < 0.05$). Data show mean \pm standard deviation (SD) with three replicates each ($N = 3$). (C) Representative flow cytometry histogram plots of FITC-dextran fluorescence are shown for cells incubated with FITC-dextran at four conditions shown in (B): (I) untreated cells (no laser, no CB nanoparticles), and cells exposed to CB nanoparticles and laser at (II) 19 mJ/cm², 7 min (III) 25 mJ/cm², 3 min, (IV) 44 mJ/cm², 1 min.

which were selected because they had previously been shown to drive intracellular uptake into another cell line DU145 prostate cancer cells [168] and we therefore expected them to be similarly effective in the ovarian cancer cells used in this study. At each of these three laser irradiation conditions, there was significant uptake of FITC-dextran (Students t-test, $p < 0.05$) with associated loss of viability (Students t-test, $p < 0.05$). More specifically, all three laser-irradiation conditions led to similar effects: uptake seen in about half of the cells and loss of viability in about one-third of the cells (Fig. 6.2B). These results are similar to those seen with the prostate cancer cells previously [168].

Closer examination of the flow cytometry data allowed us to assess the relative intracellular concentration of FITC-dextran taken up into the cells. The representative histogram plots (Fig. 6.2C) show the levels of green fluorescence among the viable cells in each sample. In graph I, background fluorescence is shown. In graph II, heterogeneous uptake is seen, with most cells exhibiting significant uptake (i.e., high uptake cells) and a fraction of cells with low signal (low/no uptake cells). In graph III, a larger fraction of the cells exhibit high uptake and, finally, in graph IV almost all cells exhibit high uptake. Note that these data only include viable cells and do not account for the fact that viability was lower for the cells shown in graph IV.

These data are interesting because they suggest a threshold phenomenon, where cells either have high uptake (i.e., the population of cells on the right side of each graph) or they have low/no uptake (i.e., the population of cells on the left side of each graph). We do not see a broad distribution of uptake levels in these graphs. This finding is consistent with previous observations in the context of intracellular delivery by acoustic cavitation and by electroporation [45, 50].

The three laser-irradiation conditions shown in Fig. 6.2B have increasing laser fluence that is compensated for by decreasing irradiation time to keep the total fraction of cells affected by the exposure approximately constant (i.e., the sum of cells with intracellular uptake and nonviable cells). However, at higher laser fluence, there were more cells with high uptake (Fig. 6.2C). Combined, these observations suggest that at the three conditions studied, the same fraction of cells experienced permeabilizing effects of laser-activated CB

nanoparticles, but the effects on the cell were stronger at higher laser fluence, resulting in more molecules delivered into each affected cell.

6.4 *siRNA Delivery and Knockdown*

The next step was to assess delivery of anti-EGFR siRNA to see siRNA uptake and knock-down of EGFR. Anti-EGFR siRNA or a negative-control (NC) siRNA were added to ovarian cell suspensions with 25 mg/l CB nanoparticles and either laser-irradiated (19 mJ/cm² for 7 min) or not exposed to laser (sham). Some samples were alternatively exposed to laser without the presence of CB nanoparticles. After 24 h post-exposure incubation, cellular RNA was isolated and then analyzed for siRNA uptake and for EGFR knockdown by quantitative polymerase chain reaction (PCR) assays. Intracellular glyceraldehyde 3-phosphate dehydrogenase (GAPDH) was used as an internal control against which RNA levels were normalized. To assess siRNA uptake, cells were laser-irradiated in the presence of anti-EGFR siRNA with CB nanoparticles (experimental group), anti-EGFR siRNA without CB nanoparticles (negative control) or NC siRNA with CB nanoparticles (negative control). There was no statistical difference (Students t-test, $p > 0.05$) in normalized anti-EGFR siRNA signal between the two negative controls (Fig. 6.3A). However, there was significantly higher anti-EGFR siRNA signal in the experimental group (2-tailed t-test with Welch's correction, $p < 0.001$) compared to either of the negative controls. The fold change of normalized anti-EGFR siRNA signal of the experimental group compared to the no-CB negative control was 12,000 and compared to the NC-siRNA negative control was 360.

As a positive control, we delivered anti-EGFR siRNA to ovarian cancer cells using a commercial transfection agent, Lipofectamine 2000. This delivery method also showed significantly higher intracellular delivery of anti-EGFR siRNA compared to NC-siRNA negative control (Fig C.4A in SI), which provides a further validation of the assay works. While delivery using this lipid-based method was effective, our photoacoustic approach has the advantage of potential use in vivo, whereas Lipofectamine 2000 is only for in vitro use.

Visual inspection of cells 24 h post treatment (Fig. C.3 in SI) revealed confluence in the no-CB negative control samples, but there was lesser cell density in the experimental group

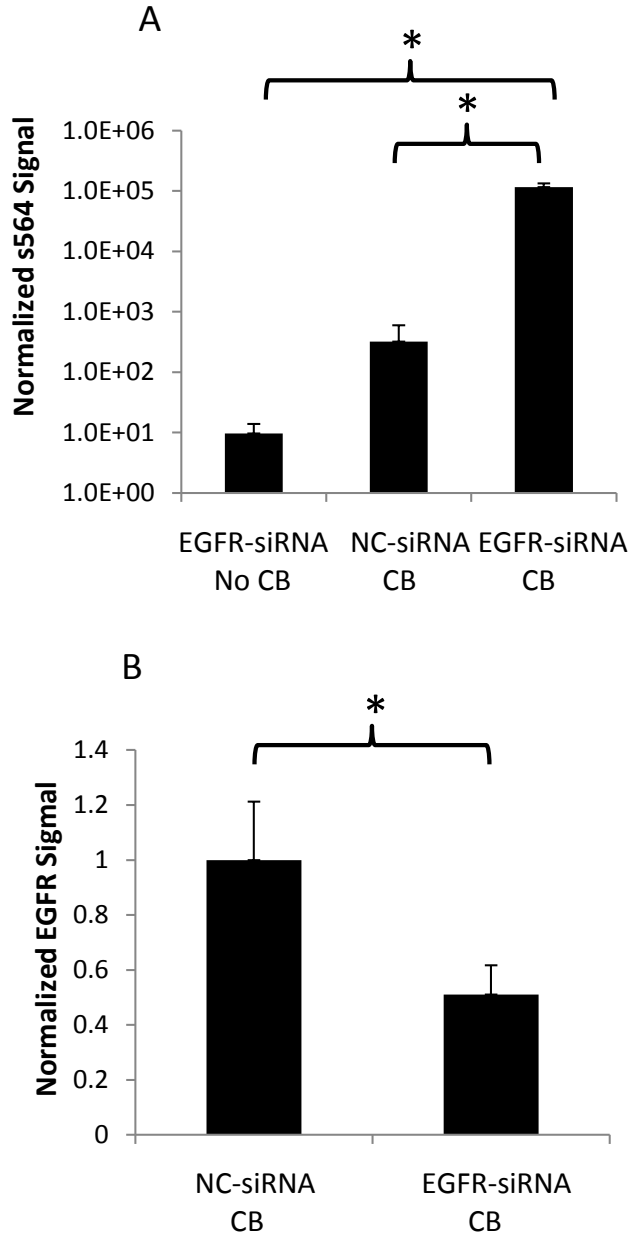


Figure 6.3: Uptake of anti-EGFR siRNA (s564) and knockdown efficiency of EGFR mRNA after photoacoustic delivery in ovarian cancer cells. (A) Amount of intracellular siRNA (s564) (in arbitrary units) normalized per 10 ng of total RNA, quantified using qPCR, when Hey A8-F8 cells with anti-EGFR siRNA or NC siRNA were exposed to laser at 19 mJ/cm² for 7 min in the presence (CB) or absence (no CB) of 25 mg/l CB nanoparticles. (B) EGFR mRNA level normalized relative to GAPDH level measured using qPCR showing knockdown when cells were exposed to laser with CB nanoparticles with, anti-EGFR siRNA compared with NC-siRNA. Asterisk symbol (*) shows statistically significant differences in uptake and knockdown (p < 0.05). Data show mean \pm SD (N = 3).

and NC-siRNA negative control samples both of which were exposed to laser irradiation in the presence of CB nanoparticles, indicated some loss of cell viability consistent with the dextran-uptake experiments (Fig. 6.2B).

Encouraged by evidence of intracellular delivery of siRNA, we finally assessed knockdown of EGFR mRNA compared to the negative control that was laser-irradiated with CB nanoparticles and NC-siRNA. The mean knockdown was approximately 49%, which was significantly lower than the negative control (Students t-test, $p < 0.05$). There was also knockdown of EGFR mRNA in positive control cells exposed to anti-EGFR siRNA with Lipofectamine 2000 (Fig. C.4B in SI). This result is consistent with the central question of this study concerning the ability of our photoacoustic method to deliver siRNA into ovarian cancer cells to knock down protein expression.

Fifty four percent of cells took up dextran at the conditions used in the siRNA experiment (Fig. 6.3B). If we assume that a similar percentage took up siRNA uptake and we assume that the degree of EGFR knockdown was the same in each affected cell, then 49% knockdown of EGFR mRNA (Fig. 6.3B) corresponds to approximately 90% of cells with siRNA uptake exhibiting knockdown (i.e., $49\% / 54\% = 91\%$). In other words, most cells that had siRNA uptake had knockdown. This indicated not only that our photoacoustic method efficiently delivered siRNA into ovarian cancer cells, but that functionally intact siRNA was delivered, and it was delivered into a cellular compartment (i.e., cytosol) that allowed it to silence protein expression.

6.5 Conclusion

This study showed for the first time that laser-activated CB nanoparticles enabled intracellular delivery of siRNA and knockdown of its target EGFR mRNA. Initial experiments showed that CB nanoparticles generated photoacoustic emission upon NIR irradiation and intracellular delivery of dextran molecules into viable cells. Photoacoustic delivery of siRNA into ovarian cancer cells resulted in 12,000 times higher normalized EGFR-siRNA signal compared to negative control cells, indicating dramatically increased uptake of siRNA molecules. This led to 49% knockdown of EGFR mRNA levels. We conclude that delivery

of siRNA to ovarian cancer cells using laser-activated carbon nanoparticles is a promising method of intracellular delivery with future possible uses in siRNA-based treatments.

CHAPTER VII

DISCUSSION AND CONCLUSION

With recent advances in biomedical research and pharmaceuticals, more focus is being put on targeted drug delivery techniques [7, 8]. Targeted delivery ensures that there is no excess dosage or exposure of healthy tissues to the drug. Most of the drawbacks associated with conventional drug delivery can be overcome by improving drug localization, targeting, and entry into the specific cell or tissue of interest. These advances in drug delivery can help minimize the required dosages and side effects and thus can also improve the efficacy of even currently used drugs.

While there are several approaches to achieve intracellular drug delivery, physical methods like ultrasound and electroporation use physical force to disrupt the cell membrane to deliver drug molecules directly into the cells. These methods are attractive because of their relative non-specificity to cell type and drug type. They create transient pores in the cell membrane which allow drug molecules to enter the cell through passive diffusion or electrophoresis. A direct intracytoplasmic delivery occurs by bypassing the endocytotic pathway thereby avoiding the issue of lysosomal degradation. However the major challenge associated with these techniques is controlling the pore size/ size of wound created by the physical force. Controlling the pore size is important because if the pore size is too small the drug molecules will not be able to enter the cell. On the other hand, too large a pore can lead to cell death. A good control over the physical force is required to control the pore size but because of the complex nature of tissues in the body it is hard to control the nature of the physical force both spatially and temporally. Our solution to the problem of controlling the physical force and pore size was the use of photo-acoustic delivery using CB nanoparticles and nanosecond laser. Our study with the nanosecond laser and CB was driven by the initial success we had with the study using the femtosecond laser [229]. Even though the femtosecond laser is more efficient in heating the nanoparticles which implies more efficient

drug delivery, it is expensive, complicated to use, and is not widely available. A nanosecond laser on the other hand is already used clinically. It is also relatively cheap and easy to use. We had flexibility in our choice of the wavelength of laser pulses because CB absorbs well across a wide range of wavelengths (300 nm to 1100 nm). Our choice of 1064 nm as the wavelength was driven by the fact that our body's primary absorptive materials (tissue, water, and hemoglobin) have a relatively high transmittance to this wavelength. This way the CB would preferentially absorb the laser while the rest of the tissue would remain relatively inert to the exposure. The method has some intrinsic advantages compared to its counterparts in physical method of intracellular drug delivery, such as: i) The source of physical force, i.e. the CB particles, is situated in the vicinity of the target cells and thereby provides more localized effect ii) The temporal nature of the force can be controlled with CB concentration and laser intensity. iii) There are more parameters, external (intensity, time of exposure) and local near the cells (CB concentration, additive addition), which can be varied to get a better control on the drug delivery. Encouraged by our initial femtosecond results and potential advantages of our method, we proceeded to test this technique on cells.

Our first goal was to test the hypothesis that exposing cells in the presence of CB leads to uptake of molecules. To test the hypothesis, we exposed DU145 cells in the presence of CB at concentrations varying from 12.5 mg/l to 75 mg/l to nanosecond laser pulses at fluences between 18.75 mJ/cm² and 200 mJ/cm² for 10 s to 7 minutes exposure times. We used calcein as our uptake marker. Visually, green cells were observed, which not only showed uptake but also proved that the calcein molecules were all over the cytoplasm and not just localized in one part of the cell. When cells were counted using a flow cytometer to quantify uptake and viability, it was observed that initially with increasing laser fluence uptake increases whereas viability decreases. Beyond a certain threshold, increasing laser fluence had no observable effect on uptake and viability. Increasing the time of exposure had two kinds of effect: below certain laser intensity, increase in uptake was observed with no apparent loss in viability, whereas beyond the threshold, the viability and uptake increased initially but then decreased in a continuous fashion. Increasing CB concentration resulted in initial increase of uptake and viability and then a continuous decrease. In other words,

parameters like fluence and time of exposure had strong correlation with final uptake and viability. Whereas the effect of fluence saturated beyond a certain threshold, increasing CB concentration and time exposure had a stronger effect on the cells leading to increased deaths. Under optimal condition, there was about 88% uptake of calcein with almost no loss of viability. It was also shown that the laser exposure to cells without CB results in less than 15% uptake even at a strong fluence 200 mJ/cm². The CB without laser exposure also did not result in any significant uptake. Adding calcein immediately after the exposure caused less than 10% uptake of calcein which meant that the pores close faster than ultrasound induced or electroporation induced pores [240, 241]. We also demonstrated uptake using two different cells lines (DU145 and H9c2), two different types of CB nanoparticles (India ink and normal CB suspension), and various uptake markers with increasing molecular weights (calcein and dextrans, 10 kDa to 500 kDa range). All of the combinations had comparable efficacies except the uptake of larger molecules (>150 kDa) which was markedly lower than the small molecules. This indicates that the technique can be used across various cell lines and drug types with some restrictions in drug size.

Cell death was observed under more intensive laser conditions both because of necrosis (suggested by red cells in microscope images and a separate population in flow scatter plots) and fragmentation (suggested by fewer cell events compared to sham for similar volume of cells analyzed in flow cytometer). Adding additives like BAPTA-AM, Ca²⁺ ions, and ATP to enhance the repair mechanism did not result in increased viability. We hypothesize that this is either because the timescales of damage are too fast that there is no time to recover or the damage was too great to be recovered. In either case, enhancing the active repair mechanism of the cell did not help. So we added an external agent like poloxamer F-68 and F-127 which prevented shearing of cells either by mitigating the acoustic waves or by plugging pores on the cells immediately as they formed. This resulted in significant increase of viability but did not compromise the uptake efficiency. Adding glycine betaine (a thermoprotectant) should have helped if there was a thermal damage to the cells, but that was not the case. So we have reasonable confidence to believe that the damage is mechanical. We believe, by controlling laser fluence, CB concentration, time of exposure,

and finally pluronic concentration, a high uptake with high viability can be achieved in various cell lines in vitro and in vivo.

The photo-acoustic effect can be broadly divided into two parts. The first is transduction of laser energy into heat, vapor bubbles, and pressure waves, and second is the interaction of pressure waves and vapor bubble with the cell which transiently porate the cells and cause uptake of molecules. After showing good efficacy with DU145 cells and calcein and comparable results with other cell lines, nanoparticles and uptake molecules, our next goal was to understand the underlying mechanism of the first stage, i.e., production of the physical force and its nature. We demonstrated that CB absorbs the laser much more efficiently than surrounding water. A suspension with less than 1% v/v CB showed significant temperature rise compared to pure DI water. It was shown through timescale measurements and acoustic data that each pulse is independent of each other, i.e., the CB goes back to its original state after each pulse and the process repeats. By measuring the bulk temperature rise it was possible to calculate the peak nanoparticle temperature. It was verified through Mie theory and absorbance measured using power meter. At 44 mJ/cm² fluence, the estimated temperature rise was about 1000°C which possibly occurs in about 10 ns. This is a really fast heating step and only pulsed lasers like femtosecond and nanosecond lasers are capable of doing that. We also devised a way to measure the acoustic output of the system without letting too much noise interfere the system. We then characterized acoustic output as a function of laser fluence, CB concentration, and distance from source. We concluded that increasing all the parameters resulted in increased acoustic output.

The possible ways of production of pressure waves from laser CB irradiation were narrowed to thermal expansion, vaporization, and carbon steam reaction. In the fluence range that we used, we eliminated the possibility of carbon steam reaction playing role in the bioeffects by demonstrating the presence of pressure waves when water was replaced with pure acetic acid. In fact, for same concentration and fluence, acetic acid had a higher output than water. This, along with non-linear rise of peak pressure with fluence, led us to believe the final acoustic pressure waves are produced as a combination of thermal expansion and vaporization.

There were two competing hypotheses about the nature of the physical force causing the poration: the first was the pressure waves interacting with the cell membrane and the second was the vapor bubble formed during the heating of the nanoparticle. In order to distinguish between the two, we devised an experiment where we physically separated the nanoparticles from the cells and uptake marker by about 50 μm and found that there was no delivery of molecules. We chose a separation distance that was not enough to cause a significant attenuation of the pressure waves. We therefore concluded that there is a strong possibility that a physical interaction between vapor bubble and cell causes the intracellular delivery. This is a very near field effect and also addresses the discrepancy between the observed saturation with increasing fluence and no saturation with increasing CB concentration. We believe that this is because when fluence is increased, it heats the particle more creating bigger vapor bubbles. The increment in radius is, however, less and less as fluence is increased, because the increment is proportional to the cube root of fluence. Therefore beyond certain fluence the probability of encountering a cell does not change significantly. Whereas, when CB concentration is increased, the number of nucleation sites for vapor bubble formation increases which increases the probability of vapor bubble - cell interaction. We then applied the method for delivery of a therapeutic molecule. We chose siRNA as one our molecule because of its size (~ 13 kDa) and its intra-cytoplasmic target, both of which fit well for the method that we developed. We chose to knockdown EGFR in ovarian cancer cells as proof of concept because the cell line and the target were well understood. To determine the conditions of laser fluence, CB concentration, and time of exposure, we chose the 3 most optimal parameters from the DU145 study. We used FITC-dextran (70 kDa) as a model uptake marker which is a good representation of the size of siRNA. They all performed similarly and we picked the mildest condition to ensure good viability 24 h post irradiation. We showed that there was significant intracellular uptake of siRNA and 49% knockdown of EGFR. This is the first proof of concept and we expect a better efficiency with more optimization of conditions.

The final objective of this project was in vivo demonstration of our method (see Appendix for more details). We demonstrated PI uptake in TA muscles of mice. A simple injection of CB suspension with propidium iodide followed by laser irradiation at 200 mJ/cm^2 for 2 minute resulted in uptake of 30%, but we did not know if this uptake occurred in viable or nonviable cells. The main challenge was to achieve a uniform spreading of CB in the entire tissue. Unfortunately, CB concentrated around the injection site with little or no spreading. Post irradiation, the mice were sacrificed after 2 days and 7 days to observe the muscle recovery from damage. It was seen that the muscle damage persisted even after 7 days. While this indicates that our method is doing something to the tissue, significant improvements need to be made to CB particles and optimization of the laser fluence and exposure time.

In summary we investigated: i) a novel method for intracellular drug delivery that can achieve high efficiency in vitro; ii) the reasons for cell death and possible ways to protect the cells from permanent damage; iii) a way to optimize the parameters to ensure maximal uptake with minimum loss of viability; iv) the underlying mechanism and nature of the physical force that causes membrane disruption; v) the possibility of the use of this method in siRNA delivery; and vi) possible in-vivo applications.

We believe this study will lead to a new paradigm in exploiting laser-material interaction for targeted intracellular drug delivery. In this study we demonstrated that other materials like MWCNT and SWCNT can generate acoustic waves similar to CB. We also demonstrated intracellular drug delivery using India ink. With more investigation we hope there will be newer materials discovered with even higher drug delivery efficiency. Exploiting laser particle interaction to achieve intracellular drug delivery has been around for quite some time now. Most of these techniques prefer gold as their laser absorptive media. The gold needs to be either internalized or at least attached to the cell surface in order for the drug delivery to occur [99, 230]. The nanoparticle also needs to be modified to bind to the cell membrane. The drug delivery occurs through heating of the nanoparticles which causes thermal damage. These methods are therefore significantly slower, complicated, and in most cases require higher laser energy. The system we developed takes advantage of

mechanical damage which can be caused from a greater distance and therefore no binding to cell surface is necessary. This also bypasses the incubation step which is required for gold based technique for cell surface binding, making it faster. CB is also cheap and abundantly available and there is no particle modification required making it a simpler protocol to follow. However, more study needs to be done in order to find particles which can perform better than CB. There is also a potential of using an implantable biomaterial made of CB entrapping the drug within it that is released only when irradiated with nanosecond pulsed laser. This would lead not only to controlled release but also poration of surrounding tissue and more efficient delivery of the drug.

Apart from intracellular drug delivery, this method also has a potential application in tattoo removal. The potential use of lasers for tattoo removal was shown back in 1963 [242]. In more recent years, the Q-switched laser has become the preferred method of tattoo removal because of efficient removal with minimal side effects [243]. The mechanism underlying the removal of tattoo using short laser pulses is photoacoustic material breakdown. Although Q-switched lasers have been shown to be highly effective in tattoo removal, they are not without adverse effects. Acute events include purpura, crusting, blistering, infection, and oxidative darkening of pigment [244]. The current study can provide some insights into improving the technique and minimizing side effects. For example, adding polaxomers during tattoo removal might save some cells from being damaged while the laser ablation of tattoo occurs. We now know that poration of cells occurs during laser ablation of CB. So, while the tattoo is being removed doctors can take the opportunity to deliver drugs during tattoo removal either to minimize side effect or for other medications.

Another use of this technique might be in the field of photodynamic therapy (PDT). Currently, most PDT absorptive media are molecules called photosensitizers that absorb laser and generate oxidative species destroying cells. From our current study we know that when the time of exposure or particle concentration is increased, more destruction of cells occurs. We can take advantage of that fact and use CB nanoparticles that migrate towards tumor through EPR effect (200 nm is a good size for that) or decorate the nanoparticles with ligands so that they specifically target tumors. The advantage of this method would

be once the particles are injected into the tumor they should remain there for longer period of time than normal PDT photosensitizer molecules and can be used for multiple exposures without the need of multiple injections. Since there is no generation of reactive oxygen species, the toxicity associated with PDT can be avoided.

The most common application of photo-acoustics in biomedical engineering is imaging wherein nanoparticles are injected and tracked using laser light from the acoustic feedback. The most common particle used is gold but from this study we propose the use of CB, nanotubes, and other forms of carbon. The current study not only allows us to track particles from the acoustic output but it can also be potentially calibrated to know the depth of nanoparticles and changes in the surrounding tissue which can indicate migration from one tissue to other, crossing of some barrier, etc. Another form of carbon called carbon dots (C-dots) are being used as imaging substitutes for quantum dots because of its non-toxic nature. C-dots are extremely small CB particles (<1 nm) and there is a strong possibility that these particles will also cause intracellular drug delivery if exposed to nanosecond laser pulses. If we conjugate them with a payload, then these particles can be tracked using fluorescence and/or photo-acoustics, and then when they reach the proper target, they can deliver their payload.

Microsurgery with laser has been around for quite a while now. The use of LASIK to correct vision was one of the revolutions in modern surgery. Since then techniques like photorefractive keratectomy [245], laser endarterectomy [246], and endoscopic laser lithotripsy [247] have been popularly used to surgically treat various part of the body. Currently very fine surgery like transoral surgery is also being performed to treat throat cancer [248]. With our current technique fine surgeries can be done in a more convenient manner because the destructive effect on cells only occur where both the CB nanoparticle and the laser is present. If we can clearly label our target area with CB then we do not need to worry about the destruction of healthy tissue. The use of CB will also result in the use of lower fluences to achieve similar effect.

7.1 *Contribution*

Overall this thesis progresses the field of drug delivery and biotechnology in several ways: i) it demonstrates a way to achieve efficient intracellular drug delivery across several cell types and delivery molecule type; ii) it helps us understand the nature of cell damage and possible ways to counter the effect which can potentially be used in other damage related studies; iii) it provides insights about mechanism of generation of pressure waves through laser irradiation of CB nanoparticles which can not only be used in drug delivery but in other applications as well; iv) it demonstrates delivery of siRNA which opens up possibility of therapeutic use of this technique; v) it promises to have an in-vivo applications in the future with proper design and optimization; and vi) it lays foundation for designing new materials for laser particle interaction to achieve controlled damage or acoustic signals.

The use of CB in medicine has so far been limited to tattoos, vascular labeling [249, 250], phagocytic labeling agent [251], imaging [91], and in studies of pollution induced toxicity in lungs [252]. We identified a novel application for this easily available nanomaterial with very little structural or functional modification. The study uniquely integrates advanced laser technology and nanoscience in the context of drug delivery by exploiting an aspect of laser-nanoparticle interaction that had almost never been used for drug delivery. Even though the main focus of this thesis is drug delivery, the physical science of acoustic wave generation can be applied to various other fields. The technique also has promising minimally-invasive, targeted in-vivo drug delivery applications. It lays the foundation for new medical devices capable of performing intracellular drug delivery efficiently.

CHAPTER VIII

RECOMMENDATIONS

8.1 Nanoparticles

A fundamental component of this intracellular delivery technique is the nanoparticles, which are used to preferentially absorb the laser energy. The nanoparticle mostly used in this study was the CB, which was prepared through sonication of the CB powder in DI water followed by addition of a stabilizing surfactant. DLS measurements revealed a Gaussian distribution in size with a dispersity of around 0.21. For good monodispersed nanoparticle formulations, the dispersity is below 0.1 [253]. I recommend a study that focuses on achieving monodispersed CB suspension and scientific way to control the size which will help understand the effect of size on acoustic output. This will also be very useful in future in-vivo applications where clearance of nanoparticles is a concern. One possible way to do it is through centrifugation and selective filtering: first big particles are centrifuged out following sonication and next the samples are passed through progressively finer filters to get a desired cut-off in size. Another more sophisticated method is to use Field Flow Fractionation (FFF) which will separate into any given size range (Instrument: Eclipse DUALTEC, Wyatt Technology).

Apart from just controlling the size, it might be worthwhile to look into functionalizing the CB nanoparticle surface with cyclic RGD[254], CRGDK[141] so that it can be better targeted into tumors. It can also be PEGylated for creating stealth nanoparticles that can be used in systemic delivery with higher residence times in the blood stream.

In this study apart from CB nanoparticles, other nanoparticles such as SWCNT, MWCNT, and India ink have been used, all of which are some form of carbon. I recommend pursuing further with the search for new nanoparticles. The design of new nanoparticles will be guided by both its size and its behavior when exposed to laser. Keeping in mind future in-vivo applications, a nanoparticle should be small enough to diffuse through tissue and get cleared easily (<150 nm [255]). However, there is a restriction on the minimum

size as well. Our hypotheses for acoustic wave generation are primarily thermal expansion and vapor formation. For that, the size of the nanoparticle should be big enough for it to absorb significant part of the laser light to get hot. However, smaller size means better heat transfer to surroundings. Therefore, the problem can be bound by determining the minimum size required for the particle to get heated faster than losing heat to the surroundings. Material properties like laser absorption efficiency, thermal conductivity, scattering efficiency, melting point, thermal expansion coefficient, and bulk modulus also play a role in this. We would want our particles to have high laser absorption efficiency (ideally at wide range of wavelengths), low thermal conductivity (to retain the heat and get hot), less scattering (for more absorption, the shape, size, and surface roughness also plays a role), high melting point (so that high temperatures can be reached without changing the shape of the material permanently), and low bulk modulus with high thermal expansion coefficient (such that more particle surface acceleration occurs for the same temperature rise). For CB the minimum size chosen can be as low as 25 nm, at which point the time scales for heat deposition would be the same as time scales heat transfer rate to the surrounding. But we have to careful because the melting point of particles also decreases dramatically with size [239].

Possible candidates for future nanomaterials can be gold nanorods [256], gold nanoshells [257], gold nanocages [258], and silica nanoparticles, Polymeric nanoparticles can also be tested for acoustic output and intracellular drug delivery. I also suggest studying SWCNT and MWCNT for their efficiency in drug delivery. We have already tested that under the same absorbance of light SWCNT generates a significantly higher acoustic output so it is a more efficient converter of heat to sound. It might be an interesting study to see how well it performs in drug delivery.

With regards to the type of carbon particles, I recommend the use extremely small CB particles called carbon dots (C-dots) [91] as laser absorbers. They are used for particle tracking and imaging but might also possess the capability of intracellular drug delivery under the influence of laser. I recommend pursuing a characterization study with C-dots. This also holds the potential of integrating an imaging technique with a drug delivery

technique using the same material, though they might be too small to be heated up to the right temperatures.

A common problem with the current CB nanoparticles is its inability to get cleared from tissues even after 7 days. One way to solve this would be to coat the carbon over polymeric particles. The laser irradiation can break the polymer and disperse the smaller CB particles in the tissue leading to better clearing than using just one big CB particle. For example we can use the C-dots and coat them over PLA/PLGA particles. After irradiation the C-dots will eventually get cleared and PLA/PLGA will slowly degrade.

8.2 System Characterization

In this thesis we have performed a series of characterization experiments to understand the system thoroughly and we believe that we have some understanding of the system. But there is still room for more experiments. I recommend studying the laser beam profile as the first thing to do. A primary reason for error in laser CB drug delivery was caused by non-uniform beam profile. Ideally we want a very uniform beam profile but unfortunately in most of our experiments we encountered diffraction rings, dead spots, and bright spots which resulted in temporally non-uniform exposure of sample. One way to address the problem is to use a top-hat output laser rather than a Gaussian output laser which can be done by replacing the internal mirrors of the current lasers or using a beam profiler.

The other important thing that needs to be done is the study of long term viability and uptake of the system. So far we have only quantified uptake and viability immediately after the laser exposure. For intracellular delivery of therapeutics like siRNA, mRNA cells are required to be incubated for some time post treatment. Therefore it might be a good idea to characterize the system through uptake and viability measurements 24 h and 48 h post treatment to see not just necrotic death but also apoptotic death.

Another issue with regards to measuring uptake is that, so far, we only count the number of cells that have a certain amount of fluorescence. That is not the only way to quantify uptake. For example, one could calculate how many molecules actually went in each cell as a function of exposure parameters. Similar studies have been done in the past for ultrasound

exposure and from those measurements the increase in cell permeability can be numerically calculated [259].

We demonstrated that poloxamer F-127 was efficient in mitigating the damaging effect of laser CB interaction at intense conditions. It would be worth doing a control experiment using less intense conditions and evaluate effectiveness of F-127.

8.3 Understanding Hypothesis

The mechanism of intracellular drug delivery through laser particle interaction can be divided broadly into two parts. The first being the energy transduction from laser to creation of acoustic waves and the second is the interaction of the physical force generated through laser CB interaction with the cell leading to reorganization of the cell membrane and pore formation followed by drug uptake and recovery. One of the highlights of this thesis is that we made some progress in the first part of the problem, i.e. understanding the mechanism of acoustic pressure generation from laser irradiation of CB nanoparticles. We have characterized the system by varying few important parameters like fluence and CB concentration and demonstrated their relationship with the pressure output. We also predicted peak particle temperature, bubble radius, etc. Our broad conclusions were that the acoustic output is caused by mainly three pathways viz. thermal expansion, vapor formation, and/or reaction of CB with steam. The three phenomena are not independent from each other and the final outcome is a sum total of all of the effects making it a very complicated system. But even so, there might be ways to separate them from one another.

For that, I recommend, finite element modeling (FEM) of the system such that whenever laser fluence, pulse width, and particle concentration are known, spatial and temporal profiles of particle temperature, pressure, bulk pressure, bubble radius can be calculated [260]. This will help us in two ways: first we can establish the relationship between the input conditions like fluence, material properties, laser properties etc. to the final outcome of pressure and bubble formation which will help us in determining the most important factors that decide the outcome of the system in terms of bioeffects. This will give us an idea about what material properties are needed to get maximal efficacy when designing new

nanoparticles. Secondly to test the current hypothesis of pressure generation, one can find the laser fluence threshold where vapor starts just forming and use fluences below that to study the effect of just thermal expansion on intracellular drug delivery. Another way to determine the threshold fluence experimentally would be to plot laser fluences vs. peak pressure. If the relationship is linear then thermal expansion is the mechanism and if it is non-linear then vapor formation has begun [84]. The data generated so far indicates that the fluences we tested do not produce enough reaction of CB with water. This, however, does not mean that there might not be reaction at higher fluences, but separating it out from the other phenomena would be difficult because for reaction, vapor formation is a must. But at higher fluences we expect reaction to occur and the way to show the existence of the reaction is to either see consumption of nanoparticles or actually measure the change in headspace gases through real time gas chromatography. If the products formed are CO and H₂ then performing real time GC is a must because H₂ escapes from the system very fast. Even though the acoustic output of the irradiated particles is an indication of the effect, it might be that the cell interaction with the vapor bubble formed during laser irradiation of CB is the real cause of delivery. If that is true, then we can test the hypothesis by reducing the fluence to the bare minimum such that there is a little vapor formation and then increase the CB concentration to get the maximal use of laser energy. Incidentally, our optimal condition is a very low fluence with longer time of exposure. This rationale can be extended to other cell lines to achieve optimal delivery conditions.

One of the hypotheses proposed in this thesis is that the vapor bubble interaction might be necessary for cellular impact. Some experiments in this thesis are presented as a proof of that hypothesis but further testing needs to be done. For that I recommend building a chamber where the spatial profile of pressure can be controlled. This can be achieved through a series of pressure transducers radially positioned and calibrated to have a net resultant effect. When cells are placed in this chamber, we can simulate a pressure profile similar to the one that is created during laser irradiation but without the formation of vapor bubbles. If indeed the acoustic waves are responsible for drug delivery we should be able to see uptake and death similar to laser irradiation in this case as well. But, if there is

no delivery, we can almost be certain that the acoustic waves do not, by themselves, cause uptake of molecules.

Another interesting and important thing to do next would be the study of cell deformation as a result of laser particle interaction. To do that, I recommend, building a live imaging system that consists of a microscope mounted on a fast video camera, capturing frames at quick succession between each pulse. If a big cell like oocyte is chosen it would be easier to observe the cell membrane deformation with proper labeling of the membrane. It might also be a good idea to track the fluorescent molecule during the laser exposure to see the transport of the molecule across the cell membrane. A key thing that can be learnt from this study is how does the nature of the cell (size, Youngs modulus of cell membrane, etc.) play a role in the final outcome of the process. A major hurdle in building this system with high temporal and spatial resolution will be lighting the system and I recommend using the nanosecond laser itself as a lighting source because of its high peak output.

8.4 siRNA Delivery

In this work, we have shown a proof of concept of EGFR knockdown in ovarian cancer cells in vitro. We did not optimize the system for knockdown and yet were able to achieve 49% EGFR knockdown. We believe if we optimize the laser input conditions we can do even better. This opens up a whole new avenue to do more work. The first thing would be to optimize laser exposure conditions to achieve maximum knockdown with minimum loss of viability. We believe that this technique is relatively non-specific to the type of delivery molecule used, so it should perform similarly across various siRNAs. Other targets like herpes simplex virus (HSV-2) associated viral proteins UL27 and UL29, human papillomavirus oncogenes (HPV E6/E7), etc. can be chosen which might have more clinical relevance [207]. One can also theoretically extend the technique to deliver other interesting molecule like shRNA, mRNA, proteins, ZFNs and TALENs.

8.5 Characterization in-vivo

We have demonstrated proof of concept in-vivo delivery of PI in TA muscle cells, but we realized that muscle might not be the best target spot for laser irradiation study. Since

the muscle cells are very long and this method creates only localized pores, the effect was not observed across the length of the muscle cell. The inflammation response is also very complicated in muscle cells making it hard to track the effect of laser CB interaction in-vivo. A good choice of tissue might be skin because it is easy to target, extract, and perform analysis on. Another big issue is particle size. The current CB particle hardly shows any diffusion, and therefore, I recommend pursuing the nanoparticle study recommendation first before the in-vivo studies. Once the nanoparticle issues and target has been fixed, laser parameters can be varied. There is a possibility that in future therapeutics can be delivered in-vivo. For example EGFR or HER2 siRNA can be delivered into ovarian cancer tumors and knockdown can be measured along with tumor size reduction studies.

APPENDIX A

IN-VIVO STUDIES

The delivery of large molecules and therapeutic drugs is a challenging task due to the barrier of the plasma membrane. One approach to facilitate the delivery of a variety of large molecule drugs, while mitigating membrane selectivity, is to induce transient pores in the cellular membranes.

It has been observed that carbon black nanoparticles (CB), when struck with nanosecond pulsed lasers, create photoacoustic effects which can potentially be used to induce these transient pores. It has been already determined in an in vitro study that such a phenomenon has made delivery of macromolecular drugs into cells possible.

This study now aims to assess the implications of the photoacoustic effects on in vivo intracellular drug delivery. The first steps of the study have been to observe and assess the delivery of a fluorescent viability marker drug, propidium iodide (PI), in murine tibialis anterior (TA) muscles. Muscle samples, when injected with 100 μ M solutions of propidium iodide (PI) and 0.4 g/l CB and exposed to a 200 mJ/cm² power nanosecond pulsed laser, exhibited significantly compromised cell membranes. This showed enhanced uptake of PI compared to non-exposed controls. However there is the possibility of other variables such as potential cell damage, the range and resulting effects of intramuscular CB distribution the process, and the clearance of PI (or any other drug in question).

A.1 Methods

A.1.1 Nanoparticle Preparation

To prepare the CB nanoparticle solution, 20 mg of CB (Black Pearls 470, Cabot, Boston, MA) was added to 50 ml of 0.013% (v/v) Tween 80 (Sigma-Aldrich, St. Louis, MO; added to reduce aggregation and settling of the nanoparticles) in DI water and sonicated for at least 15 min to obtain the final CB solution at a concentration of 0.4 mg/l. The

size of the individual CB nanoparticles was 25 nm, but they were aggregated into larger particles of 189.3 (± 1.5 nm ($n = 3$)) diameter with a dispersity of 0.16 (± 0.03 ($n = 3$)), as determined from dynamic light scattering measurements. After making the 50 ml solution of CB nanoparticles, it was aliquoted into smaller 1.5 ml samples.

A.1.2 Mice Preparation

Live female mice (CD1IGS) weighing approximately 22-24 g were anaesthetized first using isoflurane gas and then injected with a rodent injectable anesthetic (containing ketamine and xylazine) to keep them under anesthesia for approximately 2 hours. After that, the hair at the sites of their TA muscles was removed using the hair removal product (Nair).

A.1.3 Sample Injection

A total volume of 80 μ l containing PI at a final concentration of 100 μ M and CB at a final concentration of 400 g/l was injected into the murine TA using an insulin syringe. The syringe was injected perpendicular to the muscle to a finite depth using a special injector that could control the amount injected volume with a screw gauge. Injections were made while pulling out the syringe. At each step about 10 μ l of solution was injected. This ensured a uniform distribution along the depth of the muscle. For control experiments either the CB was replaced with DI water or the PI was replaced with DI water. Generally one leg served as control while the other was exposed. The control leg was wrapped in aluminum foil to prevent fluorescence.

A.1.4 Laser Exposure

After injections, some mouse muscles were exposed to a nanosecond pulsed laser (Continuum Surelite III) at different fluences respectively per leg. Fluences used were 100 mJ/cm² and 200 mJ/cm² per pulse and the exposure time was 2 minutes for both of these fluences. Mice samples were held still using a clamp but legs were free. The beam was aimed at the leg on the TA muscle.

A.1.5 Extraction

After exposure, mice muscles were either extracted immediately post exposure or housed for 2 days or 7 days before muscle extraction was performed. A 25 gauge needle was used to separate the muscle from the bone and cut out with small scissors. The extracted muscle is then washed in Dulbecco Phosphate-Buffered Saline (DPBS) and then lightly dried on a tissue to remove excess moisture. Then immediately picked up with tweezers and immersed in liquid nitrogen cooled Isopentane to be snap frozen. Frozen muscles are kept with dry ice in a freezer at -80°C until cryosection histology is to be performed on the tissues.

A.1.6 Sample Collection

The muscles to be sectioned were cut using a cryostat (Cryostar NX70). The cryosectioning was performed at a -28°C chamber temperature and each section taken was cut at a $20\ \mu\text{m}$ thickness. Mounting of the muscle sample for stability in cutting was done using an Optimal Cutting Temperature (OCT) compound which froze a segment of the muscle in place in the Cryostar chamber. Each muscle section was cut such that minimal OCT appeared in the sections. Sections were collected on special slides (VWR Superfrost®Plus Micro Slides). Sections were taken at a given representative point in the muscle, once the point was chosen 3 successive cuts were made a replicates for the same area as measure to avoid or identify cutting artifacts.

A.1.7 Analysis and Quantification

Extracted samples were stained with Hematoxylin and Eosin (H & E) for bright field imaging and samples were untouched for fluorescence imaging. For fluorescence imaging, sections were observed under a Carl Zeiss NLO 510 Multi-photon confocal microscope for signals of PI presence in tissues. The PI signals in a sample indicated that cells of a given tissue are compromised, whether this involves irreversible or reversible damage for PI to enter a cell. The viewing magnification was at 20x. Two image channels, a fluorescence channel and a bright field channel, were used to observe each section. The used lasers excited PI at 535 nm and there was an emission at 617 nm in the fluorescence channel. In order to

capture an image of an overall section at 20x magnification, the section was captured by an automatic tile-scan, taking an image of the sample frame by frame. Excess noise in the imaging process had to be accounted for in the fluorescence channel so that relevant the relevant PI signal was not overshadowed. As a control for fluorescence, samples with only PI injections and no exposure were imaged first. Subsequent samples that had been laser irradiated and/or had CB nanoparticle injections were then imaged using the same acquisition parameters that were used to image samples with only PI. Bright field imaging was done using bright field setting of a fluorescence microscope (Nikon E50).

A.1.8 Quantification

In order to analyze the amount of PI signal, 3 replicates of mice TA samples were used. For each mice sample at least 3 representative sections were imaged. Two quantities were calculated from each image: i) the total number of pixels having certain PI fluorescence (threshold gating) ii) the total pixels of the muscle section. For each muscle the sum of total pixels of PI was divided by the sum of total pixels of muscle. This gave us an estimate of the area that had certain PI fluorescence. This quantity was calculated for all 3 muscles samples. Values are reported as mean of the 3 samples with their standard deviation.

A.2 Results and Discussion

Fig. A.1 shows various combinations of treatments done on Murine TA. First TA muscles were injected with PI with no CB and no laser exposure which served as a control whether there is a background signal. Next, the TA muscles injected with PI were either exposed to laser at 200 mJ/cm² for 2minutes or injected with CB. Finally muscles were injected with both PI and CB and exposed to laser at 100 mJ/cm² for 2 minutes and then to laser at 200 mJ/cm² for 2 minutes. It was observed that PI by itself did not show any PI signal. There was no PI signal even under laser exposure without CB. The CB injection by itself showed some PI signal which was in fact very similar to the signal observed when the muscle was exposed to laser at 100 mJ/cm² for 2 minutes in the presence of CB. But when muscles were exposed to 200 mJ/cm² for 2 minutes brighter fluorescence was observed.

In our previous in vitro study we demonstrated that the CB or the laser by itself do

Table 1: Zero Day					
Conditions	No CB, No Exposure	CB, No Exposure	No CB, Exposure (200 mJ/cm ²)	CB, Exposure (100 mJ/cm ²)	CB, Exposure (200 mJ/cm ²)
Fluorescence					
Bright Field					

Figure A.1: Representative fluorescent and bright field images of tissue sections extracted immediately post treatment under various conditions. Fluorescence imaging shows that there is no propidium iodide signal (PI) signal when there is no carbon black (CB) in the tissue. The CB by itself without laser exposure shows a little signal whereas when laser and CB is used at 100 mJ/cm² for 2 minutes there is some signal which increases when the laser fluence is increased to 200 mJ/cm². Bright field imaging with H & E staining shows the accumulated CB and separation of muscle tissue. Scale bars are 500 μ m.

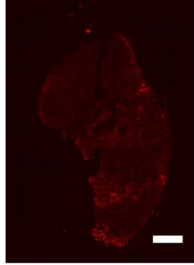
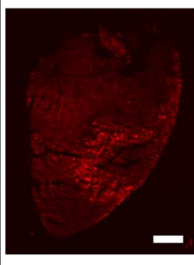
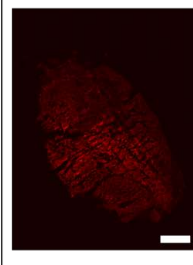
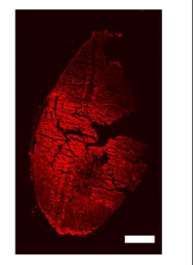
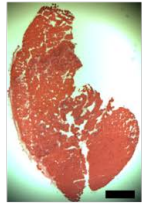
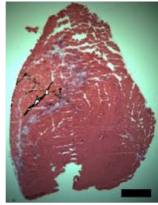
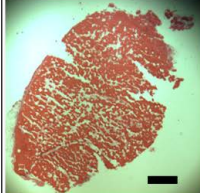
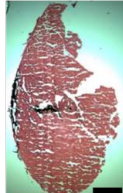
Table 2: Two Days				
Conditions	No CB, No Exposure	CB, No Exposure	No CB, Exposure (200 mJ/cm ²)	CB, Exposure (200 mJ/cm ²)
Fluorescence				
Bright Field				

Figure A.2: Representative fluorescent and bright field images of tissue sections extracted 2 days post treatment under various conditions. Fluorescence imaging shows that there is decrease in propidium iodide signal (PI) signal in the tissue with carbon black (CB) and no laser compared to immediate extraction. The laser by itself without CB does not show any sign of long term PI staining (thus signifying damage) whereas tissue exposed to 200 mJ/cm² for 2 minutes in the presence of CB still shows PI signal. Bright field imaging with H & E staining shows the accumulated CB still present even after 2 days and separation of muscle tissue. Scale bars are 500 μ m.

not affect cells, it is only under the combination of the two that results in intracellular drug delivery. To see PI fluorescence in samples with just CB was a bit odd. We did a control where we just exposed murine TA to CB without laser or PI, to find out if the CB fluoresces by itself and we found that there was no fluorescence (data not shown). Therefore, there were two hypotheses that might have resulted in PI positive samples: i) the CB is causing some sort of damage to the tissue resulting in uptake of PI ii) the CB being a non-specific absorber, absorbs the PI and fluoresces. The bright field images revealed that the CB was not diffusing across tissue, in fact it just localized around the needle track, and this may lead to formation of a CB mesoporous structure which can cause non-specific absorption of PI. When samples were analyzed for fraction of PI fluorescence area, (Fig. A.4A) it was seen that there was statistically higher fluorescence in samples with just CB compared to other controls (Students t-test, $p < 0.05$). The exposed samples both had statistically higher signal compared to laser only and no laser no CB control (Students t-test, $p < 0.05$). The 100 mJ/cm^2 for 2 minutes sample did not have a statistically higher PI signal compared to CB only sample (Students t-test, $p > 0.05$) but the sample exposed to laser had a statistically higher signal of PI than both the CB and the 100 mJ/cm^2 for 2 minutes sample (Students t-test, $p > 0.05$). But because we saw statistically higher signal with 200 mJ/cm^2 we decided to observe the muscles for longer times post irradiation.

When the muscles were extracted 2 days and 7 days post irradiation, it was observed that the signal with just the CB had gone down after 2 days and remained low after 7 days also compared to day 0 experiments (Fig. A.2 and Fig. A.3). But the sample exposed to laser at 200 mJ/cm^2 for 2 minutes retained PI signal even after 7 days and the amount of signal did not go down statistically. When analyzed numerically it was confirmed that the PI signal indeed lowered compared to day 0 in day 2 and day 7 (Students t-test, $p < 0.05$) experiments (Fig. A.4B and A.4C). This leads us to believe that the PI in the CB only sample had slowly cleared away with time. This is only possible if the PI was present in the extracellular space. This leads us to believe that the CB non-specifically absorbed the PI and therefore the fluorescence at the initial time was an artifact. When we look at the bright field images, we observe the presence of accumulated CB even after 7 days. This is

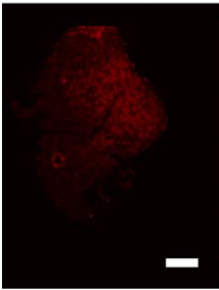
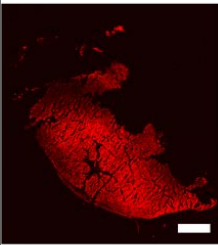
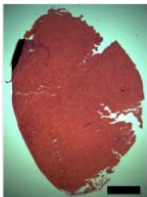
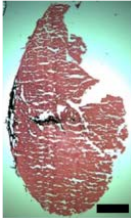
Table 3: Seven Days		
Conditions	CB, No Exposure	CB, Exposure (200 mJ/cm ²)
Fluorescence		
Bright Field		

Figure A.3: Representative fluorescent and bright field images of tissue sections extracted 7 days post treatment under various conditions. Fluorescence imaging shows that tissue exposed to 200 mJ/cm² for 2 minutes in the presence of CB still shows PI signal. Bright field imaging with H & E staining shows the accumulated CB still present even after 7 days and separation of muscle tissue. Scale bars are 500 μ m.

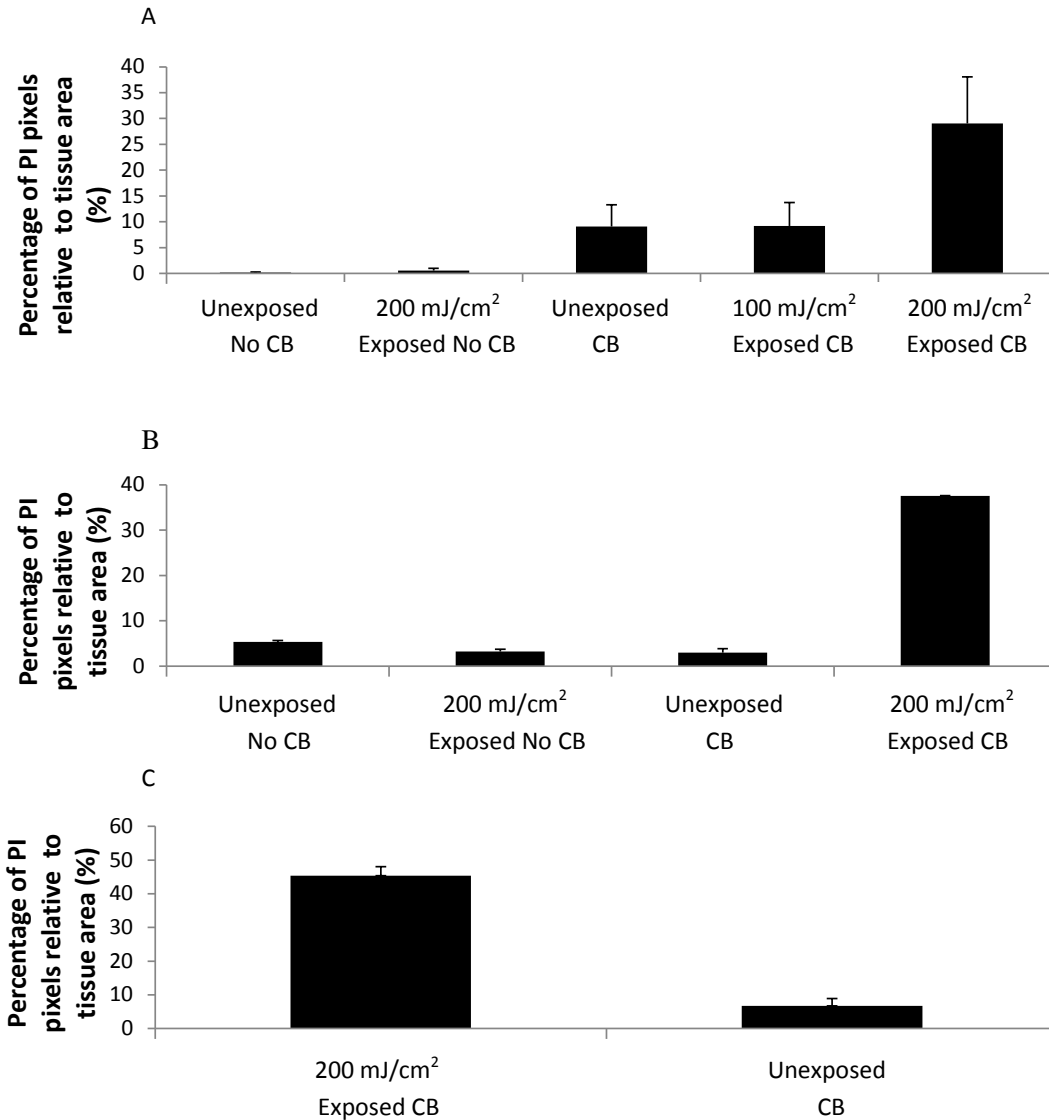


Figure A.4: Pixel of PI positive normalized to total pixel counts for analyzed tissue sections as a function of various treatment conditions at different days. Percentage of PI positive area relative to total area in the tissues under various treatment conditions when the muscle is extracted immediately after exposure (A), 2 days post exposure (B) and 7 days post exposure (C) showing PI signal in the exposed sample with CB even after seven days post treatment. Data show average \pm standard deviation (SD) ($n = 3$).

probably because CB is either too big to diffuse out and get cleared or there is some sort of charge interaction (CB has a zeta potential of -21 mV) that is preventing CB from clearing out. In either case this is concerning and needs to be taken care of in the future.

A.3 Conclusion

In this study we demonstrate uptake of PI in murine TA muscle cells when exposed to laser at 200 mJ/cm^2 for 2 minutes compared to controls. The cell still retained the PI even after 7 days post exposure. But, this process has to be further optimized to get better results and there are several concerns: i) the lack of diffusivity of CB ii) the inability for the CB to get cleared with time. We believe once those issues are solved, this technique would be a viable technique for intracellular drug delivery.

APPENDIX B

SUPPLEMENTARY INFORMATION FOR PHYSICAL MECHANISMS

B.1 Calculations

B.1.1 Uniform heating of particle

1. Temperature of particle if all the heat goes to raising the temperature of the particle

Mass of nanoparticle in the solution, $m = 25 \text{ mg/l} * 560 \text{ } \mu\text{l} = 1.4\text{e-}08 \text{ kg}$

Heat capacity, $C_p = 700 \text{ J/kg/K}$

Heat absorbed per pulse by the nanoparticles, $Q = 10.15 \text{ mJ}$

Change in temperature, $\Delta T = Q/(m * C_p) = 1000^\circ\text{C}$

2. Nanoparticle temperature rise assuming its not heat transfer limited

Rate of heat deposited on the nanoparticles = $1.015\text{e}06 \text{ W}$

Rate of heat removal because of heat transfer to the surrounding

= heat transfer coeff (h) * Surface Area (A) * temperature difference between bulk and nanoparticle (ΔT)

$$= (5.80\text{E}+06 \text{ W/m}^2/\text{K}) * (1.26\text{E-}13 \text{ m}^2) * (1000 \text{ K})$$

$$= 7.29\text{e-}04 \text{ W (for water at } 25^\circ\text{C)}$$

$$= (5.80\text{E}+06 \text{ W/m}^2/\text{K}) * (1.26\text{E-}13 \text{ m}^2) * (1000 \text{ K})$$

$$= 2.01\text{E-}12 \text{ W (for vapor at } 100^\circ\text{C)}$$

So heat removal is negligible compared to heat deposition so effectively there is no heat loss while the particle is getting hot.

B.1.2 Vapor formation

1. If all the heat went to vaporize the water

Heat required to get 1 mol CB from 23°C to 100°C

$$= (1 \text{ mol}) * (8.4 \text{ J/mol/}^\circ\text{C}) * (100^\circ\text{C} - 23^\circ\text{C})$$

$$= 646.8 \text{ J}$$

Heat required to get 1 mol of water from 23°C to 100°C

$$= (1 \text{ mol}) * (75.24 \text{ J/mol/}^\circ\text{C}) * (100^\circ\text{C} - 23^\circ\text{C})$$

$$= 5793.48 \text{ J}$$

Heat required to vaporize 1 mol of water = 2.71e+04 J

Total heat required to vaporize 1 mol of water and keep the system at 100°C = 3.36e04 J

Total heat supplied per pulse = 10.15 mJ

Total moles of CB consumed

$$= \text{Total heat supplied} / \text{Total heat required to consume 1 mol of CB}$$

$$= 3.02\text{e-}07$$

Volume of water vapor = 9.07323e-09 m³

Total number of aggregates = 7.52E+09

Volume of water vapor per aggregate

$$= \text{Total volume of the system} = \text{Volume of aggregate} + \text{Volume of water vapor}$$

$$= 4.1866\text{e-}21 \text{ m}^3 + 1.21\text{e-}18 \text{ m}^3$$

$$= 1.21\text{e-}18 \text{ m}^3$$

Radius of the bubble assuming the system is spherical = 762 nm

2. Difference of the energy between Mie and IR measurements went to vapor formation

Difference in energy = 10.15 mJ - 2.75 mJ = 7.4 mJ

Latent heat = 2.71e04 J/mol

Total volume of vapor produced = 5.45e-09 m³

Total number of nanoparticles = 7.52e09

Total volume of vapor per aggregate = 7.26e-19 m³

Total volume of vapor aggregate composite = 7.26e-19 m³

Radius of bubble assuming a spherical geometry = 645 nm

B.1.3 Reaction feasibility

1. Thermodynamics

Heat required to get 1 mol CB from 23°C to 100°C

$$= (1 \text{ mol}) * (8.4 \text{ J/mol/}^\circ\text{C}) * (100^\circ\text{C} - 23^\circ\text{C})$$

$$= 646.8 \text{ J}$$

Heat required to get 1 mol of water from 23°C to 100°C

$$\begin{aligned} &= (1 \text{ mol}) * (75.24 \text{ J/mol/}^\circ\text{C}) * (100^\circ\text{C} - 23^\circ\text{C}) \\ &= 5793.48 \text{ J} \end{aligned}$$

Heat required to vaporize 1 mol of water = 2.71e+04 J

Heat of reaction for 1 mol of CB consumption = 131000 J

Total heat required for 1 mol of CB to react = 1.65e+05 J

Total heat supplied per pulse = 10.15 mJ

Total moles of CB consumed per pulse

$$\begin{aligned} &= \text{Total heat supplied per pulse} / \text{Total heat required to consume 1 mol of CB} \\ &= 6.16795\text{e-}08 \end{aligned}$$

% of total CB consumed per pulse

$$\begin{aligned} &= \text{Total CB consumed per pulse} / \text{Total moles of CB} \\ &= 5\% \end{aligned}$$

Moles of CO produced = 6.16795e-08

Moles of H₂ produced = 6.16795e-08

Total volume of gases produced = Volume of CO + Volume of H₂

$$\begin{aligned} &= (\text{moles of CO}) * (\text{specific Volume of CO at } 100^\circ\text{C}) + (\text{moles of H}_2) * (\text{specific} \\ &\quad \text{volume of H}_2 \text{ at } 100^\circ\text{C}) \\ &= 1.1936\text{e-}09 \text{ m}^3 + 1.87\text{e-}09 \text{ m}^3 \\ &= 3.06\text{e-}09 \text{ m}^3 \end{aligned}$$

Percentage compared to vapor = 3.06e-09*100/9.07e-09=33%

2. Kinetics

Amount of gases produced per pulse = Rate of CO formation (m³ of CO/s/kg of CB)*(mass of CB)*time(s)

$$= (1.72\text{e-}04 \text{ m}^3/\text{kg/s}) * (1.48\text{e-}08 \text{ kg}) * (0.1 \text{ s})$$

$$= 2.55\text{E-}13 \text{ m}^3 \text{ (Note Kinetic predictions are much lower than thermodynamic calculations)}$$

% compared to vapor = 0.0028%

Amount of CO + CO₂ formed in 7 minutes (4200 pulses) = 1.07e-09 m³

$$= (1.07\text{e-}09 \text{ m}^3) / (0.085 \text{ m}^3/\text{mol}) = 1.25\text{e-}08 \text{ mols}$$

Amount of CB used in 7 minutes = 1.25×10^{-8} mols = 1.5078×10^{-10} kg

% of CB used in 7 minutes = $1.5078 \times 10^{-10} \times 100 / 1.4 \times 10^{-8} = 1.01\%$

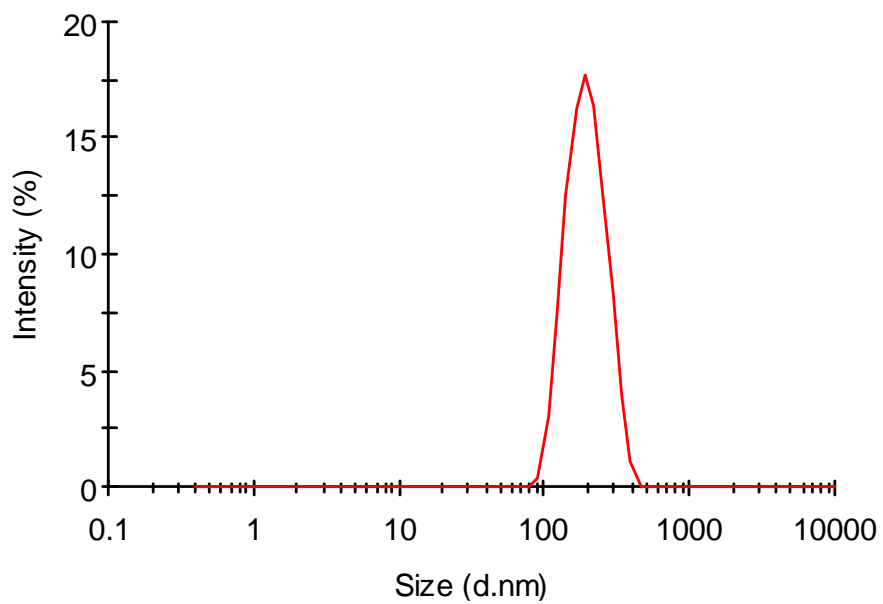


Figure B.1: DLS measurement of CB nanoparticles show a mean diameter of ~ 200 nm with a dispersity of 0.21. The suspension shows no sign of settling or aggregation over time.

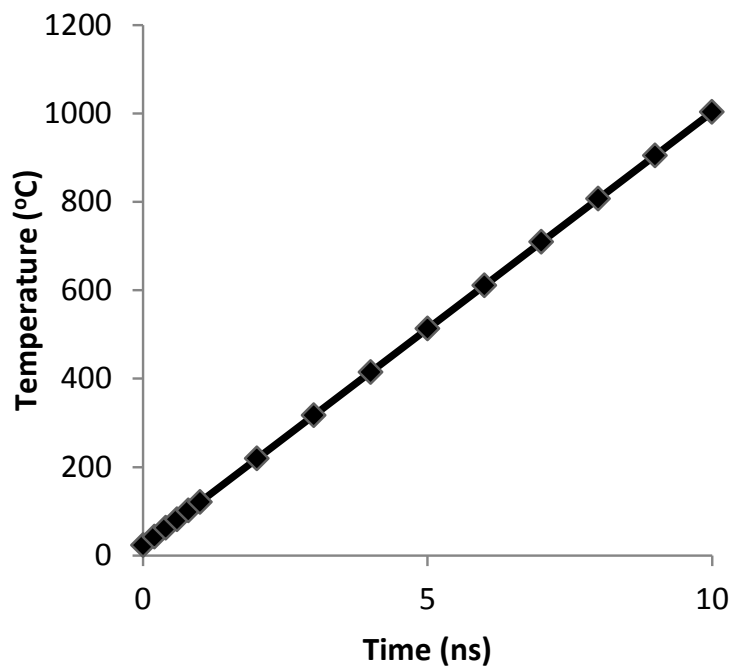


Figure B.2: Increase of particle temperature with time assuming first the surrounding temperature remains at 23°C and then once the vapor is formed, the bulk temperature goes to 100°C and stays there. This is the worst case scenario of heat transfer between particle and bulk.

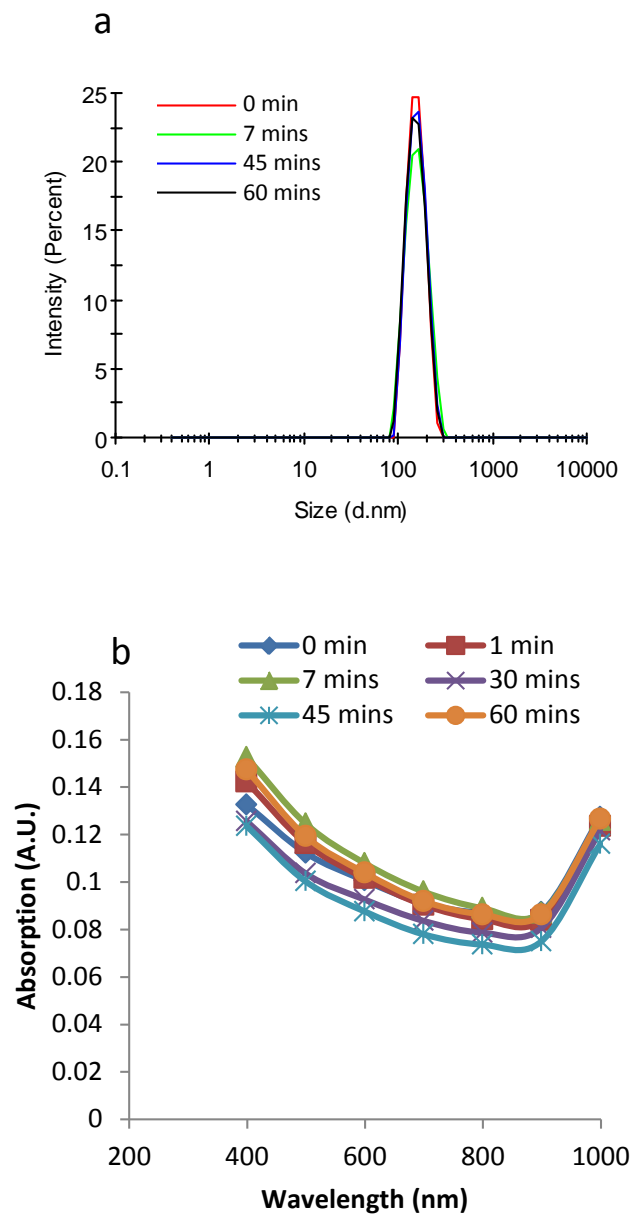


Figure B.3: Characterization of the CB suspension after the exposure. First the nanoparticle size was determined using DLS after either no exposure to laser till an hour of exposure (a). The absorption spectra were characterized for CB exposed for different time periods using a spectrophotometer to show that there is no statistical difference. (Error bars not shown, $n=3$).

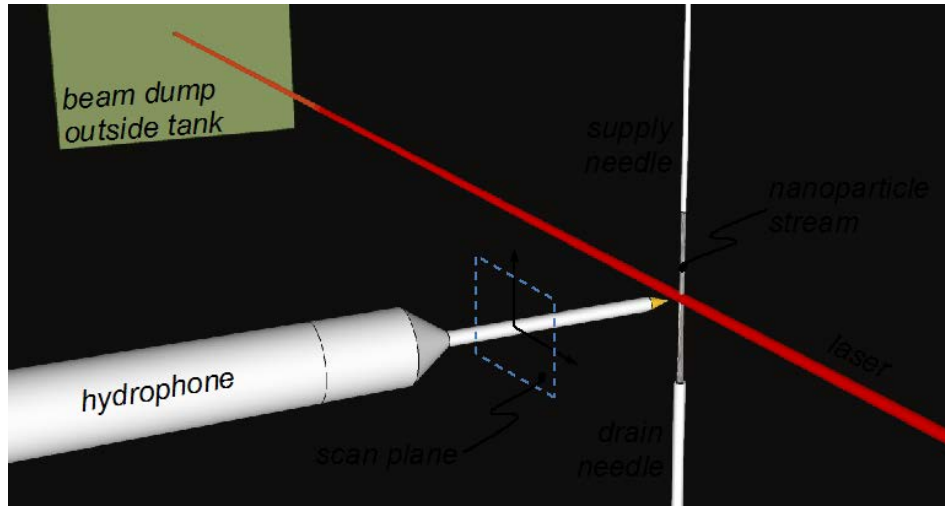


Figure B.4: The acoustic measurement setup which is used to characterize the acoustic output of the system. The hydrophone can be moved in the x,y and z directions relative to the stream of nanoparticles thereby enabling us to map the spatial pressure profile.

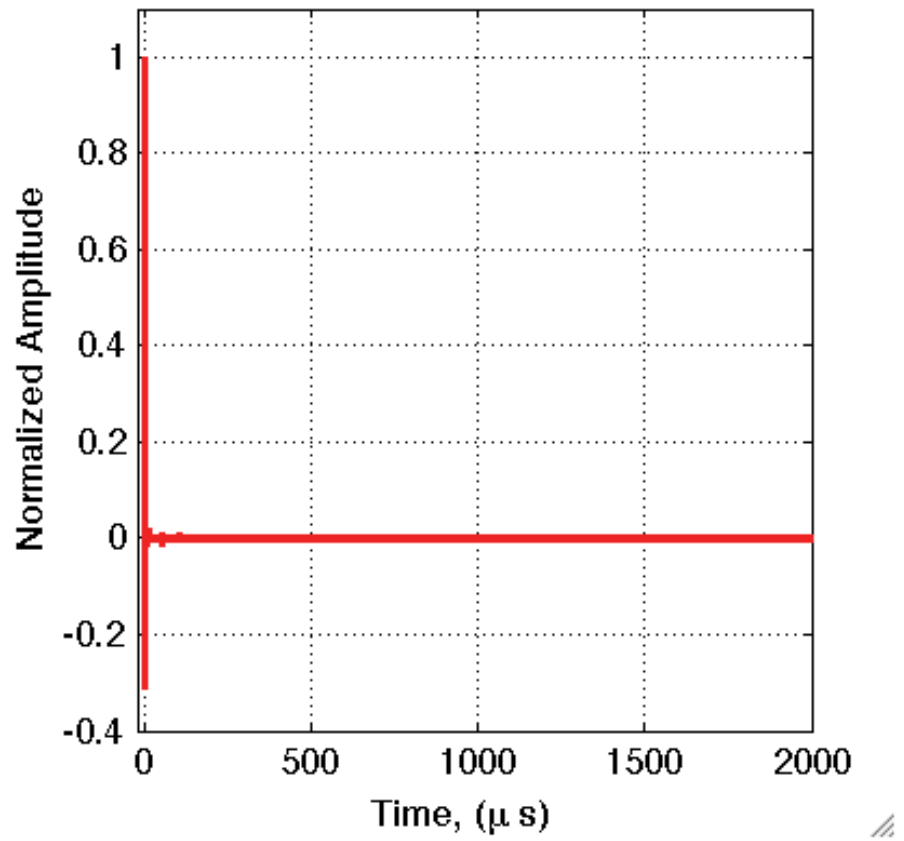


Figure B.5: Pressure output with an extended time. There is no further signal after the initial signal (as shown in Figure 5.5 in main thesis).

APPENDIX C

siRNA SUPPLEMENTARY INFORMATION

C.1 Materials and Methods

C.1.1 Cell Preparation

Human ovarian cancer cells (Hey A8-F8), kindly provided by Gordon B. Mills (MD Anderson Cancer Center, Houston, TX) and transfected with the pGL4.51[luc2/CMV/Neo] luciferase reporter vector (Promega, Madison, WI), were used in this work (Hey A8-F8) and maintained in RPMI-1640 medium supplemented with 10% FBS, penicillin-streptomycin-amphotericin B and 100 $\mu\text{g}/\text{ml}$ of Geneticin (GIBCO, Grand Island, NY). Silencer Select siRNA (EGFR) (ID: s564) or Silencer Select siRNA (Negative Control #1) (Ambion, Grand Island, NY) were dissolved in sterile nuclease-free water (Ambion) to create a 20 μM stock solution of siRNA.

C.1.2 Nanoparticle Preparation

To prepare the CB nanoparticle solution, 20 mg of CB (Black Pearls 470, Cabot, Boston, MA) were added to 50 ml of 0.013% (v/v) Tween 80 (Sigma-Aldrich, St. Louis, MO; added to reduce aggregation and settling of the nanoparticles) in DI water and sonicated for at least 15 min to obtain the final CB solution at a concentration of 400 mg/l. The size of the individual CB nanoparticles was 25 nm, but they were aggregated into larger particles of 189.3 ± 1.5 nm ($n = 3$) diameter with a dispersity of 0.16 ± 0.03 ($n = 3$), as determined from dynamic light scattering measurements (See Fig. 1A in main text). After making the 50 ml solution of CB nanoparticles, it was aliquoted into smaller 1.5 ml samples. Consistency of samples was determined by measuring the absorption spectra using a spectrophotometer (Synergy H4, BioTek, Winooski, VT) and comparing to predetermined standards.

C.1.3 Laser Apparatus

A Nd:YAG infrared laser (Surelite III, Continuum, Santa Clara, CA) was used to apply pulses of 1064 nm wavelength, 5 - 9 ns pulse length, and 75 - 175 mJ energy per pulse. Pulses were applied at a repetition rate of 10 Hz (i.e., 10 pulses per second). The energy was varied by manipulating the Q-switch timing. The beam was passed through a Faraday isolator to prevent back reflection. The laser beam was passed through a polarizer and quarter plate to fine tune the final output externally. The resulting 8 mm-diameter beam was then usually diverged to 21 mm diameter using a lens to illuminate the entire cuvette (exposure area of 4 cm²). Sham exposures were used as negative control experiments, where solutions containing cells, dextran or siRNA (s564) and CB nanoparticles went through all the same steps as exposed samples (see below), except that the laser was not turned on. Another negative control involved only cells without CB nanoparticles or siRNA.

C.1.4 Laser Exposure

A suspension of 490 μ l of Hey A8-F8 cells in RPMI-1640 medium (1.610^6 cells/ml) were combined with 50 μ l siRNA (2 μ M final concentration) stock solution and 37 μ l of CB nanoparticle suspension (25 mg/l final concentration) and irradiated with laser for 7 min at 18.75 mJ/cm² or 3 min at 25 mJ/cm² or 1 min at 44 mJ/cm² or not exposed to laser (sham). In some siRNA experiments, there was no CB added or anti-EGFR siRNA was replaced with negative control (NC) siRNA. After irradiation, cell suspensions with CB nanoparticles and dextran were either washed with 10% FBS-supplemented PBS three times and then cover-slipped and imaged with a fluorescence microscope or transferred to flow cytometry tubes for analysis. For siRNA experiments, cell suspensions with CB nanoparticles and siRNA were transferred into 6-well tissue culture plates (Falcon, Franklin Lakes, NJ) containing 2 ml of RPMI-1640 growth medium per well. Cells were incubated at 37°C in an atmosphere of humidified air with 5% CO₂ for 24 h, harvested by trypsin/EDTA and processed for the isolation of total-cell RNA.

As a transfection control, cells were transfected with s564 siRNA and NC-siRNA using Lipofectamine 2000 reagent (Invitrogen, Carlsbad, CA) as follows: Hey A8-F8 cells were

plated in RPMI-1640 growth medium into 6-well tissue culture plates (10^5 cells in 2 ml media per well) and incubated overnight at 37°C in an atmosphere of humidified air with 5% CO_2 . Thereafter, mixtures of 250 μl Opti-MEM (GIBCO) with 5 μl siRNA (500 nM) and 250 μl Opti-MEM with 5 μl Lipofectamine 2000 (0.25% v/v) were combined, incubated at room temperature for 20 min, diluted with 2 ml Opti-MEM and used to replace the medium in each well with transfected cells. After 4 h at 37°C in an atmosphere of humidified air with 5% CO_2 , the transfection medium was replaced with RPMI-1640 supplemented with 10% FBS (Cellgro), penicillin-streptomycin-amphotericin B; cells were then incubated for additional 24 h and harvested by trypsin/EDTA. All transfections or control treatments were performed in triplicate.

C.1.5 Analysis of FITC-dextran uptake

A bench-top flow cytometer (BD LSRII, BD Biosciences, San Jose, CA) was used to quantify uptake, i.e. the number of live cells with intracellular FITC-dextran, and viability, i.e. the number of live cells that were not necrotic or fragmented as determined by propidium iodide staining, on a cell-by-cell basis. For quantifying necrotic death, propidium iodide staining was analyzed using a PerCP-Cy5, 670 nm longpass filter. FITC-dextran uptake into cells was detected using a FITC, 530/28 nm bandpass filter. A cell gate was constructed based on forward-scattered and side-scattered light to determine the size distribution of cells in the control. Any events lying within this gate were considered to be cells, whereas events smaller than that were considered cell fragments or dead cells.

To determine the concentration of intact cells (and thereby account for possible cell loss due to fragmentation), we multiplied the volumetric flow rate in the flow cytometer by the time of analysis to determine the total volume analyzed. Dividing the number of cells detected within the gate by the volume provided the cell concentration, which was compared to non-exposed controls to determine cell loss due to fragmentation. The flow cytometer was run for 90 s, which resulted in collection approximately 10^5 cell events per sample ($\sim 20\%$ of the total cells present in each sample).

To account for spectral overlap between the dyes, compensation controls were run for

each experiment. Propidium iodide-positive samples were made by incubating cells in 70% methanol for 30 min and then washing with PBS. FITC-dextran-positive samples were made by exposing cells with CB nanoparticles and FITC-dextran at 44 mJ/cm² per shot for 7 min. At this condition, there was extensive cell death, but almost all cells which remained viable had FITC-dextran uptake.

C.1.6 Isolation of RNA

Cell pellets were processed for RNA isolation using mirVana miRNA isolation kit (Ambion) following the manufacturers protocol for total RNA isolation. Purity and concentration of total cell RNA were determined with NanoDrop 1000 Spectrophotometer (Thermo Scientific).

C.1.7 Analysis of siRNA uptake

Analysis of uptake of siRNA targeting EGFR gene (s564) was performed using TaqMan siRNA Assay s564.asy (Applied Biosystems/Life Technologies, Carlsbad, CA). From each treatment or control group, 10 ng of total cell RNA was denatured and reverse-transcribed using s564 RNA-specific stem-loop RT primer and TaqMan MicroRNA Reverse Transcription Kit in 15 μ l reactions following the manufacturer's recommendation. Subsequently, cDNA was amplified using TaqMan Universal Master Mix II with UNG in CFX96 Real Time PCR Detection System (BioRad, Hercules, CA) following the manufacturer's recommendation.

C.1.8 Analysis of EGFR expression

For analysis of expression of target EGFR and internal control GAPDH genes, 1.5 μ g of total cell RNA was reverse-transcribed in 20 μ l reactions using High Capacity cDNA Reverse Transcription Kit with RNase Inhibitor (Applied Biosystems/Life Technologies). For all transfected or control-treated cells, qPCR was performed in CFX96 Real Time PCR Detection System (BioRad) with 10 ng of cDNA per 20 μ l reactions using TaqMan assays

Hs01076078_m1 for EGFR, Hs02758991_g1 assay for GAPDH and TaqMan Universal Master Mix II with UNG (all from Applied Biosystems/Life Technologies) following the manufacturers recommendations. All qPCR reactions were performed in triplicate. Threshold cycles were determined using single threshold/baseline subtracted curve fit (CFX Manager Software) and averaged across technical replicates.

C.1.9 Data analysis and statistics

A minimum of three replicates was performed for all conditions. Replicates enabled calculation of means and standard deviation. For dextran uptake studies, the null hypothesis was that the average fraction of cells with uptake (or average fraction of viable cells) between a treated sample and a sham exposure were equal. To compare between mean values of two data points, an unpaired Students t-test was performed (2 tails) assuming unequal variances using GraphPad Prism 6 (GraphPad Software, La Jolla, CA). The differences between means were considered significant for $p < 0.05$.

For siRNA experiments, expression of EGFR gene relative to internal control GAPDH was presented using ΔCt method and the significance of differences between mean ΔCt values corresponding to experimental groups was tested using two-tailed t-test with Welch's correction. The differences between means were considered significant for $p < 0.05$. The concentration of s564 siRNA was expressed as 2^{-Ct} , where Ct represent mean threshold cycle values for s564 cDNA amplification across three biological replicates. Statistical significance of differences among mean Ct values was tested with one-way ANOVA with Tukey's post-test for significance of differences between all pairs of means, and considered significant at $p < 0.05$.

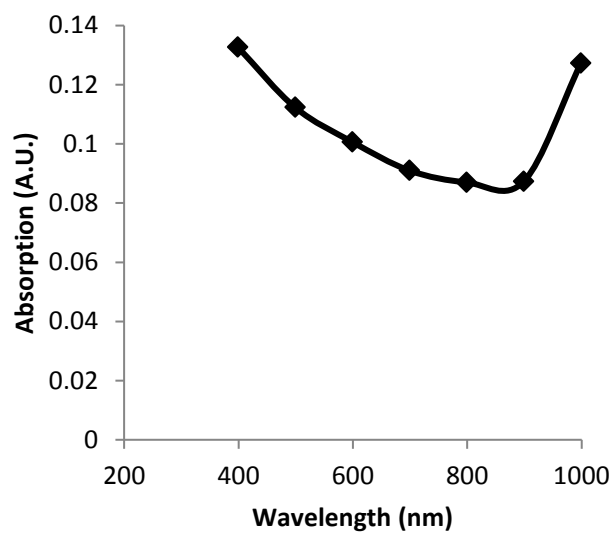


Figure C.1: Light absorption by CB nanoparticle solution versus wavelength. Absorption spectra measured using a spectrophotometer shows that CB nanoparticles absorbs across a wide range of wavelengths, including NIR.

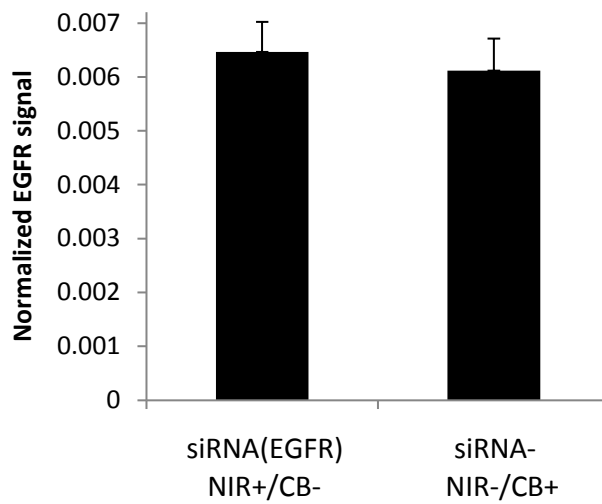


Figure C.2: Expression of EGFR in Hey A8 F8 cells treated with EGFR-siRNA and NIR laser, but no CB nanoparticles (left bar) and cells treated with CB nanoparticles, but no siRNA or laser (right bar). In both cases, there was no significant knock-down of target EGFR gene (2 tailed t-tests with Welchs corrections, $p = 0.5$). Expression presented in arbitrary units as mean \pm SD ($N = 3$).

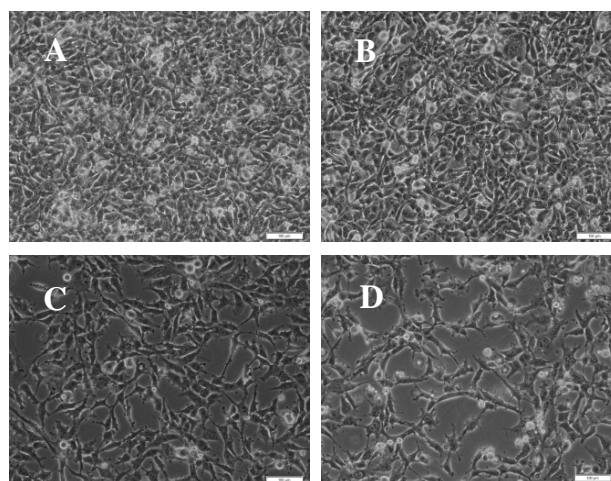


Figure C.3: Brightfield (phase contrast) micrographs of Hey A8 F8 cells 24 h post treatment with (A) CB only, (B) anti-EGFR siRNA and laser at 19 mJ/cm^2 for 7 min, (C) NC-siRNA, CB nanoparticles and laser at 19 mJ/cm^2 for 7 min and (D) anti-EGFR siRNA, CB nanoparticles and laser at 19 mJ/cm^2 for 7 minutes. Scale bars are $100 \mu\text{m}$.

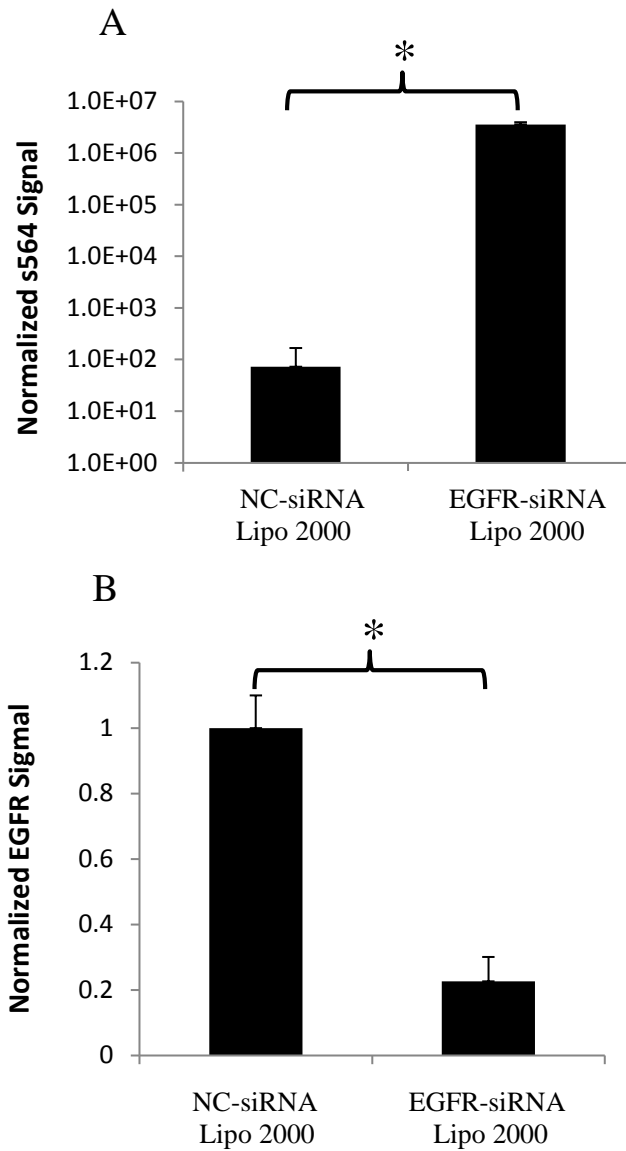


Figure C.4: Uptake of anti-EGFR (s564) siRNA and knockdown of EGFR using Lipofectamine 2000 (Lipo 2000) (A) Amount of intracellular siRNA (s564) (in arbitrary units), normalized to 10 ng of total RNA, quantified using qPCR when Hey A8-F8 cells with anti-EGFR siRNA or scrambled siRNA treated with the manufacturers recommended amount of Lipofectamine 2000. (B) EGFR mRNA level normalized relative to GAPDH level measured using qPCR showing knockdown when cells were treated with Lipofectamine 2000 and anti-EGFR siRNA compared to scrambled siRNA. Asterisk symbol (*) shows statistically significant differences in uptake and knockdown ($p < 0.05$). Data show mean \pm SD ($N = 3$).

C.2 Calculations

C.2.1 Number of siRNA per cell

1. Number of siRNA per cell (Lipofectamine 2000)

$$\begin{aligned} & \text{Total number of siRNA/ Total number of cells} \\ &= \text{molar concentration of stock siRNA} * \text{Volume of stock siRNA used} \\ & \quad * \text{Avogadros constant}/(\text{Cell concentration} * \text{Volume of cells used}) \\ &= (20 \mu\text{M}) * (5 \mu\text{l}) * 6.023 * 10^{23} / (10^5 \text{ cells/ml}) * (2 \text{ ml}) \\ &= 3.01 \times 10^8 \end{aligned}$$

2. Number of siRNA per cell (photoacoustic delivery)

$$\begin{aligned} & \text{Total number of siRNA/ Total number of cells} \\ &= \text{molar concentration of stock siRNA} * \text{Volume of stock siRNA used} \\ & \quad * \text{Avogadros constant}/(\text{Cell concentration} * \text{Volume of cells used}) \\ &= (20 \mu\text{M}) * (50 \mu\text{l}) * 6.023 * 10^{23} / (1.6 \times 10^6 \text{ cells/ml}) * (0.49 \text{ ml}) \\ &= 7.68 \times 10^8 \end{aligned}$$

C.2.2 Time scales

Time scale of conduction of heat to the surrounding water of 200 nm diameter particles

$$\begin{aligned} &= R^2 / 4 * \alpha_w \\ & \text{(where R is CB nanoparticle radius and } \alpha_w \text{ is thermal diffusivity of water)} \\ &= (10^{-7} \text{ m})^2 / 4 * (1.43 \times 10^{-7} \text{ m}^2/\text{s}) \\ &= 175 \text{ ns} \end{aligned}$$

Time scale of conduction of heat to the surrounding water of 50 nm diameter particles

$$\begin{aligned} &= R^2 / 4 * \alpha_w \\ & \text{(where R is CB nanoparticle radius and } \alpha_w \text{ is thermal diffusivity of water)} \\ &= (50 \times 10^{-9} \text{ m})^2 / 4 * (1.43 \times 10^{-7} \text{ m}^2/\text{s}) \\ &= 11 \text{ ns} \end{aligned}$$

REFERENCES

1. Timko BP, Whitehead K, Gao W et al. 2011. Advances in Drug Delivery. Annual Review of Materials Research 41: 1-20.
2. Tiwari G, Tiwari R, Sriwastawa B et al. 2012. Drug delivery systems: An updated review. Int J Pharm Investig 2: 2-11.
3. Torchilin VP. 2006. Recent approaches to intracellular delivery of drugs and DNA and organelle targeting. Annu Rev Biomed Eng 8: 343-375.
4. Varga CM, Wickham TJ, Lauffenburger DA. 2000. Receptor-mediated targeting of gene delivery vectors: Insights from molecular mechanisms for improved vehicle design. Biotechnology and Bioengineering 70: 593-605.
5. Chen H, Diebold G. 1995. Chemical Generation of Acoustic Waves: A Giant Photoacoustic Effect. Science 270: 963-966.
6. Roush SW, Murphy TV, Vaccine-Preventable Disease Table Working Group a. 2007. Historical comparisons of morbidity and mortality for vaccine-preventable diseases in the united states. JAMA 298: 2155-2163.
7. Langer R. 1998. Drug delivery and targeting. Nature 392: 5-10.
8. Langer R. 2001. DRUG DELIVERY: Drugs on Target. Science 293: 58-59.
9. Langer R. 1990. New Methods of Drug Delivery. Science 249: 1527-1533.
10. Illum L. 2003. Nasal drug delivery possibilities, problems and solutions. Journal of Controlled Release 87: 187-198.
11. Langer R. 2003. Where a Pill Won't Reach. Scientific American 288.

12. Langer R, Peppas NA. 2003. Advances in Biomaterials, Drug Delivery, and Bionanotechnology. *AIChE Journal* 49: 2990-3006.
13. D.D.Breimer. 1999. Future challenges for drug delivery. *Journal of Controlled Release* 62.
14. Faraji AH, Wipf P. 2009. Nanoparticles in cellular drug delivery. *Bioorganic & Medicinal Chemistry* 17: 2950-2962.
15. Smyth MJ, Krasovskis E, Sutton VR, Johnstone RW. 1998. The drug efflux protein, P-glycoprotein, additionally protects drug-resistant tumor cells from multiple forms of caspase-dependent apoptosis. *Proceedings of the National Academy of Sciences* 95: 7024-7029.
16. Lodhish H, Berk A, L. ZS et al. Receptor-Mediated Endocytosis and the Sorting of Internalized Proteins. *Molecular Cell Biology*. 4 ed. New York: W. H. Freeman 2000.
17. Varkouhi AK, Scholte M, Storm G, Haisma HJ. 2011. Endosomal Escape Pathways for Delivery of Biologicals. *J Controlled Release* 151: 220-228.
18. Xua ZP, Zengb QH, Lua GQ, Yub AB. 2006. Inorganic nanoparticles as carriers for efficient cellular delivery. *Chemical Engineering Science* 61.
19. J.P.Xu, J.Ji, W.D.Chen et al. 2005. Novel biomimetic polymersomes as polymer therapeutics for drug delivery. *Journal of Controlled Release* 107.
20. Moghimi SM, Hunter AC, Murray JC. 2005. Nanomedicine: current status and future prospects. *FASEB J* 19: 311-330.
21. Liong M, Lu J, Kovichich M et al. 2008. Multifunctional Inorganic Nanoparticles for Imaging, Targeting, and Drug Delivery. *ACS Nano* 2: 889-896.
22. Kumari A, Yadav SK, Yadav SC. 2010. Biodegradable polymeric nanoparticles based drug delivery systems. *Colloids and Surfaces B: Biointerfaces* 75: 1-18.

23. Junghanns JU, Muller RH. 2008. Nanocrystal technology, drug delivery and clinical applications. *Int J Nanomedicine* 3: 295-309.
24. Wissing SA, Kayser O, Mller RH. 2004. Solid lipid nanoparticles for parenteral drug delivery. *Advanced Drug Delivery Reviews* 56: 1257-1272.
25. Allen TM, Cullis PR. 2013. Liposomal drug delivery systems: From concept to clinical applications. *Advanced Drug Delivery Reviews* 65: 36-48.
26. Kesharwani P, Jain K, Jain NK. 2014. Dendrimer as nanocarrier for drug delivery. *Progress in Polymer Science* 39: 268-307.
27. Immordino ML, Dosio F, Cattel L. 2006. Stealth liposomes: review of the basic science, rationale, and clinical applications, existing and potential. *Int J Nanomedicine* 1: 297-315.
28. Mozafari MR. 2005. Liposomes: an overview of manufacturing techniques. *Cell Mol Biol Lett* 10: 711-719.
29. Vinogradov SV, Zeman AD, Batrakova EV, Kabanov AV. 2005. Polyplex Nanogel formulations for drug delivery of cytotoxic nucleoside analogs. *Journal of Controlled Release* 107: 143-157.
30. Kleemann E, Jekel N, Dailey LA et al. 2009. Enhanced gene expression and reduced toxicity in mice using polyplexes of low-molecular-weight poly(ethylene imine) for pulmonary gene delivery. *J Drug Target* 17: 638-651.
31. Desai N. 2012. Challenges in development of nanoparticle-based therapeutics. *AAPS J* 14: 282-295.
32. De Jong WH, Borm PJ. 2008. Drug delivery and nanoparticles: applications and hazards. *Int J Nanomedicine* 3: 133-149.
33. Sahay G, Querbes W, Alabi C et al. 2013. Efficiency of siRNA delivery by lipid nanoparticles is limited by endocytic recycling. *Nat Biotech* 31: 653-658.

34. Kay MA, Glorioso JC, Naldini L. 2001. Viral vectors for gene therapy: the art of turning infectious agents into vehicles of therapeutics. *Nat Med* 7: 33-40.
35. Yi Y, Noh MJ, Lee KH. 2011. Current advances in retroviral gene therapy. *Curr Gene Ther* 11: 218-228.
36. Wang AY, Peng PD, Ehrhardt A et al. 2004. Comparison of adenoviral and adeno-associated viral vectors for pancreatic gene delivery in vivo. *Hum Gene Ther* 15: 405-413.
37. Bouard D, Alazard-Dany D, Cosset FL. 2009. Viral vectors: from virology to transgene expression. *Br J Pharmacol* 157: 153-165.
38. Murakami T, Sunada Y. 2011. Plasmid DNA gene therapy by electroporation: principles and recent advances. *Curr Gene Ther* 11: 447-456.
39. Meacham JM, Durvasula K, Degertekin FL, Fedorov AG. 2013. Physical Methods for Intracellular Delivery: Practical Aspects From Laboratory Use to Industrial-Scale Processing. *J Lab Autom*: 1-18.
40. Mehier-Humbert S, Guy RH. 2005. Physical methods for gene transfer: improving the kinetics of gene delivery into cells. *Adv Drug Delivery Rev* 57: 733-753.
41. Wells DJ. 2004. Gene therapy progress and prospects: Electroporation and other physical methods. *Gene Therapy* 11: 1363-1369.
42. Hutcheson JD, Schlicher RK, Hicks HK, Prausnitz MR. 2010. Saving Cells from Ultrasound-Induced Apoptosis: Quantification of Cell Death and Uptake Following Sonication and Effects of Targeted Calcium Chelation. *Ultrasound in Medicine & Biology* 36: 1008-1021.
43. U.Zimmermann, G.Pilwat, F.Rieman. 1974. Dielectric breakdown of cell membranes. *Biophysics Journal* 14.
44. Gehl J. 2003. Electroporation: theory and methods, perspectives for drug delivery, gene therapy and research. *Acta Physiol Scand* 177: 437-447.

45. Canatella PJ, Karr JF, Petros JA, Prausnitz MR. 2001. Quantitative study of electroporation-mediated molecular uptake and cell viability. *Biophysical Journal* 80: 755-764.
46. H.Aihara, Miyazaki JJM. 1998. Gene transfer into muscle by electroporation in vivo. *Nature Biotechnology* 16.
47. Hui SW. 2008. Overview of drug delivery and alternative methods to electroporation. *Methods Mol Biol* 423: 91-107.
48. Chalberg TW, Vankov A, Molnar FE et al. 2006. Gene transfer to rabbit retina with electron avalanche transfection. *Invest Ophthalmol Vis Sci* 47: 4083-4090.
49. Liu Y, Yan J, Prausnitz MR. 2012. Can Ultrasound Enable Efficient Intracellular Uptake of Molecules? A Retrospective Literature Review and Analysis. *Ultrasound in Med & Biol* 38: 876-888.
50. Guzman HR, Nguyen DX, Khan S, Prausnitz MR. 2001. Ultrasound-mediated disruption of cell membranes. I. Quantification of molecular uptake and cell viability. *J Acoust Soc Am* 110: 588-596.
51. Hallow DM, Mahajan AD, McCutchen TE, Prausnitz MR. 2006. Measurement and correlation of acoustic cavitation with cellular bioeffects. *Ultrasound in Medicine & Biology* 32: 1111-1122.
52. Mehier-Humbert S, Bettinger T, Yan F, Guy RH. 2005. Plasma membrane poration induced by ultrasound exposure: implication for drug delivery. *J Controlled Release* 104: 213-222.
53. Bazan-Peregrino M, Rifai B, Carlisle RC et al. Cavitation-enhanced delivery of a replicating oncolytic adenovirus to tumors using focused ultrasound. *Journal of Controlled Release* 169: 40-47.
54. Q.L.Lu, H.D.Liang, T.Partridge, M.J.Blomley. 2003. Microbubble ultrasound improves the efficiency of gene transduction in skeletal muscle in vivo with reduced

- tissue damage. *Gene Therapy* 10: 396-405.
55. Schlicher RK, Radhakrishna H, Tolentino TP et al. 2006. Mechanism of Intracellular Delivery by Acoustic Cavitation. *Ultrasound in Med & Biol* 32: 915-924.
 56. Guzman HR, McNamara AJ, Nguyen DX, Prausnitz MR. 2003. Bioeffects caused by changes in acoustic cavitation bubble density and cell concentration: a unified explanation based on cell-to-bubble ratio and blast radius. *Ultrasound in Medicine & Biology* 29: 1211-1222.
 57. Nasheuer HP. 2010. *Genome stability and human diseases*. Dordrecht; New York: Springer
 58. R.J.Griesbach. 1987. Chromosome mediated transformation via microinjection. *Plant Science* 50: 69-77.
 59. Klein TM, Wolf ED, Wu R, Sanford JC. 1987. High-velocity microprojectiles for delivering nucleic acids into living cells. *Nature* 327: 70-73.
 60. Praitis V. 2006. Creation of Transgenic Lines Using Microparticle Bombardment Methods. In: Strange K, editor. *C elegans: Humana Press* p 93-107.
 61. O'Brien JA, Lummis SC. 2011. Nano-biistics: a method of biolistic transfection of cells and tissues using a gene gun with novel nanometer-sized projectiles. *BMC Biotechnol* 11: 66.
 62. Kitagawa T, Iwazawa T, Robbins PD et al. 2003. Advantages and limitations of particle-mediated transfection (gene gun) in cancer immuno-gene therapy using IL-10, IL-12 or B7-1 in murine tumor models. *J Gene Med* 5: 958-965.
 63. Plank C, Schillinger U, Scherer F et al. 2003. The magnetofection method: Using magnetic force to enhance gene delivery. *Biol Chem* 384: 737-747.
 64. Scherer F, Anton M, Schillinger U et al. 2002. Magnetofection: enhancing and targeting gene delivery by magnetic force in vitro and in vivo. *Gene Ther* 9: 102-109.

65. Rodriguez-Devora JI, Ambure S, Shi ZD et al. 2012. Physically facilitating drug-delivery systems. *Ther Deliv* 3: 125-139.
66. Zarnitsyn VG, Prausnitz MR. 2004. Physical parameters influencing optimization of ultrasound-mediated DNA transfection. *Ultrasound Med Biol* 30: 527-538.
67. Herd RM, Mrcp, Dover JS, Arndt KA. 1997. BASIC LASER PRINCIPLES. *Dermatologic Clinics* 15: 355-372.
68. Siegman AE. 1986. *Lasers*. Mill Valley, Calif.: University Science Books
69. Diels J-CRW. Ultrashort laser pulse phenomena fundamentals, techniques, and applications on a femtosecond time scale. 2006 [cited; Available from: <http://www.engineeringvillage.com/>]
70. Vogel A. 2005. Mechanisms of femtosecond laser nanosurgery of cells and tissues. *Applied Physics B: Lasers and Optics* 81: 1015-1047.
71. Weiblinger RP. 1986. Review of the clinical literature on the use of the Nd:YAG laser for posterior capsulotomy. *J Cataract Refract Surg* 12: 162-170.
72. Maiman TH. 1960. Stimulated Optical Radiation in Ruby. *Nature* 187: 493-494.
73. Duarte FJ. 1995. *Tunable laser applications*. New York: M. Dekker
74. Duarte FJEKC. Two-laser therapy and diagnosis device. Google Patents 1988.
75. Duarte FJHLWLPFKP. *Dye Laser Principles With Applications*. 1990 [cited; Available from: <http://public.eblib.com/EBLPublic/PublicView.do?ptiID=1180800>]
76. Jelnkov H. 2013. *Lasers for medical applications : diagnostics, therapy and surgery*
77. Waleed M, Hwang S-U, Kim J-D et al. 2013. Single-cell optoporation and transfection using femtosecond laser and optical tweezers. *Biomed Opt Express* 4: 1533-1547.
78. Clark IB, Hanania EG, Stevens J et al. 2006. Optoinjection for efficient targeted delivery of a broad range of compounds and macromolecules into diverse cell types. *J Biomed Opt* 11: 014034.

79. Doukas AG, Flotte TJ. 1996. Physical Characteristics and Biological Effects of Laser-Induced Stress Waves. *Ultrasound Med Biol* 22: 151-164.
80. Lee AU, Doukas AG. 1999. Laser-generated stress waves and their effects on the cell membrane. *IEEE J Sel Top Quantum Electron* 5: 997-1003.
81. Kodama T, Doukas AG, Hamblin MR. 2002. Shock wave-mediated molecular delivery into cells. *Biochim Biophys Acta* 1542: 186-194.
82. Angelos S, Choi E, Vgtle F et al. 2007. Photo-Driven Expulsion of Molecules from Mesostuctured Silica Nanoparticles. *J Phys Chem C* 111: 6589-6592.
83. Rajian JR, Fabiilli ML, Fowlkes JB et al. 2011. Drug delivery monitoring by photoacoustic tomography with an ICG encapsulated double emulsion. *Opt Express* 19: 14335-14347.
84. Park HK, Kim D, Grigoropoulos CP, Tam AC. 1996. Pressure generation and measurement in the rapid vaporization of water on a pulsed-laser-heated surface. *Journal of Applied Physics* 80: 4072-4081.
85. A.G.Doukas, Daniel J, V.Venugopalan, Flotte TJ. 1995. Physical factors involved in stress-wave-induced cell injury: The effect of stress gradient
86. Doukas AG, Flotte TJ. 1993. Biological Effects of Laser-Induced Shock-Waves - Structural And Functional Cell-Damage Invitro. *Ultrasound Med Biol* 19: 137-146.
87. Lee S, McAuliffe DJ, Kollias N et al. 2002. Photomechanical delivery of 100-nm microspheres through the stratum corneum: Implications for transdermal drug delivery. *Lasers in Surgery and Medicine* 31: 207-210.
88. Montellano A, Da Ros T, Bianco A, Prato M. 2011. Fullerene C60 as a multifunctional system for drug and gene delivery. *Nanoscale* 3: 4035-4041.
89. Cai D, Mataraza JM, Qin ZH et al. 2005. Highly efficient molecular delivery into mammalian cells using carbon nanotube spearing. *Nat Methods* 2: 449-454.

90. Cheng C, Miller KH, Koziol KKK et al. 2009. Toxicity and imaging of multi-walled carbon nanotubes in human macrophage cells. *Biomaterials* 30: 4152-4160.
91. Yang S-T, Wang X, Wang H et al. 2009. Carbon Dots as Nontoxic and High-Performance Fluorescence Imaging Agents. *The Journal of Physical Chemistry C* 113: 18110-18114.
92. Bond TC, Doherty SJ, Fahey DW et al. 2013. Bounding the role of black carbon in the climate system: A scientific assessment. *Journal of Geophysical Research: Atmospheres* 118: 5380-5552.
93. Mallidi S, Larson T, Tam J et al. 2009. Multiwavelength Photoacoustic Imaging and Plasmon Resonance Coupling of Gold Nanoparticles for Selective Detection of Cancer. *Nano Letters* 9: 2825-2831.
94. Shinto H, Fukasawa T, Aoki H et al. 2013. Acoustic pressure pulses from laser-irradiated suspensions containing gold nanospheres in water: Experimental and theoretical study. *Colloids and Surfaces A: Physicochemical and Engineering Aspects* 430: 51-57.
95. Singhana B, Slattery P, Chen A et al. 2014. Light-Activatable Gold Nanoshells for Drug Delivery Applications. *AAPS PharmSciTech*.
96. Krpetic Ze, Nativo P, See V et al. 2010. Inflicting Controlled Nonthermal Damage to Subcellular Structures by Laser-Activated Gold Nanoparticles. *Nano Letters* 10: 4549-4554.
97. Minai L, Yeheskely-Hayon D, Yelin D. 2013. High levels of reactive oxygen species in gold nanoparticle-targeted cancer cells following femtosecond pulse irradiation. *Sci Rep* 3.
98. Yao C, Qu X, Zhang Z et al. 2009. Influence of laser parameters on nanoparticle-induced membrane permeabilization. *J Biomed Opt* 14: 054034.

99. Bhattacharyya K, Mehta S, Viator J. 2012. Optically absorbing nanoparticle mediated cell membrane permeabilization. *Opt Lett* 37: 4474-4476.
100. CHEN HX, DIEBOLD G. 1995. Chemical Generation of Acoustic-Waves - A Giant Photoacoustic Effect. *Science* 270: 963-966.
101. Beveridge AC, McGrath TE, Diebold GJ. 1999. Photoacoustic shock generation in carbon suspensions. *Appl Phys Lett* 75.
102. Lowen H, Madden PA. A microscopic mechanism for shock-wave generation in pulsed-laser-heated colloidal suspensions. *J Chem Phys* 97.
103. Chen H, T.McGrath, G.Diebold. 1997. Laser Chemistry in Suspensions: new products and Unique Reaction Conditions for the Carbon-Steam Reaction. *Angew Chem, Int Ed Engl* 36.
104. McGrath TE, Diebold GJ. 2002. Laser-Initiated Chemical Reactions in Carbon Suspensions. *J Phys Chem* 106: 10072-10078.
105. McGrath TE, Beveridge AC, Diebold GJ. 1998. Sonoluminescence initiated by laser irradiation of carbon suspensions. *Applied Physics Letters* 73.
106. Kotaidis V. 2005. Cavitation dynamics on the nanoscale. *Applied Physics Letters* 87: 21.
107. Lin CP, Keijy MW. 1998. Cavitation and acoustic emission around laser-heated microparticles. *Appl Phys Lett* 72.
108. Chakravarty P, Qian W, El-Sayed MA, Prausnitz MR. 2010. Delivery of molecules into cells using carbon nanoparticles activated by femtosecond laser pulses. *Nat Nano* 5: 607-611.
109. Fire A, Xu S, Montgomery MK et al. 1998. Potent and specific genetic interference by double-stranded RNA in *Caenorhabditis elegans*. *Nature* 391: 806-811.

110. Jorgensen R. 1990. Altered gene expression in plants due to trans interactions between homologous genes. *Trends in Biotechnology* 8: 340-344.
111. Romano N, Macino G. 1992. Quelling: transient inactivation of gene expression in *Neurospora crassa* by transformation with homologous sequences. *Molecular Microbiology* 6: 3343-3353.
112. Pasquinelli AE, Ruvkun G. 2002. Control of developmental timing by microRNAs and their targets. *Annu Rev Cell Dev Biol* 18: 495-513.
113. Elbashir SM, Harborth J, Lendeckel W et al. 2001. Duplexes of 21-nucleotide RNAs mediate RNA interference in cultured mammalian cells. *Nature* 411: 494-498.
114. Tuschl T, Zamore PD, Lehmann R et al. 1999. Targeted mRNA degradation by double-stranded RNA in vitro. *Genes Dev* 13: 3191-3197.
115. Zamore PD, Tuschl T, Sharp PA, Bartel DP. 2000. RNAi: Double-Stranded RNA Directs the ATP-Dependent Cleavage of mRNA at 21 to 23 Nucleotide Intervals. *Cell* 101: 25-33.
116. Hamilton AJ, Baulcombe DC. 1999. A Species of Small Antisense RNA in Posttranscriptional Gene Silencing in Plants. *Science* 286: 950-952.
117. Bernstein E, Caudy AA, Hammond SM, Hannon GJ. 2001. Role for a bidentate ribonuclease in the initiation step of RNA interference. *Nature* 409: 363-366.
118. Dykxhoorn DM, Novina CD, Sharp PA. 2003. Killing the messenger: short RNAs that silence gene expression. *Nat Rev Mol Cell Biol* 4: 457-467.
119. Gitlin L, Karelsky S, Andino R. 2002. Short interfering RNA confers intracellular antiviral immunity in human cells. *Nature* 418: 430-434.
120. Das AT, Brummelkamp TR, Westerhout EM et al. 2004. Human immunodeficiency virus type 1 escapes from RNA interference-mediated inhibition. *J Virol* 78: 2601-2605.

121. Boden D, Pusch O, Lee F et al. 2003. Human immunodeficiency virus type 1 escape from RNA interference. *J Virol* 77: 11531-11535.
122. Dorsett Y, Tuschl T. 2004. siRNAs: applications in functional genomics and potential as therapeutics. *Nat Rev Drug Discov* 3: 318-329.
123. Sledz CA, Holko M, de Veer MJ et al. 2003. Activation of the interferon system by short-interfering RNAs. *Nat Cell Biol* 5: 834-839.
124. Akhtar S, Benter I. 2007. Toxicogenomics of non-viral drug delivery systems for RNAi: Potential impact on siRNA-mediated gene silencing activity and specificity. *Advanced Drug Delivery Reviews* 59: 164-182.
125. Lieberman J, Song E, Lee S-K, Shankar P. 2003. Interfering with disease: opportunities and roadblocks to harnessing RNA interference. *Trends in molecular medicine* 9: 397-403.
126. Reich SJ. 2003. Small interfering RNA (siRNA) targeting VEGF effectively inhibits ocular neovascularization in a mouse model. *Mol Vision* 9: 210-216.
127. Tolentino MJ. 2004. Intravitreal injection of vascular endothelial growth factor small interfering RNA inhibits growth and leakage in a nonhuman primate, laser-induced model of choroidal neovascularization. *Retina* 24: 132-138.
128. Nakamura H. 2004. RNA interference targeting transforming growth factor-[beta] type II receptor suppresses ocular inflammation and fibrosis. *Mol Vision* 10: 703-711.
129. Li BJ. 2005. Using siRNA in prophylactic and therapeutic regimens against SARS coronavirus in Rhesus macaque. *Nature Med* 11: 944-951.
130. Geisbert TW. 2006. Postexposure protection of guinea pigs against lethal ebola virus challenge is conferred by RNA interference. *J Infect Dis* 193: 1650-1657.
131. Shegokar R, Al Shaal L, Mishra PR. 2011. SiRNA delivery: challenges and role of carrier systems. *Pharmazie* 66: 313-318.

132. Lee W-R, Shen S-C, Chen W-Y et al. Noninvasive delivery of siRNA and plasmid DNA into skin by fractional ablation: Erbium:YAG laser versus CO2 laser. *European Journal of Pharmaceutics and Biopharmaceutics*.
133. Braun GB, Pallaoro A, Wu G et al. 2009. Laser-Activated Gene Silencing via Gold Nanoshell-siRNA Conjugates. *ACS Nano* 3: 2007-2015.
134. Templeton NS. 2008. *Gene and Cell Therapy: Therapeutic Mechanisms and Strategies*. Third ed. Boca Raton, Florida: CRC Press
135. Yang A, Wilson NS, Ashkenazi A. 2010. Proapoptotic DR4 and DR5 Signaling in Cancer Cells: Toward Clinical Translation. *Curr Opin Cell Biol* 22: 837-844.
136. Perez-Pinzon MA, Stetler RF, Fiskum G. 2012. Novel Mitochondrial Targets for Neuroprotection. *J Cereb Blood Flow Metab* 32: 1362-1376.
137. Sioud M. 2009. *siRNA and miRNA Gene Silencing: From Bench to Bedside (Methods in Molecular Biology, Vol. 487)* New York: Humana Press
138. Panyam J, Labhasetwar V. 2012. Biodegradable Nanoparticles for Drug and Gene Delivery to Cells and Tissue. *Adv Drug Delivery Rev* 64, Supplement: 61-71.
139. Thomas CE, Ehrhardt A, Kay MA. 2003. Progress and Problems with the Use of Viral Vectors for Gene Therapy. *Nat Rev Genet* 4: 346-358.
140. Gehl J. 2003. Electroporation: Theory and Methods, Perspectives for Drug Delivery, Gene Therapy and Research. *Acta Physiol Scand* 177: 437-447.
141. Kumar A, Ma H, Zhang X et al. 2012. Gold nanoparticles functionalized with therapeutic and targeted peptides for cancer treatment. *Biomaterials* 33: 1180-1189.
142. Lentacker I, De Cock I, Deckers R et al. 2013. Understanding Ultrasound Induced Sonoporation: Definitions and Underlying Mechanisms. *Adv Drug Delivery Rev*.
143. Zhang Y, Yu LC. 2008. Microinjection As a Tool of Mechanical Delivery. *Curr Opin Biotechnol* 19: 506-510.

144. Zhong P, Lin H Fau - Xi X, Xi X Fau - Zhu S et al. 1999. Shock Wave-Inertial Microbubble Interaction: Methodology, Physical Characterization, and Bioeffect Study. *J Acoust Soc Am* 105: 1997-2009.
145. Kodama T, Doukas AG, Hamblin MR. 2002. Shock Wave-Mediated Molecular Delivery Into Cells. *Biochim et Biophys Acta, Mol Cell Res* 1542: 186-194.
146. Yao C, Qu X, Zhang Z et al. 2009. Influence of Laser Parameters on Nanoparticle-Induced Membrane Permeabilization. *BIOMEDO* 14: 054034/054031-054034/054037.
147. Qin Z, Bischof JC. 2012. Thermophysical and Biological Responses of Gold Nanoparticle Laser Heating. *Chem Soc Rev* 41: 1191-1217.
148. Pitsillides CM, Joe EK, Wei X et al. 2003. Selective Cell Targeting with Light-Absorbing Microparticles and Nanoparticles. *Biophys J* 84: 4023-4032.
149. Vivero-Escoto JL, Slowing II, Wu C-W, Lin VSY. 2009. Photoinduced Intracellular Controlled Release Drug Delivery in Human Cells by Gold-Capped Mesoporous Silica Nanosphere. *J Am Chem Soc* 131: 3462-3463.
150. Paasonen L, Sipil T, Subrizi A et al. 2010. Gold-Embedded Photosensitive Liposomes for Drug Delivery: Triggering Mechanism and Intracellular Release. *J Controlled Release* 147: 136-143.
151. El-Sayed IH, Huang X, El-Sayed MA. 2006. Selective Laser Photo-Thermal Therapy of Epithelial Carcinoma Using Anti-EGFR Antibody Conjugated Gold Nanoparticles. *Cancer Letters* 239: 129-135.
152. Chakravarty P, Qian W, El-Sayed MA, Prausnitz MR. 2010. Delivery of molecules into cells using carbon nanoparticles activated by femtosecond laser pulses. *Nat Nanotechnol* 5: 607-611.
153. Stone KR, Mickey DD, Wunderli H et al. 1978. Isolation of a Human Prostate Carcinoma Cell Line (DU 145). *Int J Cancer* 21: 274-281.

154. Watkins S, Borthwick G, Arthur H. 2011. The H9c2 Cell Line and Primary Neonatal Cardiomyocyte Cells Show Similar Hypertrophic Responses in Vitro. *In Vitro CellDevBiol-Animal* 47: 125-131.
155. Halpern B, Benacerraf B, Biozzi G. 1953. Quantitative Study of the Granuloplectic Activity of the Reticulo-Endothelial System. I: The Effect of the Ingredients Present in India Ink and of Substances Affecting Blood Clotting in Vivo on the Fate of Carbon Particles Administered Intravenously in Rats, Mice and Rabbits. *Br J Exp Pathol* 34: 426-440.
156. Madsen SJ, Patterson MS, Wilson BC. 1992. The Use of India Ink As an Optical Absorber in Tissue-Simulating Phantoms. *Phys Med Biol* 37: 985-993.
157. Faraggi E, Gerstman BS, Sun J. 2005. Biophysical Effects of Pulsed Lasers in the Retina and Other Tissues Containing Strongly Absorbing Particles: Shockwave and Explosive Bubble Generation. *BIOMEDO* 10: 064029/064021-064029/064010.
158. Leighton TG. *The Acoustic Bubble*: Academic Press 1994.
159. Prausnitz MR, Lau BS, Milano CD et al. 1993. A Quantitative Study of Electroporation Showing a Plateau in Net Molecular Transport. *Biophys J* 65: 414-422.
160. Oliver JD, 3rd, Anderson S Fau - Troy JL, Troy JI Fau - Brenner BM et al. 1992. Determination of Glomerular Size-Selectivity in the Normal Rat with Ficoll. *JASN* 3: 214-218.
161. Escoffre JM, Rols MP. 2012. Electrochemotherapy: Progress and Prospects. *Curr Pharm Des* 18: 3406-3415.
162. Malietzis G, Monzon L, Hand J et al. 2013. High-Intensity Focused Ultrasound: Advances in Technology and Experimental Trials Support Enhanced Utility of Focused Ultrasound Surgery in Oncology. *Br J of Radiol* 86: 20130044.
163. Allen TM, Cullis PR. 2004. Drug Delivery Systems: Entering the Mainstream. *Science* 303: 1818-1822.

164. Torchilin VP, Lukyanov AN. 2003. Peptide and protein drug delivery to and into tumors: challenges and solutions. *Drug Discovery Today* 8: 259-266.
165. Lange MJ, Sharma TK, Whatley AS et al. 2012. Robust Suppression of HIV Replication by Intracellularly Expressed Reverse Transcriptase Aptamers Is Independent of Ribozyme Processing. *Mol Ther* 20: 2304-2314.
166. Noguchi T, Kato T, Wang L et al. 2012. Intracellular tumor-associated antigens represent effective targets for passive immunotherapy. *Cancer Res* 72: 1672-1682.
167. Hui S-W. 2008. Overview of Drug Delivery and Alternative Methods to Electroporation. In: Li S, editor. *Electroporation Protocols: Humana Press* p 91-107.
168. Sengupta A, Kelly SC, Dwivedi N et al. 2014. Efficient Intracellular Delivery of Molecules with High Cell Viability Using Nanosecond-Pulsed Laser-Activated Carbon Nanoparticles. *ACS Nano* 8: 2889-2899.
169. Ramrez OT, Mutharasan R. 1990. The role of the plasma membrane fluidity on the shear sensitivity of hybridomas grown under hydrodynamic stress. *Biotechnology and Bioengineering* 36: 911-920.
170. Murhammer DW, Goochee CF. 1990. Sparged Animal Cell Bioreactors: Mechanism of Cell Damage and Pluronic F-68 Protection. *Biotechnology Progress* 6: 391-397.
171. Tsoneva I, Iordanov I, Berger AJ et al. 2010. Electrodelivery of Drugs into Cancer Cells in the Presence of Poloxamer 188. *Journal of Biomedicine and Biotechnology* 2010.
172. Lee RC, River LP, Pan FS et al. 1992. Surfactant-induced sealing of electropermeabilized skeletal muscle membranes in vivo. *Proc Natl Acad Sci U S A* 89: 4524-4528.
173. Chen Y-C, Liang H-D, Zhang Q-P et al. 2006. Pluronic block copolymers: Novel functions in ultrasound-mediated gene transfer and against cell damage. *Ultrasound in Medicine & Biology* 32: 131-137.

174. Alexandridis P, Holzwarth JF, Hatton TA. 1994. Micellization of Poly(ethylene oxide)-Poly(propylene oxide)-Poly(ethylene oxide) Triblock Copolymers in Aqueous Solutions: Thermodynamics of Copolymer Association. *Macromolecules* 27: 2414-2425.
175. Batrakova EV, Li S, Alakhov VY et al. 2003. Optimal Structure Requirements for Pluronic Block Copolymers in Modifying P-glycoprotein Drug Efflux Transporter Activity in Bovine Brain Microvessel Endothelial Cells. *Journal of Pharmacology and Experimental Therapeutics* 304: 845-854.
176. Wu G, Majewski J, Ege C et al. 2005. Interaction between lipid monolayers and poloxamer 188: an X-ray reflectivity and diffraction study. *Biophys J* 89: 3159-3173.
177. Honda H, Kondo T, Zhao QL et al. 2004. Role of intracellular calcium ions and reactive oxygen species in apoptosis induced by ultrasound. *Ultrasound Med Biol* 30: 683-692.
178. Juffermans LJ, Dijkmans PA, Musters RJ et al. 2006. Transient permeabilization of cell membranes by ultrasound-exposed microbubbles is related to formation of hydrogen peroxide. *Am J Physiol Heart Circ Physiol* 291: H1595-1601.
179. Kumon RE, Aehle M, Sabens D et al. 2007. Ultrasound-induced calcium oscillations and waves in Chinese hamster ovary cells in the presence of microbubbles. *Biophys J* 93: L29-31.
180. McNeil PL, Kirchhausen T. 2005. An emergency response team for membrane repair. *Nat Rev Mol Cell Biol* 6: 499-505.
181. Tang Q, Jin MW, Xiang JZ et al. 2007. The membrane permeable calcium chelator BAPTA-AM directly blocks human ether a-go-go-related gene potassium channels stably expressed in HEK 293 cells. *Biochem Pharmacol* 74: 1596-1607.
182. Gndz D, Kasseckert SA, Hrtel FV et al. 2006. Accumulation of extracellular ATP protects against acute reperfusion injury in rat heart endothelial cells. *Cardiovascular*

Research 71: 764-773.

183. Podesta JE, Kostarelos K. 2009. Chapter 17 - Engineering cationic liposome siRNA complexes for in vitro and in vivo delivery. *Methods Enzymol* 464: 343-354.
184. Ko R, Smith LT, Smith GM. 1994. Glycine betaine confers enhanced osmotolerance and cryotolerance on *Listeria monocytogenes*. *Journal of Bacteriology* 176: 426-431.
185. Conska LN, Epstein W. 1996. Osmoregulation. In: others FCNa, editor. *Escherichia coli and Salmonella typhimurium: Cellular and Molecular Biology*. Washington, DC: ASM Press p 1210-1223.
186. Caldas T, Demont-Caulet N, Ghazi A, Richarme G. 1999. Thermoprotection by glycine betaine and choline. *Microbiology* 145: 2543-2548.
187. Dumortier G, Grossiord JL, Agnely F, Chaumeil JC. 2006. A review of poloxamer 407 pharmaceutical and pharmacological characteristics. *Pharm Res* 23: 2709-2728.
188. Firestone MA, Seifert S. 2005. Interaction of Nonionic PEO-PPO Diblock Copolymers with Lipid Bilayers. *Biomacromolecules* 6: 2678-2687.
189. Al-Rubeai M, Emery AN, Chalder S, Goldman MH. 1993. A flow cytometric study of hydrodynamic damage to mammalian cells. *Journal of Biotechnology* 31: 161-177.
190. Gigout A, Buschmann MD, Jolicoeur M. 2008. The fate of Pluronic F-68 in chondrocytes and CHO cells. *Biotechnology and Bioengineering* 100: 975-987.
191. Weaver JC, Chizmadzhev YA. 1996. Theory of electroporation: A review. *Bioelectrochemistry and Bioenergetics* 41: 135-160.
192. Diamant S, Eliahu N, Rosenthal D, Goloubinoff P. 2001. Chemical chaperones regulate molecular chaperones in vitro and in cells under combined salt and heat stresses. *J Biol Chem* 276: 39586-39591.
193. Sharom FJ. 1997. The P-glycoprotein efflux pump: how does it transport drugs? *J Membr Biol* 160: 161-175.

194. Lodish H, Berk A, Kaiser CA et al. *Molecular Cell Biology*. New York: W. H. Freeman and Co. 2000.
195. Lodish H, Berk A, L. ZS et al. *Receptor-Mediated Endocytosis and the Sorting of Internalized Proteins*. *Molecular Cell Biology*. 4 ed. New York: W. H. Freeman 2000.
196. Wells AJ, Smith WR. 1941. The Absorption Spectrum of Suspensions of Carbon Black. *The Journal of Physical Chemistry* 45: 1055-1060.
197. Mourant JR, Fuselier T, Boyer J et al. 1997. Predictions and measurements of scattering and absorption over broad wavelength ranges in tissue phantoms. *Appl Opt* 36: 949-957.
198. Bond TC, Bergstrom RW. 2006. Light Absorption by Carbonaceous Particles: An Investigative Review. *Aerosol Science and Technology* 40: 27-67.
199. Grigonis A, Rutkuniene Z, Vinciunaite V. 2011. Different Wavelength Laser Irradiation of Amorphous Carbon. *ACTA PHYSICA POLONICA A* 120: 26-29.
200. Hunt BE, Mori S, Katz S, Peck RE. 1953. Reaction of Carbon with Steam at Elevated Temperatures. *Industrial & Engineering Chemistry* 45: 677-680.
201. Park HK, Kim D, Grigoropoulos CP, Tam AC. 1996. Pressure generation and measurement in the rapid vaporization of water on a pulsed-laser-heated surface. *J Appl Phys* 80: 4072-4081.
202. Markham JJ, Beyer RT, Lindsay R. 1951. Absorption of Sound in Fluids. *Rev Mod Phys* 23: 353-411.
203. Pierce AD. 1991. *Acoustics an introduction to its physical principles and applications*. Woodbury, NY: Acoustical Soc. of America
204. Lyamshev LM, Naugol'nykh KA. 1981. Optical generation of sound: nonlinear effects (review). *Sov Phys Acoust* 27: 357-371.

205. Teslenko VS. 1977. Investigation of photoacoustic and photohydrodynamic parameters of laser breakdown in liquids. *Soviet Journal of Quantum Electronics* 7: 981.
206. Elbashir SM, Harborth J, Lendeckel W et al. 2001. Duplexes of 21-nucleotide RNAs mediate RNA interference in cultured mammalian cells. *Nature* 411: 494-498.
207. Whitehead KA, Langer R, Anderson DG. 2009. Knocking down barriers: advances in siRNA delivery. *Nat Rev Drug Discov* 8: 129-138.
208. Frank-Kamenetsky M, Grefhorst A, Anderson NN et al. 2008. Therapeutic RNAi targeting PCSK9 acutely lowers plasma cholesterol in rodents and LDL cholesterol in nonhuman primates. *Proceedings of the National Academy of Sciences*.
209. Sato Y, Murase K, Kato J et al. 2008. Resolution of liver cirrhosis using vitamin A-coupled liposomes to deliver siRNA against a collagen-specific chaperone. *Nat Biotechnol* 26: 431-442.
210. Song E, Lee SK, Wang J et al. 2003. RNA interference targeting Fas protects mice from fulminant hepatitis. *Nat Med* 9: 347-351.
211. Morrissey DV, Lockridge JA, Shaw L et al. 2005. Potent and persistent in vivo anti-HBV activity of chemically modified siRNAs. *Nat Biotechnol* 23: 1002-1007.
212. Niu XY, Peng ZL, Duan WQ et al. 2006. Inhibition of HPV 16 E6 oncogene expression by RNA interference in vitro and in vivo. *Int J Gynecol Cancer* 16: 743-751.
213. Takeshita F, Minakuchi Y, Nagahara S et al. 2005. Efficient delivery of small interfering RNA to bone-metastatic tumors by using atelocollagen in vivo. *Proc Natl Acad Sci U S A* 102: 12177-12182.
214. Tabernero J, Shapiro GI, LoRusso PM et al. 2013. First-in-Humans Trial of an RNA Interference Therapeutic Targeting VEGF and KSP in Cancer Patients with Liver Involvement. *Cancer Discovery* 3: 406-417.

215. Davis ME. 2009. The First Targeted Delivery of siRNA in Humans via a Self-Assembling, Cyclodextrin Polymer-Based Nanoparticle: From Concept to Clinic. *Molecular Pharmaceutics* 6: 659-668.
216. Tomar RS, Matta H, Chaudhary PM. 2003. Use of adeno-associated viral vector for delivery of small interfering RNA. *Oncogene* 22: 5712-5715.
217. Devroe E, Silver PA. 2002. Retrovirus-delivered siRNA. *BMC Biotechnol* 2: 15.
218. Hughes J, Yadava P, Mesaros R. 2010. Liposomal siRNA delivery. *Methods Mol Biol* 605: 445-459.
219. Rosi NL, Giljohann DA, Thaxton CS et al. 2006. Oligonucleotide-modified gold nanoparticles for intracellular gene regulation. *Science* 312: 1027-1030.
220. Giljohann DA, Seferos DS, Prigodich AE et al. 2009. Gene regulation with polyvalent siRNA-nanoparticle conjugates. *J Am Chem Soc* 131: 2072-2073.
221. Davis ME, Zuckerman JE, Choi CH et al. 2010. Evidence of RNAi in humans from systemically administered siRNA via targeted nanoparticles. *Nature* 464: 1067-1070.
222. Lewis DL, Wolff JA. 2007. Systemic siRNA delivery via hydrodynamic intravascular injection. *Adv Drug Deliv Rev* 59: 115-123.
223. Thomas CE, Ehrhardt A, Kay MA. 2003. Progress and problems with the use of viral vectors for gene therapy. *Nat Rev Genet* 4: 346-358.
224. Howard DB, Powers K, Wang Y, Harvey BK. 2008. Tropism and toxicity of adeno-associated viral vector serotypes 1, 2, 5, 6, 7, 8, and 9 in rat neurons and glia in vitro. *Virology* 372: 24-34.
225. de Bruin KG, Fella C, Ogris M et al. 2008. Dynamics of photoinduced endosomal release of polyplexes. *J Control Release* 130: 175-182.
226. Mintzer MA, Simanek EE. 2009. Nonviral vectors for gene delivery. *Chem Rev* 109: 259-302.

227. Oishi M, Kataoka K, Nagasaki Y. 2006. pH-responsive three-layered PEGylated polyplex micelle based on a lactosylated ABC triblock copolymer as a targetable and endosome-disruptive nonviral gene vector. *Bioconjug Chem* 17: 677-688.
228. Kitz M, Preisser S, Wetterwald A et al. 2011. Vapor bubble generation around gold nano-particles and its application to damaging of cells. *Biomed Opt Express* 2: 291-304.
229. Chakravarty P, Qian W, El-Sayed MA, Prausnitz MR. 2010. Delivery of molecules into cells using carbon nanoparticles activated by femtosecond laser pulses. *Nat Nanotechnol* 5: 607-611.
230. Huang X, Pallaoro A, Braun GB et al. 2014. Modular Plasmonic Nanocarriers for Efficient and Targeted Delivery of Cancer-Therapeutic siRNA. *Nano Letters* 14: 2046-2051.
231. Siegel R, Naishadham D, Jemal A. 2012. Cancer statistics, 2012. *CA Cancer J Clin* 62: 10-29.
232. <http://seer.cancer.gov/statfacts/html/ovary.html>. [Accessed on: 8th May 2014].
233. Ozols RF. 2005. Treatment goals in ovarian cancer. *Int J Gynecol Cancer* 15 Suppl 1: 3-11.
234. Dickerson EB, Blackburn WH, Smith MH et al. 2010. Chemosensitization of cancer cells by siRNA using targeted nanogel delivery. *BMC Cancer* 10: 10.
235. Weissleder R. 2001. A clearer vision for in vivo imaging. *Nat Biotechnol* 19: 316-317.
236. Stolik S, Delgado JA, Prez A, Anasagasti L. 2000. Measurement of the penetration depths of red and near infrared light in human ex vivo tissues. *Journal of Photochemistry and Photobiology B: Biology* 57: 90-93.
237. Han D, Meng Z, Wu D et al. 2011. Thermal properties of carbon black aqueous nanofluids for solar absorption. *Nanoscale Res Lett* 6: 457.

238. Fang J, Nakamura H, Maeda H. 2011. The EPR effect: Unique features of tumor blood vessels for drug delivery, factors involved, and limitations and augmentation of the effect. *Adv Drug Deliv Rev* 63: 136-151.
239. Roduner E. 2006. Size matters: why nanomaterials are different. *Chemical Society Reviews* 35: 583-592.
240. Schlicher RK, Radhakrishna H, Tolentino TP et al. 2006. Mechanism of intracellular delivery by acoustic cavitation. *Ultrasound Med Biol* 32: 915-924.
241. Prausnitz MR, Corbett JD, Gimm JA et al. 1995. Millisecond measurement of transport during and after an electroporation pulse. *Biophys J* 68: 1864-1870.
242. Goldman L, Blaney DJ, Kindel Jr DJ, Franke EK. 1963. Effect of the Laser Beam on the Skin¹. *The Journal of Investigative Dermatology* 40: 121-122.
243. Kuperman-Beadle M, Levine VJ, Ashinoff R. 2001. Laser removal of tattoos. *Am J Clin Dermatol* 2: 21-25.
244. Nanni C. 1997. Complications of laser surgery. *Dermatol Clin* 15: 521-534.
245. Taneri S, Zieske JD, Azar DT. 2004. Evolution, techniques, clinical outcomes, and pathophysiology of LASEK: review of the literature. *Surv Ophthalmol* 49: 576-602.
246. Eugene J, McColgan SJ, Hammer-Wilson M, Berns MW. 1985. Laser endarterectomy. *Lasers Surg Med* 5: 265-274.
247. Kelly JD, Keane PF, Johnston SR, Kernohan RM. 1995. Laser lithotripsy for ureteric calculi: results in 250 patients. *Ulster Med J* 64: 126-130.
248. Karni RJ, Rich JT, Sinha P, Haughey BH. 2011. Transoral laser microsurgery: A new approach for unknown primaries of the head and neck. *The Laryngoscope* 121: 1194-1201.
249. Joris I, Cuenoud HF, Doern GV et al. 1990. Capillary leakage in inflammation. A study by vascular labeling. *Am J Pathol* 137: 1353-1363.

250. Majno G, Palade GE, Schoeffl GI. 1961. Studies on inflammation. II. The site of action of histamine and serotonin along the vascular tree: a topographic study. *J Biophys Biochem Cytol* 11: 607-626.
251. Linden R, Cavalcante LA, Barradas PC. 1986. Mononuclear phagocytes in the retina of developing rats. *Histochemistry* 85: 335-339.
252. Xia T, Kovochich M, Brant J et al. 2006. Comparison of the Abilities of Ambient and Manufactured Nanoparticles To Induce Cellular Toxicity According to an Oxidative Stress Paradigm. *Nano Letters* 6: 1794-1807.
253. Zabetakis K, Ghann W, Kumar S, Daniel M-C. 2012. Effect of high gold salt concentrations on the size and polydispersity of gold nanoparticles prepared by an extended Turkevich-Frens method. *Gold Bull* 45: 203-211.
254. Arosio D, Manzoni L, Araldi EM, Scolastico C. 2011. Cyclic RGD functionalized gold nanoparticles for tumor targeting. *Bioconjug Chem* 22: 664-672.
255. Albanese A, Lam AK, Sykes EA et al. 2013. Tumour-on-a-chip provides an optical window into nanoparticle tissue transport. *Nat Commun* 4.
256. Shi C, Soltani S, Armani AM. 2013. Gold Nanorod Plasmonic Upconversion Micro-laser. *Nano Letters* 13: 5827-5831.
257. Stern JM, Stanfield J, Lotan Y et al. 2007. Efficacy of laser-activated gold nanoshells in ablating prostate cancer cells in vitro. *J Endourol* 21: 939-943.
258. Hu M, Petrova H, Chen J et al. 2006. Ultrafast laser studies of the photothermal properties of gold nanocages. *J Phys Chem B* 110: 1520-1524.
259. Zarnitsyn V, Rostad CA, Prausnitz MR. 2008. Modeling transmembrane transport through cell membrane wounds created by acoustic cavitation. *Biophys J* 95: 4124-4138.

260. Faraggi E, Gerstman BS, Sun J. 2005. Biophysical effects of pulsed lasers in the retina and other tissues containing strongly absorbing particles: shockwave and explosive bubble generation. *J Biomed Opt* 10: 064029.